

5-4-2018

Data-Driven Process Optimization of Additive Manufacturing Systems

Amirmassoud Aboutaleb

Follow this and additional works at: <https://scholarsjunction.msstate.edu/td>

Recommended Citation

Aboutaleb, Amirmassoud, "Data-Driven Process Optimization of Additive Manufacturing Systems" (2018).
Theses and Dissertations. 1254.
<https://scholarsjunction.msstate.edu/td/1254>

This Dissertation - Open Access is brought to you for free and open access by the Theses and Dissertations at Scholars Junction. It has been accepted for inclusion in Theses and Dissertations by an authorized administrator of Scholars Junction. For more information, please contact scholcomm@msstate.libanswers.com.

Data-driven process optimization of Additive Manufacturing systems

By

Amirmassoud Aboutaleb

A Dissertation
Submitted to the Faculty of
Mississippi State University
in Partial Fulfillment of the Requirements
for the Degree of Doctor of Philosophy
in Industrial and Systems Engineering
in the Department of Industrial and Systems Engineering

Mississippi State, Mississippi

May 2018

Copyright by
Amirmassoud Aboutaleb
2018

Data-driven process optimization of Additive Manufacturing systems

By

Amirmassoud Aboutaleb

Approved:

Linkan Bian
(Major Professor)

Tung-Lung Wu
(Minor Professor)

John Usher
(Committee Member)

Mohammad Marufuzzaman
(Committee Member)

Reuben Burch
(Committee Member)

Stanley F. Bullington
(Graduate Coordinator)

Jason Keith
Dean
Bagley College of Engineering

Name: Amirmassoud Aboutaleb

Date of Degree: May 4, 2018

Institution: Mississippi State University

Major Field: Industrial and Systems Engineering

Major Professor: Linkan Bian

Title of Study: Data-driven process optimization of Additive Manufacturing systems

Pages in Study 211

Candidate for Degree of Doctor of Philosophy

The goal of the present dissertation is to develop and apply novel and systematic data-driven optimization approaches that can efficiently optimize Additive Manufacturing (AM) systems with respect to targeted properties of final parts. The proposed approaches are capable of achieving sets of process parameters that result in the satisfactory level of part quality in an accelerated manner. First, an Accelerated Process Optimization (APO) methodology is developed to optimize an individual scalar property of parts. The APO leverages data from similar—but non-identical—prior studies to accelerate sequential experimentation for optimizing the AM system in the current study. Using Bayesian updating, the APO characterizes and updates the difference between prior and current experimental studies. The APO accounts for the differences in experimental conditions and utilizes prior data to facilitate the optimization procedure in the current study. The efficiency and robustness of the APO is tested against an extensive simulation studies and a real-world case study for optimizing relative density of stainless steel parts fabricated by a Selective Laser Melting (SLM) system. Then, we extend the idea behind the APO to handle multi-objective process optimization problems in which some of the characteristics of the AM-fabricated parts are uncorrelated. The proposed Multi-objective Process

Optimization (m-APO) breaks down the master multi-objective optimization problem into a series of convex combinations of single-objective sub-problems. The m-APO maps and scales experimental data from previous sub-problems to guide remaining sub-problems that improve the solutions while reducing the number of experiments required. The robustness and efficiency of the m-APO is verified by conducting a series of simulation studies and a real-world case study to minimize geometric inaccuracy of parts fabricated by a Fused Filament Fabrication (FFF) system. At the end, we apply the proposed m-APO to optimize the mechanical properties of AM-fabricated parts that show conflicting behavior, namely relative density and elongation-to-failure. Numerical studies show that the m-APO can achieve the best trade-off among conflicting mechanical properties while significantly reducing the number of experimental runs compared with existing methods.

Keywords: additive manufacturing, process optimization, design of experiments, Bayesian updating, multi-objective optimization, geometric accuracy, principal component analysis, tensile properties.

DEDICATION

It is honorably dedicated to:

Those who spread peace, love, brotherhood and unity;

Those who endeavor to make the planet a better, happier and safer place to live;

Those who are committed to pure moral principles, man's dignity and ethics;

My life master and hero, my father in heaven, who has been always a constant source of courage, inspiration and passion;

The angle of my life, my lovely mom, who taught me how to unconditionally and generously love and be stronger;

And, my adorable and supporting fiancée, Dr. Parvaneh Jahani, who is constantly loving me and proving to me that life is a majestic God's grace and every single second of that should be a unique glorious experience and a magnificent adventure.

ACKNOWLEDGEMENTS

With my deepest gratitude, I would like to thank my advisor, Dr. Linkan Bian, who always reminds me that “great things never come from comfort zones”. I’m thankful that he provided me all the challenges and opportunities I needed to be eligible for being a doctor. I would also warmly thank Dr. John Usher for his supports and warm-heartedness. At the end, I would like to express my profound appreciation to my other committee members Dr. Mohammad Marufuzzaman, Dr. Tung-Lung Wu and Dr. Reuben Burch.

TABLE OF CONTENTS

DEDICATION	ii
ACKNOWLEDGEMENTS	iii
LIST OF TABLES	viii
LIST OF FIGURES	xi
CHAPTER	
I. INTRODUCTION	14
1.1 Research challenges.....	14
1.1.1 Challenges with LBAM process optimization	15
1.1.2 Challenges with optimizing geometric accuracy of AM-fabricated parts	16
1.1.3 Challenges with optimizing multiple mechanical properties of LBAM-fabricated parts	17
1.2 Proposed solutions.....	18
1.2.1 Accelerated Process Optimization (APO) of LBAM-fabricated parts by leveraging data from similar—but non-identical—studies	18
1.2.2 Multi-objective Accelerated Process Optimization (m-APO) for optimizing geometric accuracy of AM-fabricated parts	19
1.2.3 Multi-objective Accelerated Process Optimization (m-APO) for optimizing multiple mechanical properties of LBAM-fabricated parts	20
1.3 Dissertation organization.....	21
II. A REVIEW ON LASER-BASED ADDITIVE MANUFACTURING PROCESS OPTIMIZATION.....	23
2.1 Introduction: effects of parameters.....	23
2.1.1 Laser power and laser velocity	25
2.1.2 Layer height.....	25
2.1.3 Deposition pattern	26
2.2 Physics-based Models	28
2.2.1 Buckingham's II theorem.....	29
2.2.2 Process characterization	33

2.2.3	Steady state thermal maps	33
2.2.4	Thermal maps for transient analysis	34
2.2.5	Process maps for different scales of LBAM systems	34
2.2.6	Limitation of process maps	35
2.3	Data-driven optimization methods	36
2.3.1	Full factorial designs	37
2.3.2	Fractional factorial design	39
2.3.3	Taguchi design.....	44
2.3.4	More advanced designs and modeling methods	49
2.3.4.1	Space filling designs	49
2.3.4.2	D-Optimal designs	50
2.3.4.3	Response surface and Kriging	51
2.3.4.4	Artificial intelligence.....	56
2.4	Summary.....	57
III.	ACCELERATED PROCESS OPTIMIZATION FOR LASER-BASED ADDITIVE MANUFACTURING BY LEVERAGING SIMILAR PRIOR STUDIES.....	59
2.5	Introduction	59
2.6	Methodology: accelerated process optimization by leveraging related but non-identical prior studies	63
2.6.1	Sequential Minimum Energy Design (SMED).....	64
2.6.2	Accelerated Process Optimization (APO) based on SMED	66
2.6.2.1	Characterizing DRPCS	68
2.6.2.2	Predicting the response at new design points	70
2.6.2.3	Updating DRPCS.....	73
2.7	Numerical studies	79
2.7.1	Simulation studies	79
2.7.1.2	Comparing our approach with full factorial DOE	83
2.7.1.3	Comparing our approach with sequential minimum energy design (SMED)	84
2.7.1.4	Comparing various charge functions.....	86
2.7.2	Case study.....	87
2.8	Summary and conclusions.....	91
IV.	MULTI-OBJECTIVE ACCELERATED PROCESS OPTIMIZATION OF PART GEOMETRIC ACCURACY IN ADDITIVE MANUFACTURING.....	94
2.9	Introduction	94
2.9.1	Objective and hypothesis.....	94
2.9.2	Motivation	95
2.9.3	Research challenges and overview of the proposed approach	97
2.10	Literature review	100

2.10.1	Existing literature in geometric accuracy optimization in AM processes	100
2.10.2	Background in multi-objective optimization	102
2.11	Methodology	103
2.11.1	Description of the experimentally obtained geometric accuracy data	103
2.11.2	Multi-objective process optimization	107
2.11.2.1	Scalarization of multi-objective optimization and Pareto front	107
2.11.2.2	Multi-objective Accelerated Process Optimization (m-APO)	111
2.12	Experimental and numerical studies	117
2.12.1	Experimental case study: multi-geometric characteristic optimization of parts fabricated by FFF system	118
2.12.2	Numerical simulation studies for non-convex Pareto front	123
2.12.2.1	Case A: non-convex Pareto front and well-distributed objective space	124
2.12.2.2	Case B: non-convex Pareto front and congested objective space	125
2.12.2.3	Case C: high dimension design space	126
2.12.2.4	Simulation results: Pareto front estimation	127
2.13	Conclusions	130
V.	MULTI-OBJECTIVE ACCELERATED PROCESS OPTIMIZATION OF MECHANICAL PROPERTIES IN LASER-BASED ADDITIVE MANUFACTURING: CASE STUDY ON SELECTIVE LASER MELTING (SLM) Ti-6Al-4V	132
2.14	Introduction	132
2.14.1	Objective and hypothesis	132
2.14.2	Motivation	133
2.14.3	Research challenges and overview of the proposed approach	137
2.15	Background: mechanical properties of laser-based additive manufacturing	142
2.16	Methodology	145
2.16.1	Multi-objective process optimization	145
2.16.1.1	Multi-objective process optimization and Pareto front	146
2.16.1.2	An overview of Multi-objective Accelerated Process Optimization (m-APO)	150
2.17	Experimental case study and discussion: mechanical properties optimization of Ti-6Al-4V parts fabricated by Selective Laser Melting (SLM)	152
2.17.1	Experimental data generation: fabrication and test procedures	153
2.17.2	Initial design of experiments setups and data generation	154
2.17.3	Apply Multi-objective Accelerated Process Optimization (m-APO)	155

2.18	Conclusions	158
VI.	CONCLUSIONS	160
	REFERENCES	164
APPENDIX		
A.	PRIOR DISTRIBUTION OF λ_i 's	177
B.	PROPORTIONAL FORMULA OF $f(\mathbf{Y} \boldsymbol{\lambda}, \mathbf{u})$	179
C.	POSTERIOR DISTRIBUTION OF λ_i 's	182
D.	CALCULATION OF $\boldsymbol{\Lambda}$ AND $\boldsymbol{\eta}$	184
E.	EXPERIMENTAL RESULTS FOR APO SIMULATIONS	187
F.	EFFECT OF $\boldsymbol{\gamma}$ ON THE OPTIMIZATION PERFORMANCE	193
G.	ALGORITHM OF M-APO	205

LIST OF TABLES

2.1	Parameters for metal deposition.	31
2.2	Dimensionless parameters.	32
2.3	Levels of Process Parameters.	41
2.4	Design matrix of factorial design.	42
2.5	Main effects of parameters.	42
2.6	L ₄ design.	45
2.7	L ₈ design.	46
2.8	L _{16B} orthogonal array.	48
2.9	ANOVA for shrinkage in X-direction.	49
3.1	DOE factors and levels applied for empirical density empirical function, Eq. 3.5.	80
3.2	Different types of DRPCS for SLM SS 17-4 PH.	82
3.3	Process optimization using full factorial DOE.	83
3.4	Computational time needed to obtain optimal process parameters.	86
3.5	Number of experiment runs needed to achieve the target density with various choices of change functions and various scenarios of DRPCS.	87
3.6	Experimental conditions in prior and current studies for SLM of 17-4 PH SS.	89
3.7	Experimental data from prior studies [49,59,72].	90
3.8	Density optimization data of the case study.	91
4.1	Levels of the process parameters applied to generate experimental data based on full factorial DOE plan.	119

4.2	Signed correlation among GD&T characteristics of benchmark part samples.	120
4.3	The 88.15% of variability within the parts' geometry characteristics data is captured by the first two principal components.	121
4.4	Illustrating principal components' coefficients.....	121
4.5	Optimal process parameters and corresponding GD&T values achieved in the case study	122
4.6	Improvement achieved in simulation studies by m-APO in terms of decreasing General Distance (GD) and increasing Proportional Hyper-Volume (PHV) for three test problems.	130
5.1	Chemical composition of powder used to fabricate the Ti-6Al-4V specimens.	153
5.2	Levels of the process parameters applied in the initial full factorial DOE plan.	155
5.3	Levels of the process parameters applied in the auxiliary full factorial DOE plan to narrow down to the effect of laser power.....	155
5.4	Optimal process parameters and the corresponding, relative density, elongation-to-failure and ultimate stress.	157
E.1	Prior data with negative DRPCS.	188
E.2	Prior data with smaller DRPCS (compared to Table E.1).....	189
E.3	Prior data with positive and negative DRPCS.....	190
E.4	Prior data with positive DRPCS.....	191
E.5	More prior data points.	192
F.1	Performance of SMED and our method with negative DRPCS and $\gamma=1$	194
F.2	Performance of SMED and our method with positive and negative DRPCS and $\gamma=1$	195
F.3	Performance of SMED and our method with positive DRPCS and $\gamma=1$	196
F.4	Performance of SMED and our method with positive DRPCS and $\gamma=3$ (Same as Table E.1).....	197

F.5	Performance of SMED and our method with positive and negative DRPCS and $\gamma=3$ (Same as Table E.3).	198
F.6	Performance of SMED and our method with positive DRPCS and $\gamma=3$ (Same as Table E.4).....	199
F.7	Performance of SMED and our method with negative DRPCS and $\gamma=5$	200
F.8	Performance of SMED and our method with negative DRPCS and $\gamma=5$	202
F.9	Performance of SMED and our method with positive DRPCS and $\gamma=5$	203
F.10	Performance of SMED and our method with positive DRPCS and $\gamma=5$	204

LIST OF FIGURES

2.1	Different deposition patterns.	27
2.2	2^3 designs.....	37
2.3	2^2 designs.....	39
2.4	Fractional factorial designs.....	40
2.5	Response surface of $g(x) = 20 + 5x_1 + 3x_2$	52
2.6	Contour plot of $g(x) = 20 + 5x_1 + 3x_2$	53
2.7	Response surface of $gx = 20 + 5x_1 + 3x_2 - x_1x_2$	54
2.8	Contour plot of $gx = 20 + 5x_1 + 3x_2 - x_1x_2$	54
3.1	Difference between prior and current studies.....	62
3.2	Applying SMED to LBAM process optimization.	66
3.3	Framework of the proposed accelerated process optimization (APO) method.	68
3.4	Empirical relation between relative part density and energy density [59].	80
3.5	Comparison between SMED and our method's performance.	84
3.6	Resulted improvement by applying our method instead of SMED.....	84
3.7	ProX 100 SLM System (left) and test coupons (right).	88
4.1	Flooded contour plots (deviation maps) of the benchmark part used in FFF experiments detailed in Sec. 4.3.1.	96
4.2	Contour plot of (a) part concentricity and (b) flatness vs. infill percentage (If) and extruder temperature(te).	97
4.3	Design of the circle-square-diamond part.	104

4.4	The areas used to measure GD&T form the design part.	105
4.5	The eight points used for alignment of the scan points with the CAD model.	106
4.6	The representation of the data scatter plot matrix to illustrate both positive and negative correlations among pairs of part geometric characteristics.	107
4.7	Schematic illustration of design space, objective space, non-dominated design points, Pareto points and Pareto front.	110
4.8	Leveraging the information from prior data to accelerate solving subsequent sub- problems.....	113
4.9	Multi-objective Accelerated Process Optimization (m-APO) flowchart.....	114
4.10	Schematic illustration of HV (Hyper-Volume) as the measure of the contribution of Pareto points.	116
4.11	A schematic diagram of the FFF process [76,77].....	119
4.12	Demonstrating the Pareto points and conducted experiments for the case study.....	122
4.13	Case A—Discretization of objective space for test problem with non-convex Pareto front and well-distributed objective space.	125
4.14	Case B—Discretization of objective space for test problem with non-convex Pareto front and congested objective space.	126
4.15	Case C—Discretization of objective space for test problem with increased number of process parameters.	127
4.16	Case A—Comparing estimated Pareto front resulted by m-APO and full factorial DOE with true Pareto front (test problem with non-convex Pareto front and well-distributed objective space).....	128
4.17	Case B—Comparing estimated Pareto front resulted by m-APO and full factorial DOE with true Pareto front (test problem with non-convex Pareto front and congested objective space).	128
4.18	Case C—Comparing estimated Pareto front resulted by m-APO and full factorial DOE with true Pareto front (test problem with increased number of process parameters).....	129

5.1	Schematic indicating the various possible distribution of voids for samples with similar densities, which may result in different tensile properties.	136
5.2	Contour plot of (a) part density and (b) part elongation-to-failure (ϵ_f) versus hatch spacing and layer thickness.	137
5.3	Selected stress-strain curves of the different specimens fabricated with different process parameters, indicating the sensitivity of the tensile properties to the process parameters.	138
5.4	The representation of the data scatter plot to illustrate correlation between scaled part relative density and scaled elongation-to-failure.	140
5.5	Schematic illustration of design space, objective space, optimal design point, Pareto optimal solution and Pareto front [135,136].....	148
5.6	Different combinations of weight coefficients lead to distinct shapes of contour plot for the weighted summation of part relative density and elongation-to-failure.	149
5.7	The m-APO leverages experimental data obtained from prior sub-problems to accelerate solving the subsequent sub-problems.	152
5.8	Schematic showing the dimensions of the specimen used in monotonic tensile tests (all dimensions are in mm).	154
5.9	Demonstrating the objective space, Pareto optimal solutions and conducted experiments by m-APO.....	156
G.1	Schematic illustration of applying APO to different sub-problems, and representing the design space dynamics associated with conducting m-APO.	209
G.2	Schematic illustration of HV as the yardstick of improving the Pareto front approximation.	210

CHAPTER I

INTRODUCTION

Additive Manufacturing (AM) has been featured as a disruptive innovation and a new industrial revolution among research-industrial communities as well as public media. AM is capable of fabricating parts directly from a computer-aided design (CAD) model in a layer-by-layer manner. Hence, AM—as a set of emerging technologies—provides a unique opportunity to fabricate functional parts with very complex geometries, customized design and functionally graded materials [1]. It also brings a great opportunity to significantly shorten the logistical supply chain in many industries, namely deafens and biomedical implants [2,3]. Moreover, AM can reduce material waste and improve part consolidation because of its capability to fabricate final parts without any part-specific tooling [4]. Nowadays, the most recent AM systems, Laser-Based Additive Manufacturing (LBAM), are capable of fabricating metallic parts with the potential of being utilized as end-parts for direct use in a variety of industries and applications [1,4,5]. Manufacturing parts with target properties and quality in AM is crucial toward enhancing the “trustworthiness” of this emerging technology and pushing it into the mainstream.

1.1 Research challenges

Despite the unique industrial paradigm-shifting potentials of AM, its poor process reliability as well as non-satisfactory quality of AM-fabricated parts remains the Achilles Heel for AM and hinder its commercial viability and widespread application. Depending

on the material and type of AM, the quality issues for AM-fabricated parts include, but are not limited to, high surface roughness, low relative density, poor mechanical properties (such as tensile strength, fatigue life and elongation-to-failure) and geometric inaccuracy. In the present dissertation, we develop novel methodologies and systematic frameworks to identify sets of optimal process parameters, which result in satisfactory level of quality with respect to quantifiable properties of AM-fabricated parts, such as relative density, tensile properties and geometric characteristics.

1.1.1 Challenges with LBAM process optimization

In Chapter 2, we conduct a comprehensive literature review concerning the effect of process parameters involved in LBAM systems. We also review the existing and common methodologies in the realm of LBAM pertaining to characterization and optimization of the melt-pool formation, solidification and quality of final parts. These approaches are grouped into two major categories: (i) physics-based models and (ii) data-driven optimization methods. We find that a large number of process parameters contribute to the fabrication process and eventually affect the quality of final parts, namely laser power, laser velocity, powder feed rate, layer thickness, hatching space, scanning pattern, etc. Hence, identifying the optimal process parameter setup—with respect to just a single quantifiable characteristic of parts such as relative density—is extremely challenging because of high dimensional parameter space. This challenge is further compounded considering the interactions among process parameters. In other words, the effect of one process parameter depends on the effect of the other process parameters. Moreover, due to the very complex underlying thermo-mechanical process, the mathematical formula representing the relationship between process parameters and the properties of the final

parts is unknown. In other words, the functional form of objective function is not easily achievable.

Most of existing researches seek the optimal process parameter setups via extensive experimental runs. However, in reality, it may not be possible to consider all process parameters and the corresponding interactions in either experimental or analytical studies. Moreover, considering the LBAM very time-and cost-intensive experiments it may not be practical to utilize conventional design of experiments (DoE) methodologies (e.g., fractional and full factorial designs). Another major limitation of the existing approaches is that the resulting optimal process parameters cannot be applied to a similar process because of the differences in the experimental conditions (e.g., powder morphology or machine brand). With this in mind, there is an urgent need to develop a generic optimization framework that can (i) systematically characterize the relationship between process parameters and the desired characteristics of the final parts and (ii) efficiently leverage the information from existing prior studies to accelerate the process optimization in the current study.

1.1.2 Challenges with optimizing geometric accuracy of AM-fabricated parts

Due to the layer-by-layer nature of the AM fabrication process, geometric accuracy of final parts is not usually as it is desired. Initial experimental data show that there are some deviations of 3D point cloud coordinate measurements from design specifications [6,7]. In other words, the shape of the final parts deviates from the original computer-aided design (CAD) file. To address this issue, some data-driven approaches targeted at compensating for AM-fabricated part geometry distortions have been recently proposed

[8–10]. However, these research approaches are restricted to elementary shapes (such as cubes and cylinders), and are limited to modeling of uniaxial geometry deviations.

The geometric accuracy optimization of AM-fabricated parts is an extremely challenging research problem since experimental data represent conflicting behavior among geometric characteristics (e.g., flatness and concentricity) of AM-fabricated parts. That is, improving the accuracy of one geometric characteristic of parts, such as flatness, will result in worsening another geometric characteristic of them, such as concentricity. Hence, the observed negative correlation among the geometric characteristics of AM-fabricated parts (e.g., flatness and concentricity) makes the abovementioned research problem even more complicated. Considering this, the problem of geometric accuracy optimization for AM-fabricated parts falls into the area of multi-objective optimization. The existing multi-objective optimization methodologies are not applicable in our case since the functional form of objective functions is not explicitly known. Additionally, constructing the meta-models representing the objective functions is not economically feasible because of high experimental cost in AM. Hence, there is an urgent need for an efficient experimental framework that can achieve the best compromises between conflicting geometric characteristics of AM-fabricated parts.

1.1.3 Challenges with optimizing multiple mechanical properties of LBAM-fabricated parts

It is traditionally believed that optimizing the relative density for LBAM-fabricated parts results in satisfactory level of other mechanical properties of parts. However, our further experimental studies reveal that maximizing the relative density of the part—although necessary—might not be sufficient to achieve a reliable level of other mechanical

properties, such as elongation-to-failure. Optimizing multiple mechanical properties of LBAM-fabricated parts is a very challenging research problem since—for the same level of relative density—size, shape and distribution of the voids can dominate the mechanical properties of the final parts. Moreover, experimental data reveals that some tensile properties of LBAM-fabricated parts—such as elongation-to-failure—have significant negative correlation with the part relative density. In other words, improving the relative density of parts does not necessarily guarantee improving other mechanical properties of parts in the optimal relative density window. Hence, they may not be optimized simultaneously. In other words, optimizing multiple mechanical properties of LBAM-fabricated parts is a multi-objective optimization problem. Most of the existing experimental approaches are not well-suited for this research problem since they cannot incorporate several conflicting responses of interest. Moreover, conventional multi-objective optimization methodologies are not applicable in this case because the functional form of objective functions is unknown and impossible to achieve due to the extremely high experimental cost in LBAM processes.

1.2 Proposed solutions

1.2.1 Accelerated Process Optimization (APO) of LBAM-fabricated parts by leveraging data from similar—but non-identical—studies

Chapter 3 proposes a novel process optimization method that directly utilizes experimental data from previous studies—as the initial experimental data—to guide the sequential optimization experiments of the current study. Most of the existing LBAM studies do not use a systematic approach to optimize process parameters (e.g., laser power, laser velocity, layer thickness, etc.) for desired part properties. The proposed methodology

serves to reduce the total number of time- and cost-intensive experiments needed. We verify our method and test its performance via comprehensive simulation studies that test various types of prior data. The results show that our method significantly reduces the number of optimization experiments, compared with conventional optimization methods. We also conduct a real-world case study that aims to optimize the relative density of parts manufactured using a Selective Laser Melting (SLM) system. A combination of optimal process parameters is achieved within five experiments. Note that the proposed method—Accelerated Process Optimization (APO)—is not limited to the SLM system or optimization of relative density. The APO can be readily applied to optimize any individual characteristic of AM parts fabricated using any AM system.

1.2.2 Multi-objective Accelerated Process Optimization (m-APO) for optimizing geometric accuracy of AM-fabricated parts

Chapter 4 is dedicated to minimizing geometric inaccuracies in AM-fabricated parts by optimizing the process parameters settings. This is a very challenging research problem, because it is often difficult to satisfy various specified geometric accuracy requirements by using the process parameters as the controlling factor. To overcome this challenge, the objective of this work is to develop and apply a multi-objective optimization approach to find the process parameters minimizing the overall geometric inaccuracies by balancing multiple requirements. The central hypothesis is that formulating such a multi-objective optimization problem as a series of simpler single-objective problems leads to optimal process conditions minimizing the overall geometric inaccuracy of AM parts with fewer trials compared to traditional DoE approaches. The proposed Multi-objective Accelerated Process Optimization (m-APO) method accelerates the optimization process

by jointly solving the sub-problems in a systematic manner. The m-APO maps and scales experimental data from previous sub-problems to guide remaining sub-problems that improve the solutions while reducing the number of experiments required. The presented hypothesis is tested with experimental data from a Fused Filament Fabrication (FFF) AM process; the m-APO reduces the number of FFF trials by 20% for obtaining parts with the least geometric inaccuracies compared to full factorial DoE method. Furthermore, a series of studies conducted on synthetic responses affirmed the effectiveness of the proposed m-APO approach in more challenging scenarios evocative of large and non-convex objective spaces. This outcome directly leads to minimization of expensive experimental trials in AM.

1.2.3 Multi-objective Accelerated Process Optimization (m-APO) for optimizing multiple mechanical properties of LBAM-fabricated parts

Chapter 5 is targeted at maximizing multiple mechanical properties of parts fabricated by LBAM systems. Process optimization of Laser-Based Additive Manufacturing (LBAM) systems is often complicated by the tradeoff between different mechanical properties as well as the relative density window. For instance, parts with similar relative densities can have noticeably different tensile mechanical properties (e.g., elongation-to-failure, yield strength, ultimate tensile strength, Young's modulus). This phenomenon can be attributed to the variation of size and distribution of fabrication-induced voids within the final parts. To overcome the aforementioned challenge, we apply an efficient sequential multi-objective process optimization framework to optimize the quality of LBAM-fabricated parts with respect to multiple non-correlated mechanical properties within the optimal relative density regime. The applied Multi-objective

Accelerated Process Optimization (m-APO) method indirectly accounts for the effect of size and distribution of voids on the final parts' mechanical properties. The m-APO decomposes the master multi-objective optimization problem into a sequence of single-objective sub-problems constructed from mathematically convex combination of individual unknown objective functions. At each step, the m-APO smartly maps the experimental data from previous sub-problems to the remaining sub-problems. Therefore, the information captured from previous sub-problems is leveraged to accelerate the master multi-objective process optimization problem. The m-APO exhibited capability to achieve a set of process parameter setups, resulting in the best trade-off between conflicting mechanical properties in the optimal window. The m-APO methodology is employed to maximize relative density and elongation-to-failure of Ti-6Al-4V parts fabricated by Selective Laser Melting (SLM) system. The results show that the m-APO achieves the optimal process parameter setups while reducing the time-and cost-intensive experiments by 51.8%, compared with an extended full factorial design of experiments plan. Note that the m-APO is not limited to the SLM system, Ti-6Al-4V material, maximizing relative density and elongation-to-failure of parts. In fact, it is a generic framework capable of optimizing any couple of scalar characteristics for AM-fabricated parts having negative correlation.

1.3 Dissertation organization

The remainder of this dissertation is organized as follows: in Chapter 2, a comprehensive literature review concerning the effects of LBAM process parameter and existing process modeling approaches in LBAM is conducted. Chapter 3 proposes a novel Accelerated Process Optimization (APO) methodology to efficiently optimize AM

processes with respect to a single characteristic of the final parts. In Chapter 4, a smart Multi-objective Accelerated Optimization (m-APO) framework is developed to optimize multiple geometric characteristics of parts in AM. In Chapter 5, the m-APO is modified and applied to optimize multiple mechanical properties of LBAM-fabricated parts. Finally, in Chapter 6 we outline the concluding remarks.

CHAPTER II
A REVIEW ON LASER-BASED ADDITIVE MANUFACTURING PROCESS
OPTIMIZATION

2.1 Introduction: effects of parameters

The optimization of Laser-Based Additive Manufacturing (LBAM) processes requires the understanding and characterization of the relation between a vector of process control parameters \mathbf{x} and a vector of response \mathbf{y} , which can be mechanical properties such as porosity, fatigue, yield strength, etc., or in-process variables, such as melt-pool dimensions, deposit height, etc. Since the mechanical properties of LBAM parts depends on the process parameters, which affect the microstructural distribution via thermal history, it is important to optimize the LBAM process parameters to generate near-net-shaped parts with minimal defects. The significance of LBAM process optimization is two-fold: (i) the optimized process parameters can then be utilized for effectively “seeding” a thermally-monitored, feedback-controlled LBAM process, which may result in LBAM parts with improved and/or customized properties; and (ii) it facilitates the research in material science to accumulate suitable AM processing data for various metallic materials, since comprehensive knowledge is involved in AM processes, including laser technology, material science, and solidification.

Despite the recent advances in LBAM technologies, the expense of running a large number of experiments remains non-trivial. Optimal process parameters are typically determined via extensive experiments, which usually require high experimental costs and a significant time investment. Due to the high machine, materials, operation costs, single experimental studies of LBAM part density could cost thousands of dollars, if not more, and take up to weeks. Moreover, this type of trial-and-error approach may never uncover the functional relationship between the process parameters \mathbf{x} and part features \mathbf{y} , and therefore, may never estimate the optimal combinations for process control parameters.

Two types of methods/models have been used to address the challenge of LBAM process optimization: (i) physics-based models that seek to characterize the underlying thermo-physics deposition process of LBAM; (ii) data-driven methods that target identifying the patterns in the existing experimental data through design of experiments and empirical modeling. For both approaches, the goal is to identify the functional relationship;

$$\mathbf{y} = f(\mathbf{x}) + \epsilon \quad (2.1)$$

where f represents the unknown relation between process parameters \mathbf{x} and LBAM response \mathbf{y} ; and ϵ represents the random error and uncertainty associated with the process.

Characterizing the functional form of f , i.e., the underlying phenomena that govern the LBAM process is non-trivial because several LBAM process parameters may affect the response vector of the part, which include, but are not limited to, laser power, laser velocity, laser scanning strategy, etc. For instance, laser power and laser velocity affect the melt-

pool shape and incident energy, and consequently, the cooling rate and local thermal gradients, and eventually the mechanical properties of parts.

In what follows, we summarize the effects of a number of key process parameters on the thermal history and mechanical properties of LBAM parts to delineate the complex relationship between process parameters and microstructural/mechanical properties. A more detailed discussion about the effects of various process parameters can be found in Ref. [5,11].

2.1.1 Laser power and laser velocity

The combination of lower laser power and higher laser velocity results in lower incident energy at the top of the part, which in turn leads to higher cooling rate as well as finer microstructure [5]. Conversely, a lower cooling rate and coarser microstructure can be achieved by increasing laser power and decreasing laser traverse speed [5]. Lower incident energy, which can be due to laser attenuation and/or radiation effects, tends to result in finer equiaxed morphologies. By contrast, higher incident energy generally results in a coarser microstructure and columnar grains [5]. Since the cooling rate (and consequently the solidification rate) increases toward the surface of the deposit, a transition from columnar to mixed equiaxed-columnar microstructure has been observed at the surface of the deposit. Therefore, various combinations of laser power and laser velocity may result in differential microstructure, morphology and thus mechanical properties.

2.1.2 Layer height

Layer height influences the microstructure and mechanical properties, as well as the geometric accuracy, of LBAM fabricated parts. Layer height is affected by different

factors for different powder deposition mechanisms: For Laser-based Powder Bed Fusion (PBF-L) processes, also referred to as Selective Laser Melting (SLM), a uniform bed of powder is first spread on the previous layer or substrate by a roller or re-coater blade, and then specific regions of the bed are selectively melted by a laser beam in order to build a single layer of the part. Upon the completion a layer, the powder bed is lowered by the height of the deposited layer (layer height), and a new layer of powder is deposited with the roller. In this case, the layer height is mainly determined by the thickness of powder and may be accurately controlled. For Direct Energy Deposition (DED) processes, such as Laser-Engineered Net Shaping (LENS), the amount of powder forming a layer is mainly determined by the amount of powder injected into the melt-pool (deposited mass flow rate). The resulting powder density distribution in the melt-pool is then the most important factor for layer height control. Thus, characterizing the effect of process control parameters on the layer height is equivalent to modeling their effects on the amount of the powder injected into the melt-pool and its distribution. In general, the layer height increases as the powder feed rate increases. Powder feed rate interacts with other parameters, such as laser power and traverse velocity. A higher laser power coupled with lower powder feed rate may result in increased porosity; and vice versa.

2.1.3 Deposition pattern

There are four common deposition patterns used in LBAM: raster, bi-directional, offset, and fractal patterns. The offset patterns can be further divided into two types, offset-out and offset-in, depending on the direction and starting point of deposition, as shown in Figure 2.1. The raster pattern is the most commonly used because of its ease of implementation [5]. The choice of laser scanning path of the raster pattern does not depend

on the geometry of the part. However different deposition patterns significantly affect the geometric and mechanical properties of the fabricated parts [5]. Choosing the appropriate scanning patterns reduce the incidence of residual stresses and thermal distortions. Moreover, the fractal and offset-out deposition patterns generate the smallest and second smallest substrate deformations, respectively, according to Ref. [12]. Despite the advantageous resultant mechanical properties and geometric accuracy, applying offset or fractal patterns requires additional customization of deposition path per part geometry, which is very challenging for a part with complex geometry.

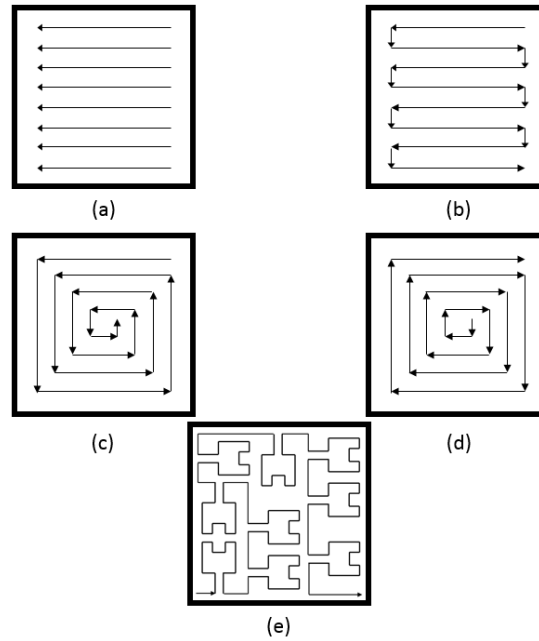


Figure 2.1 Different deposition patterns.

Raster, (b) Bi-directional, (c) Offset-in, (d) Offset-out, and (e) Fractal Post-manufacturing processing [12].

Post-manufacturing processes, such as hot isostatic pressing (HIP), may be used to enhance physical and mechanical properties of LBAM parts. HIP is a manufacturing

process used for reducing the porosity, and increasing the density of materials, by exposing the part to elevated temperature under constant/isostatic gas pressure. As reported by Ref. [11] adequate densification of LENS Ti-6Al-4V can be accomplished through HIP—leading to a higher ductility and elongation-to-rupture. Furthermore, the high temperatures experienced during the HIP process cause an increase in the alpha-platelet thickness of Ti-6Al-4V, which consequently reduces the strength of the material. In addition, HIP'ed specimens exhibit less anisotropic behavior than heat treated ones. Such observations indicate that porosity may play a significant role in the anisotropic behavior of laser-deposited parts. In general, the effects of different manufacturing and post manufacturing parameters on the anisotropic behavior of laser-deposited parts are not yet well understood; thus, further investigations are required.

2.2 Physics-based Models

Because of the layer-by-layer additive nature of LBAM, the complex thermal histories are experienced repeatedly in different regions of the deposited layers, which normally involve melting as well as numerous reheating cycles at a relatively lower temperature. Such complicated, cycling thermal behavior during LBAM results in the complex phase transformations and microstructural developments, and consequently exist significant difficulties in obtaining targeted optimal mechanical properties. On the other hand, the use of a finely focused laser to form a rapidly traversing melt-pool may result in considerably high solidification rate and melt instability. Complicated residual stresses tend to be locked into the parts during the building process, due to the thermal transients encountered during solidification. Understanding of the parameter-thermo-mechanical relationship facilitates the optimization of the LBAM process and thus final mechanical

properties. Actually, a series of complex thermo-mechanical phenomena including heat transfer, phase changes, mass addition and fluid flow are involved in the melt-pool during LBAM. Therefore, physics-based models developed based on the knowledge of temperature, velocity and composition distribution history is essential for an in depth understanding of the process, and subsequent mechanical properties.

2.2.1 Buckingham's II theorem

Determining the effects of process parameters on the LBAM process is challenging because the high dimensionality of the parameter space and their interaction amongst each other. In other words, each process parameter may not be singled out and studied individually because its impact on the microstructure and mechanical properties of LBAM parts depend on the values/levels of other process parameters. Buckingham's II (Pi) theorem provides a key tool in dimensional analysis for reducing the dimensionality of the process parameter space and a guideline in identifying the maximal number of dimensionless parameters, needed to characterize the process. The main idea is that if there is a physically governing equation involving a certain number, say n , of physical variables, and k is the number of fundamental dimensions (such as time, location, density, etc.) required to describe these n variables, then the original expression is equivalent to an equation involving a set of $p = n - k$ dimensionless parameters constructed from the original variables. Buckingham's II theory suggests the number of dimensionless parameters that can be constructed but the dimensionless parameters generated via Buckingham's theory are not unique, and there exist multiple choices for the selection of these dimensionless parameters. In most cases, researchers select dimensionless parameters that are useful in understanding the underlying process physics. Possible

choices of dimensionless parameters include melting efficiency, deposition efficiency, process efficiency, laser absorptivity, specific energy, and others. The utilization of common thermo-fluidic dimensionless numbers, such as Re , Pr , Bo , is also sought as these classical numbers can provide physical insight into various aspects of the LBAM process. As an example, one can find the Reynolds number for the melt-pool to help in assessing if laminar or turbulent flow exists.

- **Example 1.: Buckingham's II theorem [13]**

Determining the effects of LBAM process parameters on the quality of the final parts requires an extensive experimental study for various combinations of process parameters, as listed in Table 2.1. The parameters taken into account include materials, laser, product, process, and environment, resulting in a parameter space with high dimensionality (e.g., 19 parameters). Nevertheless, even such a high dimensional parameter space only includes a number of major parameters, and does not incorporate all the factors that could affect the LBAM process. For example, the effects of the powder delivery system (e.g. powder feeding location) and the shielding and carrier gases are not considered. The distribution of the laser irradiance at the focal spot and the position of the focal spot relative to the melt surface are not taken into account. Considering the high dimensionality, fully characterizing the effect of process parameters on the LBAM process would be very challenging. Any possible reduction of the parameter space will significantly improve the efficiency of the study.

Table 2.1 Parameters for metal deposition.

Material	Density, ρ	Thermal Conductivity, k	Solidification Time, t_s	Viscosity, μ	Heat Capacity, c_p	Surface Tension, σ	Melting Energy, E_m
Laser	Beam Diameter at Focus, d_f	Power, P					
Product	Height of Deposit, h_D	Width of Deposit, w					
Process	Delivered Mass Flow Rate, m_{del}	Deposited Mass Flow Rate, m_{dep}	Energy Loss to Environment, E_l	Translation Speed, v_s	Powder Size, d_p	Initial Powder Temperature, T_i	Powder Stream Speed, v_p
Environment	Gravity, g						

Kahlen and Kar [13] reduced the number of parameters by combining some of the process parameters and by identifying similar parameters using Buckingham's II-Theorem. With a basis of five dimensions (i.e., time, length, mass, temperature, and energy), Buckingham's II-theorem groups the original 19 process parameters into 14 ($= 19 - 5$) dimensionless numbers to characterize the process, as shown in Table 2.2. These resulting dimensionless numbers—which included Reynold's number (Re), Bond number (Bo), Prandtl's number (Pr) and various process “efficiencies”—aid in constraining the process parameter dimension and help in reducing the number of experiment required to optimize the process.

The advantage of using dimensionless parameters is that these parameters are usually defined based on LBAM processes, instead of materials to be processed or geometries of parts to be fabricated. Thus, dimensionless parameters are less dependent on material properties and part geometries. In practice, when a material is to be processed or when a part is to be built, dimensionless parameters can be used to suggest the range of parameters in which good metal parts are formed. Furthermore, the use of dimensionless

parameters can alleviate the confusion of dealing with various units for a single process parameter. For example, the units utilized for traverse speed can vary substantially (e.g. inches/minute, cm/s, etc.). Utilization of a dimensionless traverse speed allows for easier communication of process parameters amongst the international community.

Table 2.2 Dimensionless parameters.

Similarity parameter	Expression
Energy Loss Efficiency	$\eta_L = \frac{E_l}{P}$
Melting Efficiency	$\eta_m = \frac{E_m}{P}$
Superheating Efficiency	$\eta_x = \frac{E_x}{P}$
Powder Delivery Efficiency	$\eta_P = \frac{m_{dep}}{m_{del}}$
Bond Number	$Bo = \frac{\rho d_F^2 g}{\sigma}$
Froude Number	$Fr = \frac{v_P^2}{g d_F}$
Galileo Number	$Ga = \frac{g d_F^3 \rho^2}{\mu^2}$
Prandtl Number	$Pr = \frac{c_p \mu}{k}$
Reynolds Number	$Re = \frac{v_P \rho d_F}{\mu}$
Length Scale of the Melt-pool	$L_P = \frac{v_s t_s}{d_F}$
Powder Particle Number Density in the Melt-pool	$N = \left(\frac{d_P}{d_F}\right)^2$
Melt-pool Shape Factor	$S_P = \frac{v_P}{v_s}$
Product Aspect Ratio	$A_S = \frac{h_D}{w}$
Powder Dissolution Factor	$D_P = \frac{4k(T_a - T_i)d_F}{E_m}$

2.2.2 Process characterization

One well-established method for developing dimensionless parameters is process maps that can be used to understand the LBAM process parameters and their impact on the thermal history and microstructure of the part. Process maps possess dimensionless ordinates to help in determining the effects of laser velocity, part preheating, laser power, etc.; and are generalized for the moving heat source problem (e.g. Rosenthal's solutions) inherent to LBAM processes. Plots are generated based on analytical, numerical or experimental results, which can be used as tools to aid LBAM users in ascertaining the appropriate, initial process parameters for a given material for fabrication via LBAM.

2.2.3 Steady state thermal maps

Early research of process maps mainly focuses on predicting the steady-state melt-pool size for various practical combinations of process parameters. During LBAM, the laser beam creates a moving melt-pool on the substrate in which powder is melt. The melt-pool size has been identified as a critical parameter for maintaining optimal building conditions. The formation of steady melt-pool with a small heat affected zone and an uninterrupted solidification front tends to result in homogeneous part quality. A typical steady-state thermal process map can demonstrate how melt-pool length is affected by normalized height of substrate and melt temperature. These steady-state process maps have been used for determining process parameters that result in desired melt-pool lengths. An advantage of the steady-state process maps is its ease of implementation: the relations between dimensionless process parameters and the melt-pool lengths are contained in the form of a single three-dimensional or two-dimensional plot that process engineers can use directly.

2.2.4 Thermal maps for transient analysis

Thermal process maps have also been developed to conduct transient analysis, accounting for dynamics LBAM processes and their effects on, for example, melt-pool/track morphology. One typical dynamic LBAM process is the so-called “boundary issue”, which results in an increase in the melt-pool size as the boundary of each layer is approached. The boundary problem is mainly caused by the fact that the laser velocity reduces, and thus the energy density increases, to accurately deposit materials near the boundary of layers. In addition, a velocity reversal is needed to continue with deposition of the next layer of material. Efficient and effective optimization of the melt-pool size/morphology and other process parameters requires comprehensive understanding of how the melt-pool size changes over a range of process size scales, as well as various laser power or velocity. In other words, a transient analysis allows one to determine how changes in process parameters affect the melt-pool geometries, as well as the cooling rates, thermal gradients, etc.

2.2.5 Process maps for different scales of LBAM systems

Whenever a new laser-based manufacturing system is developed at a different size scale, engineers must perform a large number of experiments to characterize their process. It is important to obtain fundamental understanding of how to apply deposition knowledge acquired from small-scale systems—e.g., Laser Engineering Net Shaping (LENS) equipped with a 500W Nd:YAG laser, or other similarly sized lasers—to analogous large-scale systems—e.g., AeroMet, which manufactures components for the aerospace industry and uses an 18kW CO₂ laser. Multiple process maps with various scales have been developed for predicting part features for the large scale process via extrapolation by Ref.

[14]. The authors showed that the process maps can be applied over multiple process size scales by simply using dimensionless parameters, i.e., by changing the normalization temperature with changes in power range. Although the resulting prediction can be used to provide a possible range for the optimal process parameters in large-scale LBAM processes, the prediction may be inaccurate due to the error caused by model extrapolation. Therefore, there exists a great need to fill the gap between industrial applications that demand the use of large-scale deposition processes and the process development that occurs on small-scale processes in the laboratory conditions.

2.2.6 Limitation of process maps

Process maps are advantageous in that they provide a fundamental way to predict and thus control melt-pool size, stress and material properties by presenting results in a form that process engineers can readily use. Bontha et al. [15] further generalized the thermal process maps to establish the relation between dimensionless process parameters and solidification cooling rates in laser deposition processes, namely solidification maps. The simultaneous control of residual stress and melt-pool size has also been addressed by Ref. [16]. However, there also exist two major limitations in the existing process map methods. First, the current process maps are for limited part geometries—developed for thin-wall and bulk shapes only. In other words, these process maps do not hold for other common shapes, let alone parts with complex geometries. One promising application of AM is to fabricate parts whose geometry is so complex that they cannot be produced using traditional manufacturing methods. Therefore, in order to make process maps useful in real-world manufacturing applications, future work is needed to develop process maps that characterize the thermal behaviors and mechanical properties of parts with various

geometries. Secondly, process maps do not consider temperature-dependent material properties. Current process maps are based on Rosenthal's analytical solution for temperature with moving-heat-source boundary, and material properties are assumed independent of temperature. This may not be realistic assumption in real world applications. In fact, process maps are used to approximate the underlying fabrication process when the temperature remains in a certain range.

2.3 Data-driven optimization methods

Although physics-based models are essential for thoroughly understanding the underlying LBAM processes, their development is extremely challenging due to the complexity associated with LBAM. Some research efforts have circumvented this challenge by utilizing data-driven methods that directly model how the process parameters affect the quality of final parts. Data-driven approaches involve (i) choosing an experimental design for generating data, and (ii) choosing a model to fit the data. In particular, existing research for the optimization of LBAM parts primarily rely on a trial-and-error procedure to determine optimal process parameters and achieve targeted properties of the fabricated product. Statistical design of experiments (DoE) provides a systematic framework to utilize the previous experimental data and plan future experimental trials with the minimal cost. An experimental design represents a batch or sequence of experiments to be performed, expressed in terms of factors (design variables) set at specified levels. Based on the experimentation data, simplified/approximated relations between part features and process parameters can be learned in an empirical way. Properly designed experiments and subsequent data modeling are essential for effective experimental analysis and process optimization. A common feature shared by data-driven

methods is that process parameters and part features (e.g., mechanical properties) are empirically related based on experimental data sets. In other words, the developed methods are not completely dependent on the domain knowledge of a specific process and thus may be applied to other processes. Below, we review DOE methods together with the corresponding data models that have been applied for LBAM studies, as well as those can be potentially applied.

2.3.1 Full factorial designs

The most basic experimental design is a full factorial design. The main idea is to replicate all possible combination of the levels of the factors in each run of experiments. The number of design points dictated by a full factorial design is the product of the number of levels for each factor. For instance, if there are 2 factors, each with ℓ levels, each experimental run would investigate ℓ^2 design points. More generally, when there are k factors, each with ℓ levels, the total number of design points is ℓ^k . The most common are 2^k (for evaluating main effects and interactions) and 3^k designs (for evaluating main and quadratic effects and interactions) for k factors at 2 and 3 levels, respectively. A 2^3 full factorial design is shown in Figure 2.2.

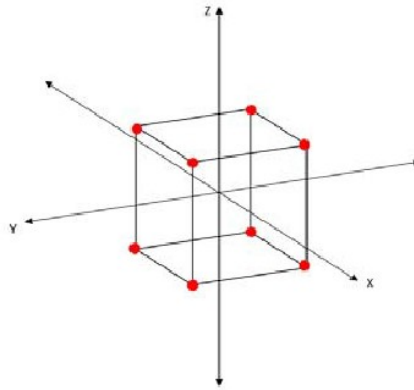


Figure 2.2 2^3 designs.

The main effect of a factor refers to the resulted change in the response variable by changing the level in factor of interest. Figure 2.3 illustrates an example of a 2^2 design. Two levels are denoted by "+" and "-" representing "high" and "low" levels for the factors of interest, respectively. The main effect of a factor of a factorial design is defined as the difference between the average response values at high and low level of the factor of interest. In this example, the main effect of factor M is calculated as follows: Main Effect of Factor $M = (31 + 41)/2 - (15 + 25)/2 = 16$. The effect of a factor may depend on the level of others. In the case, there exists an interaction between these factors. Following the previous example, the magnitude of the interaction between factors M and N (i.e. MN effect) is calculated as $MN = ((39 - 21) - (11 - 27)) / 2 = 17$.

There are various ways to mathematically formulate factorial designs. For instance, a regression-type model can be developed to capture the main effects and interactions of two-factor as shown in Eq. 2.2.

$$y = \alpha_0 + \alpha_1 x_1 + \alpha_2 x_2 + \alpha_{12} x_1 x_2 + \epsilon \quad (2.2)$$

where y represents the response value, α_i 's are the coefficients which should be estimated, x_1 and x_2 are variables representing scaled values (1 and +1 representing low and high levels) of factors M and N , respectively. Also, $x_1 x_2$ represents the interaction term between factors; and ϵ is the random error. After forming the model, statistical methods (such as ANOVA) can be employed to analysis and determine the statistical significance of each factor and interactions as well as conventional statistical tests and interpretations.

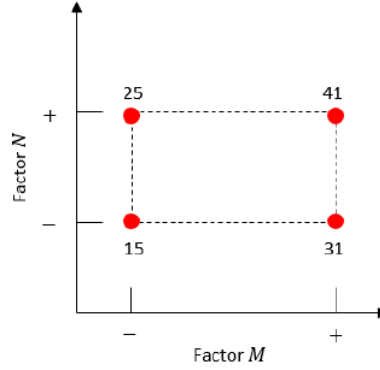


Figure 2.3 2^2 designs.

2.3.2 Fractional factorial design

The combinations of design points in full factorial design increase exponentially along with the number of factors. Hence, full factorial designs may not work well for cases in which a moderate-to-large number of factors are involved. Moreover, each design point should be replicated several times in order to make the experimental design capable of detecting the significant effects, leading to an unmanageable number of experiments. Fractional Factorial Design is a potential alternative when the experiments are expensive to run and a large number of factors and levels are involved. A fractional factorial design is a fraction of a full factorial design, which aims to select a portion of all possibilities to reduce the number of required experiments. The general form of ℓ -level fractional factorial design is ℓ^{k-p} , where $k - p$ is the fraction of original full factorial design which is to be run. For instance, a half fraction of 2^3 full factorial design includes $2^{3-1} = 4$ design points which are illustrated in Figure 2.4.

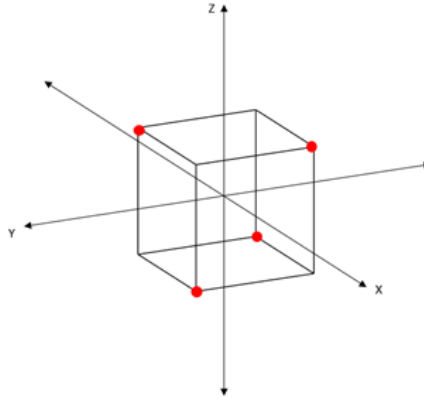


Figure 2.4 Fractional factorial designs.

Reducing the design space by shifting from full to fractional factorial design is also accompanied by an inevitable cost in terms of detecting the significant effects. For instance, applying 2^3 full factorial design, not only considers all main effects (x, y, z) and all two factor interactions (xy, xz, yz), but also it accounts for three factor interactions (xyz). On the other hand, half fraction of 2^3 full factorial design does not allow for estimation of three factor interactions. The interaction effects cannot be ignored unless they are known (or assumed) to be insignificant. An example of the application of 2^{l-p} design can be found in the example below:

Example 2: Two-level fractional factor design [17]

Laser Engineered Net Shaping (LENS) is an Additive Manufacturing (AM) process that can build complex, functional parts in metal, by slicing 3D objects into 2D layers of user-defined thickness and superimposing successive layers. Users must choose the layer thickness and match it with the deposition to keep the laser in focus throughout the build. If a mismatch exists between the layer thickness and the deposited thickness, the laser is

no longer focused on the melt-pool surface, leading to geometric inaccuracy of parts, or even failures of build. The deposition thickness is typically governed by other process parameters, such as laser power, laser velocity, hatching spacing, powder mass flow rate, etc. To match the layer thickness with deposition, it is very important to understand and estimate the relationship between these process parameters and the deposition thickness so that the layer thickness can be optimized based on the chosen process parameters.

Kummailil et al. [17] studied the effects of process parameters on deposition thickness and applied a two-level fractional factorial designs to develop empirical relationships between process parameters and deposition. Experiments were performed on a LENS 850 system using Ti-6Al-4V powder. The geometry of testing parts was a rectangular block with a width of 12.7mm, length of 19.1mm, and height dependent on the layer deposited (because the build may fail if the specified layer thickness mismatches the deposition). Two levels, high (+) and low (−), are chosen for each process parameter, as shown in Table 2.3. The minimum number of experiments needed is $2^4 = 16$. Experiments were performed according to the design matrix, as shown in Table 2.4, and the deposition thickness was measured for each testing sample.

Table 2.3 Levels of Process Parameters.

Process parameter	−	+
Laser power (W)	250	350
Laser velocity (mm/s)	16.9	27.5
Hatch spacing (um)	381	457
Powder mass flow rate (mg/s)	38	73.4

Table 2.4 Design matrix of factorial design.

Design point	Laser power	Laser velocity	Hatch spacing	Powder mass flow rate
1	—	—	—	—
2	—	—	—	+
3	+	—	—	—
4	+	—	—	+
5	—	+	—	—
6	—	+	—	+
7	+	+	—	—
8	+	+	—	+
9	—	—	+	—
10	—	—	+	+
11	+	—	+	—
12	+	—	+	+
13	—	+	+	—
14	—	+	+	+

The main effects of process parameters on deposition thickness are presented on Table 2.5. Laser power and mass flow rate have positive effects on deposition, whereas, hatch spacing and laser velocity have negative effects on deposition. Mass flow rate and laser velocity have more significant impacts on deposition, whereas, hatch spacing shows a less significant effect; and laser power has the smallest impact on deposition thickness. Therefore, to achieve the targeted deposition thickness, powder mass flow rate and laser velocity may be the most effective parameters to adjust, based on experimental data.

Table 2.5 Main effects of parameters.

Parameter	Laser power	Laser velocity	Hatch spacing	Powder mass flow rate
Main effect	6.97	29.01	-12.36	30.56

An empirical model can also be developed based on the experimental data. Since two major factors affecting the build process are material and energy (specifically, process

parameters affect the deposition by changing either the energy or amount of material available in the melt-pool area), the four process parameters can be grouped into two categories: (i) the energy density at the melt-pool and (ii) the powder flow rate. An empirical model was developed between deposition (μm) and the product of energy density (J/mm^2) and mass flow rate (g/s):

$$\text{deposition} = \beta \times \text{energy density} \times \text{mass flow rate}$$

The R^2 value of the fitted model is found to be 0.85, which indicates the goodness-of-fit of this linear model.

Fractional factorial designs are useful for screening factors to identify those with the greatest effects when a large number of factors are involved. In practice, it is usually assumed that the system is dominated by main effects and lower order interaction effects (e.g. quadratic effects). One specific family of fractional factorial designs vastly applied for screening are two level Plackett-Burman (PB) designs. These are used to study $k = n - 1$ factors where n is an integer multiple of 4. By ignoring the interactions between factors, PB designs allow for using only one more design point than the number of factors to obtain unbiased estimation of main effects. To estimate quadratic effects, $3k$ or $3(k - p)$ designs can be used but often require an unmanageable number of design points. The most common second-order designs, configured to reduce the number of design points, are central composite and Box-Behnken designs. A central composite design (CCD) is a two level factorial design, augmented by n_0 center points and two "star" points positioned at \pm for each factor. Box-Behnken designs use the smallest number of factor levels in an experimental design. These are formed by combining 2^k factorials with incomplete block designs. They do not contain points at the vertices of the hypercube defined by the upper

and lower limits for each factor. This is desirable if these extreme points are expensive or impossible to test. More information about central composite and Box-Behnken designs can be found in Ref. [18].

2.3.3 Taguchi design

Taguchi design provides a balanced design of experiments that lays out the factors' levels in an equally weighted way. Taguchi design is an efficient method because it provides enough information by designing just a few design setups, and may be used a robust alternative to two or three level fractional factorial designs. The Taguchi design uses three sequential steps: (i) system design, which incorporate domain knowledge, (ii) parameter design, which optimizes the settings of process parameters, and (iii) tolerance design, which determines and analyzes tolerances around the optimal parameters. This subsection focuses on parameter design, which is a key step that incorporates statistical design of experimentation. Taguchi (parameter) design is developed based on the idea of orthogonal arrays. For a system with f factors, each with l levels, an orthogonal array is a N by k matrix denoted by L_N such that each possible combination of levels are repeated by the same number of times across the columns of this matrix. A more rigorous definition of orthogonality is that the inter product of any two columns the design matrix is zero. Each row of an orthogonal array represents an experimental design setup and the number included in the cells represents the level of each factor. The example of a L_4 design can be found in Table 2.6.

Table 2.6 L_4 design.

Experiment number	Factors and levels		
	f_1	f_2	f_3
1	-1	-1	-1
2	-1	1	1
3	1	-1	1
4	1	1	-1

Two levels, high and low represented by 1 and -1 respectively, are considered. There exists four possible combinations of factor levels: $(1, 1)$, $(1, -1)$, $(-1, 1)$, and $(-1, -1)$. For any two columns of the L_4 design matrix, each of four factor combinations appears exactly once. From another perspective, the inner product of any two columns is zero. Another example of 7-factor Taguchi design can be found in Table 2.7. Taguchi orthogonal arrays can be considered as a fraction of full factorial designs. Specifically, orthogonal array L_N is a $\frac{N}{\ell^k}$ fraction of ℓ -level full factorial design with k factors. For example, orthogonal array L_4 can be considered a half fraction of a 2^3 full factorial design. By applying Taguchi designs, the number of design points decreases from 8 to 4. These arrays are constructed to reduce the number of design points necessary; two-level L_4 , L_8 , and L_{12} arrays, for example, allow 3, 7, and 11 factors/effects to be evaluated with 4, 8, and 12 design points, respectively.

Table 2.7 L₈ design.

Experiment number	Factors and levels						
	f_1	f_2	f_3	f_4	f_5	f_6	f_7
1	-1	-1	-1	-1	-1	-1	-1
2	-1	-1	-1	1	1	1	1
3	-1	1	1	-1	-1	1	1
4	-1	1	1	1	1	-1	-1
5	1	-1	1	-1	1	-1	1
6	1	-1	1	1	-1	1	-1
7	1	1	-1	-1	1	1	-1
8	1	1	-1	1	-1	-1	1

Example 3: SLS shrinkage compensation [19]

Selective Laser Sintering (SLS) is a powder-based additive manufacturing (AM) process, in which parts are built by selective sintering of layers of powder using a CO₂ laser. SLS can be used to produce functional parts for various applications, such as aerospace, rapid tooling, etc. Shrinkage is a major issue that affects the accuracy of SLS parts. A common practice to resolve the issue of part shrinkage is to calculate or estimate the amount of shrinkage in each direction and apply the shrinkage compensation in the opposite direction in the digital model. Part shrinkage is found to be affected by various process parameters such as laser power, laser velocity, hatch spacing, powder bed temperature, scanning length, etc. To apply optimal shrinkage compensation to the digital file, it is important to identify the process parameters that govern part shrinkage in each direction, and understand the relation between process parameters and the amount of shrinkage. Raghunath and Pandey [19] designed experiments using the Taguchi method and used polymer powder to fabricate cuboids of 30mm × 30mm cross section with different lengths along the laser scanning direction (i.e., scanning length).

The ranges of process parameters were chosen based on the minimum and maximum energy density: $E = \text{Laser Power} / (\text{Laser Velocity} \times \text{Hatch Spacing})$. The energy density should be high enough so that sintering can occur. However, too high energy density may cause the degradation of material properties. Raghunath and Pandey [19] ascertained that the energy density should be at least 1 J/cm^2 for the sintering to occur; and that the polymer begins to degrade when the energy density is above 4.8 J/cm^2 . Hence, the range of energy density was set in the range of $(1\text{--}4.8) \text{ J/cm}^2$. The corresponding ranges of the laser power, laser velocity, and hatch spacing were selected to be 24–36 W, 3000–4500 mm/s, 0.22–0.28 mm, respectively. In addition, the powder bed temperature and scan length were also considered. Four levels of parameter values were considered for each process parameter. To select an appropriate orthogonal array, the total degrees of freedom need to be calculated. Four-level design results in 3 degrees of freedom for each of the 5 parameters. Plus one degree of freedom for the overall mean, the total degrees of freedom is $3 \times 5 + 1 = 16$. Hence, L_{16B} orthogonal array with 4 columns and 16 rows was used and is given in Table 2.8.

Table 2.8 L₁₆B orthogonal array.

Experiment number	Laser power	Laser velocity	Hatch spacing	Powder bed temperature	Scan length
1	1	1	1	1	1
2	1	2	2	2	2
3	1	3	3	3	3
4	1	4	4	4	4
5	2	1	2	3	4
6	2	2	1	4	3
7	2	3	4	1	2
8	2	4	3	2	1
9	3	1	3	4	2
10	3	2	4	3	1
11	3	3	1	2	4
12	3	4	2	1	3
13	4	1	4	2	3
14	4	2	3	1	4
15	4	3	2	4	1
16	4	4	1	3	2

Analysis of Variance (ANOVA) was used to analyze the shrinkage data in each direction to identify the parameters that has significant contributions to the total variance of shrinkage. If a factor is significantly influencing the process response (i.e., shrinkage in this example), the corresponding F-value would be large. For example, the ANOVA for the part shrinkage in the *X*-direction is presented in Table 2.9, which indicates the scan length and laser power have the most significant impact on part shrinkage. Similar analysis was performed to shrinkage in *Y* and *Z* directions. It was reported that laser power and laser velocity have significant effects on the shrinkage in *Y* direction, whereas, part bed temperature, laser velocity, hatch spacing are more significant for shrinkage in *Z* direction.

Table 2.9 ANOVA for shrinkage in *X*-direction.

Factor	DOF	Sum of Square (SS)	Mean Square (MS)	F-Statistics
Laser power	3	26.39	8.80	2.51
Laser velocity	3	18.51	6.17	1.74
Hatch spacing	3	2.29	0.76	0.21
Part bed temperature	3	10.80	3.60	1.01
Scan length	3	91.61	30.54	8.60
Error	6	31.60	3.55	
Total	15	149.59		

Linear empirical models are developed to characterize the relation between process parameters and part shrinkage, and estimate the shrinkage compensation in each direction. Only significant process parameters identified using ANOVA are included to develop the empirical models. For instance, the developed models for shrinkage compensation in *X*-direction is

$$S_X = 1.611691 - 0.01615 \text{ Laser power} - 0.009647 \text{ Laser velocity.}$$

Similar empirical shrinkage models are also developed for the *Y* and *Z* directions. The developed models predict the shrinkage in percentage for any combination of process parameters to scale up the digital file for optimal accuracy.

2.3.4 More advanced designs and modeling methods

2.3.4.1 Space filling designs

Besides these classical design-of-experiment methods, other designs exist, such as space filling designs that treat all regions of the design space equally. Space-filling designs are useful for modeling systems that are deterministic or near-deterministic, such as a

computer simulation, which involves many variables with complicated interrelationships. One criterion to fill the design space is to minimize the integrated mean squared error (IMSE) over the design space by using IMSE-optimal designs. Koehler and Owen [20] describe several Bayesian and frequentist space filling designs, including maximum entropy designs, mean squared-error designs, minimax and maximin designs, Latin hypercubes, randomized orthogonal arrays, and scrambled nets. A review of Bayesian experimental designs for meta modeling is given in Ref. [21].

2.3.4.2 D-Optimal designs

D-optimal design is another type of design, which is useful when classical designs (such as factorial and fractional designs) do not apply. In practice, standard factorial or fractional factorial designs may require too many runs for the amount of resources or time allowed for the experiment, or the design space may be constrained (the process space contains factor settings that are not feasible or are impossible to run). The design matrices generated by D-optimal designs are usually not orthogonal and effect estimates are correlated. These types of designs are always an option regardless of the type of model the experimenter wishes to fit (for example, first-order, first-order plus some interactions, full quadratic, cubic, etc.) or the objective specified for the experiment (for example, screening, response surface, etc.). However, D-optimal designs are developed based on a chosen optimality criterion and the possible underlying model that will be used to fit the experimental data. Specifically, D-optimal designs maximize the determinant of the information matrix. This optimality criterion results in minimizing the generalized variance of the parameter estimates for a pre-specified model. As a result, the “optimality” of a given

D-optimal design is model dependent. In other words, an approximation model must be specified before the generation of design points.

2.3.4.3 Response surface and Kriging

The response surface model (RSM) "is a collection of statistical and mathematical techniques useful for developing, improving, and optimizing process" [22]. Since the true response surface function $f(x)$ is usually unknown, a response surface $g(x)$ is created to approximate $f(x)$. Low-order polynomial models are usually popular choices for the response surface $g(x)$. Depending on the needed curvature, various polynomial models can be developed. The more curvature needed to be incorporated, the higher-order polynomial models are required.

After identifying the factors that have significant impacts on the response, the general RSM approach includes all or some of the following steps:

(1) First-order experimentation: when the starting point is far from the optimum point or when knowledge about the space being investigated is sought, first-order models and an approach such as steepest ascent are used to "rapidly and economically move to the vicinity of the optimum" [18]. The general form of first-order model is expressed as below:

$$g(x) = \alpha_0 + \sum_{i=1}^k \alpha_i x_i$$

The 3D response surface and 2D contour plot of a linear response surface model are demonstrated in Figure 2.5 and Figure 2.6, respectively. The resulting response surface is a plane over the 2D design space. The first-order model is also called main effect model because it focuses on the main effects of the process parameters. Other than the main

effects, interactions between the process parameters can be incorporated in the response surface model:

$$g(x) = \alpha_0 + \sum_{i=1}^k \alpha_i x_i + \sum_{i < j} \sum_{j=2}^k \alpha_{ij} x_i x_j$$

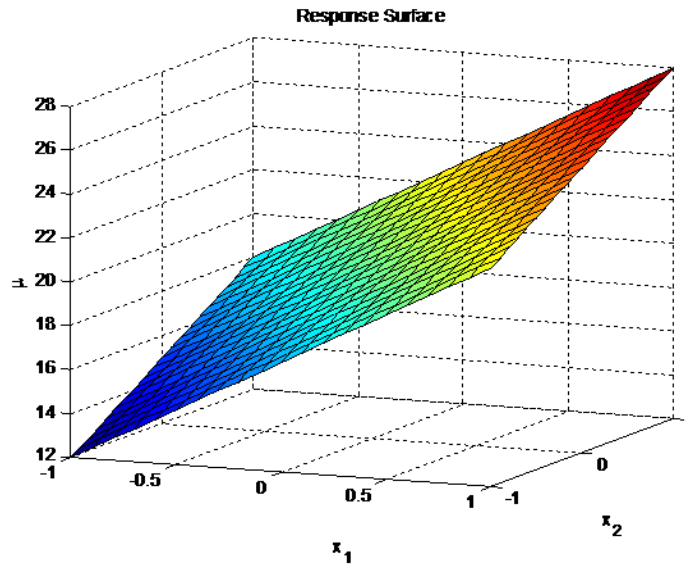


Figure 2.5 Response surface of $g(x) = 20 + 5x_1 + 3x_2$.

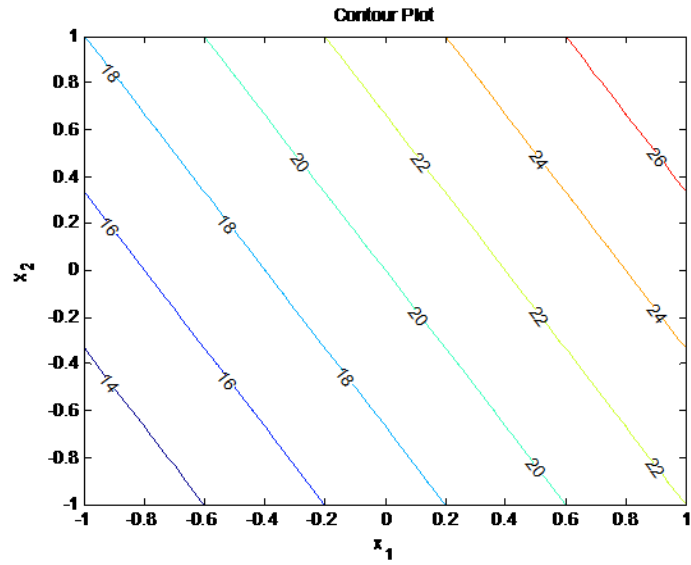


Figure 2.6 Contour plot of $g(x) = 20 + 5x_1 + 3x_2$.

Following the previous example, the 3D response surface and 2D contour plot of the first-order response surface model, with the consideration of parameter interaction, are demonstrated in Figure 2.7 and Figure 2.8, respectively. As shown in figures, the incorporation of the interaction term has imposed curvature to the response surface.

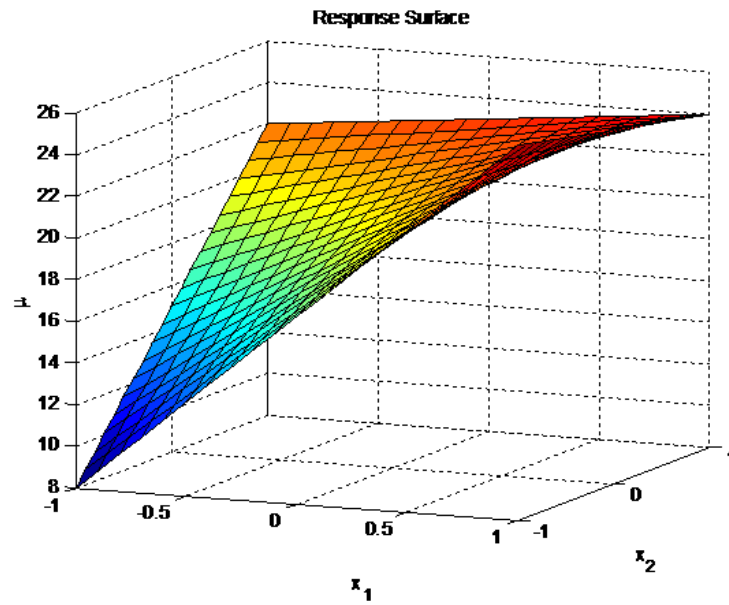


Figure 2.7 Response surface of $g(x) = 20 + 5x_1 + 3x_2 - x_1x_2$.

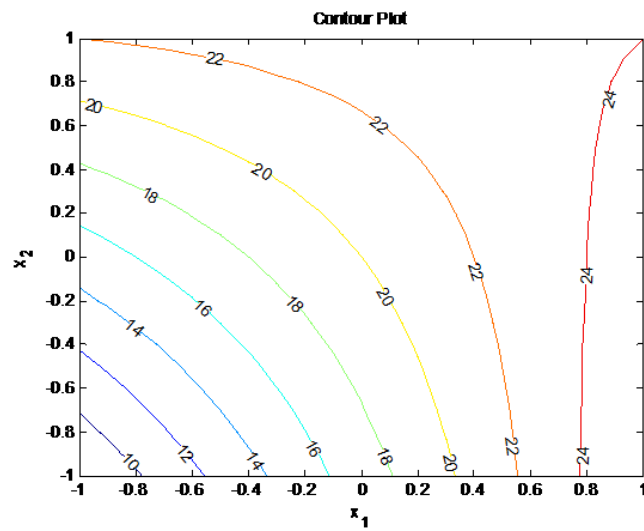


Figure 2.8 Contour plot of $g(x) = 20 + 5x_1 + 3x_2 - x_1x_2$.

(2) Second-order experimentation: after the best solution using first order methods is obtained, a second order model is fit in the region of the first order solution to evaluate curvature effects and to attempt to improve the solution. The general form of second-order model is as follows:

$$g(x) = \alpha_0 + \sum_{i=1}^k \alpha_i x_i + \sum_{i=1}^k \alpha_{ii} x_i^2 + \sum_{i < j} \sum_{j=2}^k \alpha_{ij} x_i x_j$$

The parameters of the polynomials models are usually determined by least squares regression analysis by fitting the response surface approximations to existing data. These approximations are normally used for prediction within response surface methodology (RSM). A polynomial model may not seem a reliable and precise model for approximating the non-linear functions of arbitrary shape over the whole design space; however, it is accurate enough for approximating relatively small portion of the true function, and it is difficult to take enough sample points in order to estimate all of the coefficients in the polynomial equation, particularly in high dimensions. A complete discussion of response surfaces and least squares fitting is presented in Ref. [22].

Similar to the response surface model, the method of Kriging may also be used to characterize the responses as a combination of a polynomial model plus localized departures, characterized by a Gaussian process. Based on the observed experimental data and a covariance structure, the kriging method can predict the response value for any unobserved parameter setup. The kriging parameters can usually be estimated using the method of Maximum Likelihood Estimates. Detailed discussion of parameter estimation can be found in Ref. [23]. For small problems with relatively few sample points, fitting a kriging model is rather trivial. However, as the size of the problem increases and the

number of sample points increases, the added effort needed to obtain the “best” kriging model may begin to outweigh the benefit of building the approximation. Besides, prediction with a kriging model requires the inversion and multiplication of several matrices which grow with the number of sample points. Hence, for large problems prediction with a kriging model may become computationally expensive as well.

2.3.4.4 Artificial intelligence

Another category of data-driven methods that have been applied for AM process optimization is artificial intelligence (AI), which aims at “training” a black-box model based on a large training data set. More detail about the fundamentals of AI methods can be found in Ref. [24]. These algorithms include, but are not limited to, Support Vector Machine, Neural Network, Bayesian Network, and their extensions. With a large training data set, AI algorithms usually provide accurate estimations of parameter-feature relations. For instance, Lu et al. [25] applied the method of least square support vector machine (LS-SVM) to investigate the relation between mechanical properties of parts and process parameters such as laser power, traverse speed, and the powder feed rate in LENS. Validated by using fabricated thin-walled parts, the method of LS-SVM is reported to accurately predict the deposition height when a large sample of parts is used to train the model. Similar successful applications of AI methods were performed by Casalino and Ludovico [26], which uses Feed Forward Neural Network (FFNN) to model a laser sintering process, and by Wang et al. [27] which adopts Bayesian Probability Network to characterize a laser bending process. DLD process optimization for controlled layer height can also be accomplished using advanced/intelligent computational methods such as the Mutable Smart Bee Algorithm (MSBA) and Fuzzy Interference System (FIS), and

unsupervised machine learning approaches such as Self-Organizing Maps (SOM) [28]. Despite these successful studies, the application of AI methods is rather rare in the literature of AM at large. This is because the key to a successful application of AI methods is enormous training data that can be used to estimate the process model, which usually results in extremely high experimental costs. Moreover, due to the proprietary nature of DLD experimental data, data sets are often hard to obtain.

2.4 Summary

The optimization of LBAM process is essential to building LBAM parts with enhanced mechanical properties and improved quality. This requires the combination of the optimization in powder material design/preparation and the corresponding optimal LBAM processing parameters. Thus, efficient process parameter optimization is essential for the establishment of a material process database, realizing a simplified, precise and stable control of AM treatment of versatile powder materials for industrial applications.

In order to achieve enhanced or optimal quality for LBAM parts, it is essential to understand and characterize how LBAM process parameters affect thermal history, solidification, and eventually microstructural/mechanical properties. This remains an open research area due to the large number of process parameters (e.g., laser power, laser velocity, powder feed rate, layer thickness, hatching pitch, scanning pattern, etc.) involved during LBAM. Most of the existing studies seek only optimal process parameters via extensive experimental data or simulation. A major limitation of this approach is that the resulting optimal process parameters may not be useful when experimental conditions (e.g., process or material) change—resulting in new experiments to-be-conducted from scratch. Further research is needed to (i) leverage the information from existing studies and (ii)

systematically characterize the relation between process parameters and part features so that the LBAM process can be optimized in a more efficient manner.

This challenge of process optimization is further compounded by the interactions among LBAM parameters. In reality, it may not be practical to incorporate all process parameters in either experimental or analytical studies. Ignorance of such higher-order interaction effects, taking place during the LBAM process, causes systematic uncertainty in the resulting models and experimental results. Process uncertainty is associated with the initial (latent heat exchange) and evolutionary (dendritic) sollicitation, and conductive, convective, and radiative heat transfer. For instance, the spatial/temporal scale for LBAM is relatively small for conduction heat transfer and thus thermal responses can be difficult to measure and model—especially for the material (which is not detectable). Such uncertainties will not only affect the microstructure but also the mechanical features of the fabricated parts. In addition, there lies considerable uncertainty in melt-pool depth (and other dimensions) due to uncertain heat transfer and fluid/part wetting behavior (contact angles unknown). Further research is needed to systematically incorporate uncertainty when optimizing the LBAM process.

CHAPTER II

ACCELERATED PROCESS OPTIMIZATION FOR LASER-BASED ADDITIVE MANUFACTURING BY LEVERAGING SIMILAR PRIOR STUDIES

2.5 Introduction

Additive Manufacturing (AM) processes can be utilized to generate physical objects directly from a digital model, layer by layer—providing an opportunity to generate complex-shaped, functionally graded, or custom-tailored parts that can be utilized in a variety of engineering applications. New AM technologies have been recently identified as potentially disruptive by manufacturing researchers, practitioners, and public media [29–31]. AM processes are now capable of generating metallic parts such as stainless steel [32–34], Ti-6-Al-4V [35,36], and nickel-based alloys (e.g., Inconel 625 and 718 [37]) and this has allowed AM to transition from solely producing visualization and functional prototypes to producing end-parts for direct use. Many real-world end-parts produced using Laser-Based Additive Manufacturing (LBAM) have recently been reported. These include fuel nozzles produced using Selective Laser Melting (SLM) for GE Aviation’s LEAP engine [38,39] and Airbus’s brackets in its A300/A310 models, which promise to achieve 30–55% weight reduction and 90% raw material usage [40]. Direct end-part production has contributed to 34.7% of the total product and service revenue from AM, a significant increase from only 3.9% in 2003 [39]. Although LBAM has been used for generating parts for real-world industrial application, many challenges remain in achieving its full potential and unlocking the many opportunities that it offers [4].

LBAM relies on the successful layer-to-layer adhesion of melted powder with solid material. A directed energy source, a laser beam being a common example, is utilized to ensure phase-change of the utilized powders. Powders can either be deposited co-axially with the directed energy source—that is, Directed Energy Deposition—or deposited to form a bed first and then selectively melted; that is, Laser Powder Bed Fusion (PBF-L). There are many controllable process parameters that can affect the layer-to-layer adhesion and solidification heat transfer during LBAM—and such parameters have a direct impact on the properties of the produced part [41]. For example, in SLM (a well-known PBF-L process), these parameters include laser power, laser velocity, layer (bed) thickness, hatch distance between successive passes of the laser within the same layer, etc. [42]. Most existing studies that are related to the optimization of LBAM processes can be categorized into two groups: physics-based methods and data-driven methods. Physics-based methods primarily rely on differential equations that govern the underlying thermo-mechanical process [16,43]. Data-driven methods, on the other hand, circumvent the challenge of characterizing underlying thermo-mechanical processes and are based on empirical experimental data and the statistical/intelligent learning methods [17,25,26,44].

Recent efforts in data-driven methods for LBAM center on using a traditional Design of Experiment (DoE) approach, such as two-level fractional factorial design [17,44], full-factorial design [33,45], and response surface methods [46,47]. Other papers have studied the effect of SLM process parameters on the resulting density of SLM parts; however, the process parameters were selected arbitrarily without the use of formal experimental design [32,48,49]. Despite these successful efforts, one important drawback of DOE methods is that most of them do not utilize results from existing studies or the

domain of public knowledge pertaining to the LBAM process. As a result, when the experimental conditions (such as, materials, process type/scale, etc.) change, new sets of experiments are required prior to process optimization, thus leading to higher experimental costs.

The purpose of this study is to present a methodology that accelerates process parameter optimization in LBAM by leveraging prior information from similar, but non-identical, studies, of which there are numerous examples in the literature, due to recent advances in AM technologies. Instead of seeking an unknown global optimal value, the objective of the proposed optimization method is to develop an efficient experimental procedure that seeks to identify the optimal process parameters that result in a targeted value of a mechanical/physical property, which is usually specified by the design or application of the part. A DOE method that utilizes data from prior studies may have first been presented by Vastola [50], who presented a two-step optimization process requiring, first, a large batch of initial experiments and, second, multiple smaller batches of sequential experiments. In this particular method, a large number of experiments may be required; for example, in its initial/first phase, 18 experiments are needed when only two process parameters are taken into account [50]. In contrast, the method presented herein, which is a generalization of the Sequential Minimum Energy Design (SMED) method first proposed by Dasgupta [51], directly utilizes prior data from previous studies as the initial experimental data and incorporates it into sequential optimization experiments. In other words, the process optimization begins with sequential experiments directly without generating initial experiments, resulting in a smaller number of time- and cost-intensive experiments.

One challenge in leveraging prior data is to account for the differences in experimental conditions from which they originated, such as the original equipment manufacturer of the LBAM system, scale of machines, raw material characteristics, etc. Due to these differences, the experimental results for a given material (e.g., density, mechanical strength, geometric accuracy, etc.) between prior and current studies may be different. Figure 2.9 illustrates the concept of our proposed method. In this figure, the horizontal axis represents a given process parameter (x), and the vertical axis represents the objective function (relative density as an example). The $f_2(x)$ curve is the true unknown density function in the current study and we aim to reach its optimum. The $f_1(x)$ and $f_3(x)$ curves represent unknown density functions in two different prior studies. The true objective functions from the current and prior studies do not exactly overlap due to different experimental conditions. Clearly, we cannot fully rely on the reported data in the prior studies (two diamonds on $f_1(x)$ and one triangle on $f_3(x)$) because they do not exactly sit on the $f_2(x)$ curve.

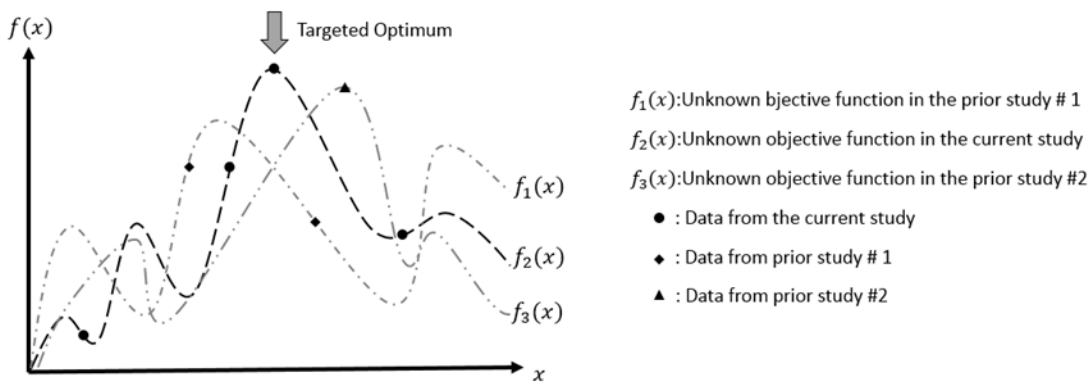


Figure 2.9 Difference between prior and current studies.

The method presented herein characterizes such difference of responses (i.e., experiment results) between the prior and current studies (DRPCS for short) using probability distributions. With this characterization, results from prior studies are used to guide the optimization experiments of the current study and data from the current study are, in turn, used to update the DRPCS distribution. In this presented method, a closed-form expression for updating this distribution to further reduce the computational load and streamline the optimization process is developed. The efficiency and performance of the presented method is examined using a series of simulation studies and a real-world case study using an experimental test based on the SLM process.

The remainder of this article is organized as follows: Sec. 2.6 describes a knowledge-guided optimization process via the efficient utilization of data from related prior studies. In Sec. 2.7, a series of simulation studies and a real-world case study are presented to evaluate the performance of the proposed method. Finally, in Sec. 2.8, concluding remarks and directions for future work related to LBAM process optimization are provided.

2.6 Methodology: accelerated process optimization by leveraging related but non-identical prior studies

We propose an accelerated process optimization methodology for LBAM by leveraging related, but non-identical, prior studies and designing experiments for the current study based on SMED [51,52]. In what follows, we first review the SMED method developed by Dasgupta and then generalize the SMED method to utilize knowledge from prior studies and account for the differences in experimental conditions.

2.6.1 Sequential Minimum Energy Design (SMED)

SMED is a novel DOE method that balances the objectives of optimization and space-filling. For example, assume that we need to determine the parameter values for n potential design points $\mathbf{s}_1, \mathbf{s}_2, \dots, \mathbf{s}_n$ that maximize a response function $y(\mathbf{s})$. Here, the response can be any experimental result of interest, such as, relative density, strength, etc.; and each design point \mathbf{s}_i is a vector that represents a combination of process parameters to be tested via experimentation. To account for the optimization objective (maximizing $y(\mathbf{s})$ for instance), more design points of $\mathbf{s}_1, \mathbf{s}_2, \dots, \mathbf{s}_n$ should be placed in the range of \mathbf{s} that have higher potential of resulting in optimal values of $y(\mathbf{s})$. On the other hand, the range of \mathbf{s} with lower optimization potential should also be tested, i.e., space-filling, to avoid the case where the optimization algorithm is trapped in local optima.

To do this, SMED assigns a positive electrical charge to each design point (i.e. combination of parameters). The charged design points repel each other and occupy positions within the design space so as to minimize the total potential energy. The resulting positions of these electrical charges correspond to the minimum energy design points. The mathematical formulation of the SMED is summarized below: Let $q(\mathbf{s}_i)$ be the charge of the i th design point \mathbf{s}_i . The potential energy between any two design points \mathbf{s}_i and \mathbf{s}_j is equal to $q(\mathbf{s}_i)q(\mathbf{s}_j)/d(\mathbf{s}_i, \mathbf{s}_j)$, where $d(\mathbf{s}_i, \mathbf{s}_j)$ represents the Euclidean distance between \mathbf{s}_i and \mathbf{s}_j . Therefore, the total potential energy for n charged design points, $\mathbf{s}_1, \mathbf{s}_2, \dots, \mathbf{s}_n$ is given by

$$E_n = \sum_{i=1}^{n-1} \sum_{j=i+1}^n q(\mathbf{s}_i)q(\mathbf{s}_j)/d(\mathbf{s}_i, \mathbf{s}_j) \quad (3.1)$$

The optimal parameter values of $\mathbf{s}_1, \mathbf{s}_2, \dots, \mathbf{s}_n$, based on SMED, can be obtained by choosing $\mathbf{s}_1, \mathbf{s}_2, \dots, \mathbf{s}_n$ that minimize the total potential energy E_n .

The charge function $q(\mathbf{s})$ is selected based on the optimization objective. In the previous example, in which the objective is to choose \mathbf{s} to maximize $y(\mathbf{s})$, $q(\mathbf{s})$ should be selected to be a decreasing function of $y(\mathbf{s})$. Hence, any design point \mathbf{s} with a low $y(\mathbf{s})$ value results in a high value of the charge $q(\mathbf{s})$ and thus strongly pushes other design points away. In contrast, a design point with a high $y(\mathbf{s})$ value corresponds to a low charge, which allows for more design points to exist in the neighborhood of \mathbf{s} . Therefore, the number of design points $\mathbf{s}_1, \mathbf{s}_2, \dots, \mathbf{s}_n$ will be higher in the range of \mathbf{s} that tends to maximize the objective function $y(\mathbf{s})$.

SMED allows the addition of $\mathbf{s}_1, \mathbf{s}_2, \dots, \mathbf{s}_n$ in a sequential manner under the constraint of minimizing the total potential energy E , represented by Eq. 3.1. To add a new design point \mathbf{s}_{n+1} , the response at \mathbf{s}_{n+1} (i.e. Y_{n+1}) is predicted using inverse distance weighting (IDW) as follows:

$$\hat{Y}_{n+1} = \frac{\sum_{j=1}^n |\mathbf{s}_{n+1} - \mathbf{s}_j|^{-2} y_j}{\sum_{j=1}^n |\mathbf{s}_{n+1} - \mathbf{s}_j|^{-2}} \quad (3.2)$$

where $|\mathbf{s}_{n+1} - \mathbf{s}_j|^{-2}$ is the coefficient that captures the effect of \mathbf{s}_j on \hat{y}_{n+1} for $j = 1, \dots, n$.

The predicted \hat{Y}_{n+1} value is used to calculate the corresponding charge function $q(\mathbf{s}_{n+1})$ for all possible choices of \mathbf{s}_{n+1} . The new design \mathbf{s}_{n+1} that minimizes total potential energy E will be selected for the next experiment.

Figure 2.10 demonstrates an illustrative example of applying SMED to LBAM process optimization based on some available real experimental data. The vertical axis represents laser power and the horizontal axis represents laser velocity. These are two major factors that significantly affect part density. In this contour plot, the black color corresponds to design points (i.e., combination of process parameters) resulting in part

build with low density, and the light gray color represents design points resulting in high part density. It can be observed that the SMED method tends to assign larger charges to design points that result in lower part density, so that these design points push other design points away to reduce the number of experiment runs in low density areas, and *vice versa*. One limitation of SMED is the fact that it was not developed to account for experimental data from prior studies, thus requiring the generation of all design points within the current study. When the experimental conditions (e.g., original equipment manufacturer of the LBAM system, scale of machine, raw material characteristics, etc.) or target properties (e.g., relative density, tensile strength, elastic modulus, fatigue life, roughness, etc.) change, SMED cannot be used to incorporate the results from prior non-identical studies.

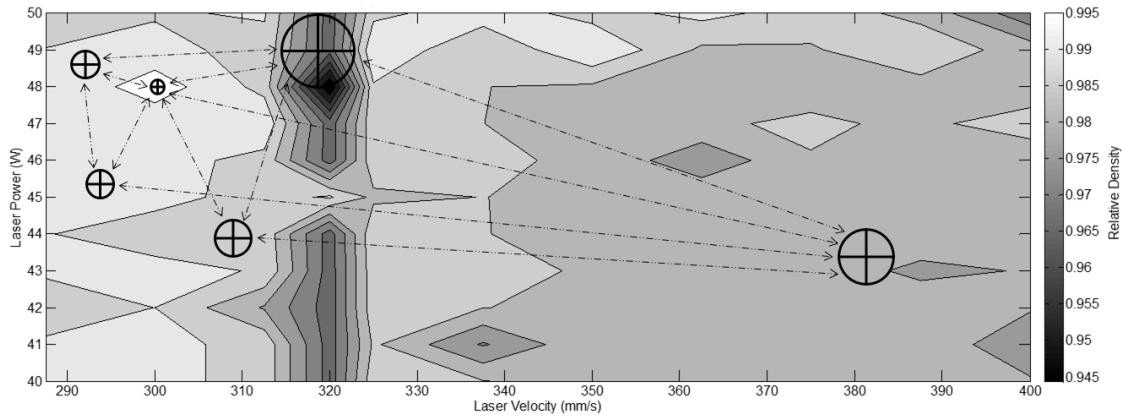


Figure 2.10 Applying SMED to LBAM process optimization.

2.6.2 Accelerated Process Optimization (APO) based on SMED

We extend and generalize the SMED method to accelerate LBAM process optimization by utilizing data from prior studies. Hence, the availability of a few prior studies including some experimental data is a major assumption of the presented method.

However, directly using data from prior studies may cause error in the optimal process parameters of the current study, due to variations in experimental conditions. Our method characterizes the DRPCS using probability distributions. The prior data, with DRPCS, are used to guide the optimization experiments of the current study before any experimental data of the current study are generated. Once data are obtained from the current study, prior data, current data, and DRPCS are used to generate the next design point for the optimization experiment. In particular, responses for the next batch of experiments are predicted using a generalized formula of IDW. Based on the predicted responses, design points that minimize the total potential energy are selected for the next batch of experiments, and the corresponding experimental data are collected. If the experimental results meet a pre-specified criterion, the optimization algorithm is stopped; otherwise, these data are added to the existing database to update the distribution of DRPCS and generate the next batch of experiment designs using the Bayesian method. The Bayesian method allows for updating the parameters of the posterior distribution of DRPCS using empirical data, which eventually converge to their true values even though the initial values of the parameters of prior distributions may not be accurate. In other words, as long as reasonable values of the prior parameters are used, the posterior parameters updated using experimental data will eventually be close to their true values. An overall framework of our proposed accelerated process optimization (APO) method is summarized in Figure 2.11.

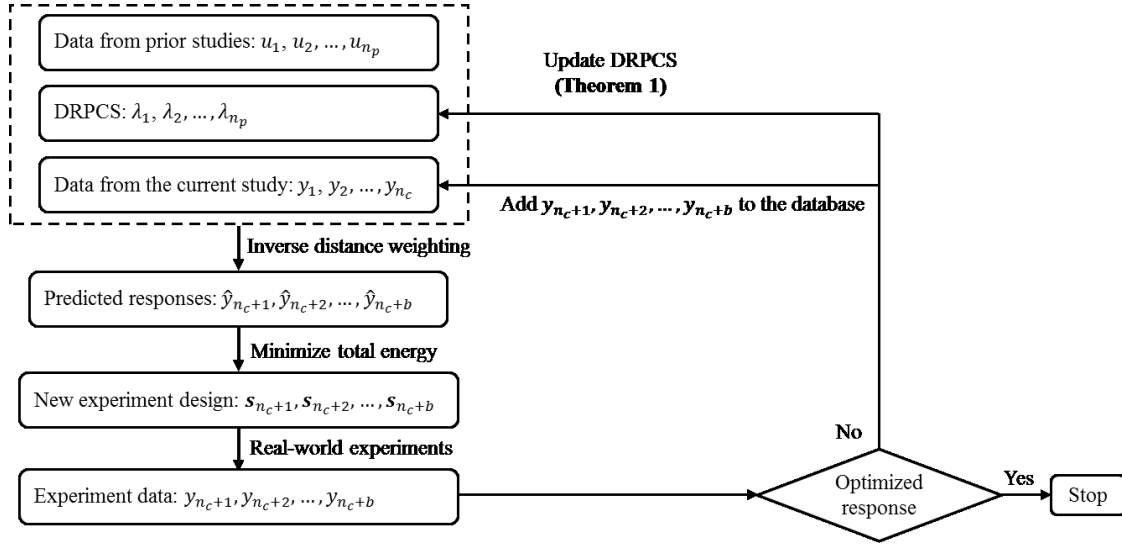


Figure 2.11 Framework of the proposed accelerated process optimization (APO) method.

2.6.2.1 Characterizing DRPCS

Denote data from prior studies by (\mathbf{x}_i, u_i) for $i = 1, 2, \dots, n_p$, where \mathbf{x}_i is the i th design point from prior studies, u_i the corresponding response, and n_p the number of data points from prior studies. Pairs of (\mathbf{x}_i, u_i) 's have been reported in the literature. In the rest of this article, we use lower case letters to represent deterministic known variables; and use upper case letters for random variables. Let random variable Y_i represent the part property corresponding to design point \mathbf{x}_i under the experimental conditions of the current study. Due to the difference in experimental conditions between the current and prior studies, the true value of Y_i is unknown and is thus represented by a random variable. At design point \mathbf{x}_i , the difference between the reported response from prior studies u_i and the actual unknown response from the current study Y_i —that is, DRPCS—is characterized by another random variable λ_i . That is, $\lambda_i = Y_i - u_i$, for $i = 1, 2, \dots, n_p$. The value of DRPCS λ_i is

unknown. In other words, we define λ_i as $\lambda_i = Y_i - u_i$ for the i th design point. u_i is the deterministic experimental data collected in the prior experiments, and Y_i is the unknown response of the current experimental conditions. Without further knowledge, we assume that Y_i follows a normal distribution, which is a common assumption about uncertainty. Hence, $\lambda_i = Y_i - u_i$ also follows a normal distribution. Therefore, we assume that λ_i follows a prior normal distribution $N(\beta_i, \omega_i^2)$, as the normal distribution is the most natural choice in this case. β_i represents the prior mean and ω_i^2 is the prior variance of λ_i , which may be obtained via expert opinions and domain knowledge. We specify the parameters values of (β_i, ω_i^2) based on two cases:

- Case 1: If the domain or expert knowledge about the difference between the current and prior studies is available, the values of β_i and ω_i^2 can be specified using the domain/expert knowledge.
- Case 2: If the domain/expert knowledge is not available, we set $\beta_i = 0$ and $\omega_i^2 = \rho\sigma^2$, where ρ is a tuning parameter and σ is measurement error within the current system.

In our simulation studies and case study, we let $\rho = 0.5$.

Regardless of the values for prior parameters of (β_i, ω_i^2) , the posterior distribution of λ_i updated with the experimental data from the current study will converge to the true distribution by virtue of Bayesian updating. The choice of the values of prior parameters only affects the rate of convergence.

The prior distribution of λ_i is updated using the experimental data obtained from the current study so that the accuracy of the estimated DRPCS can be improved. We denote experimental data to be collected from the current study by (s_j, Y_j) , for $j = 1, 2, \dots$, where

\mathbf{s}_j represents the j th design point in the current study, and Y_j the resulting response. Y_j may be subject to measurement error or there may exist variability in Y_j . Thus, we let $\text{var}(Y_j) = \sigma_j^2$ represent possible error/uncertainty in Y_j . In fact, σ_j represents measurement error of the system or data variation of Y_j 's. For each \mathbf{s}_j , we obtain repeated measurements of Y_j and use the empirical standard deviation of Y_j to estimate σ_j .

2.6.2.2 Predicting the response at new design points

In some real world applications, it may be more efficient to design experiments in the form of batches, so that the total time spent on experiments may be reduced. Our proposed method allows for predicting the responses of design points in batches and generating batch experiments with any integer size b . In what follows, we develop the formula for predicting experiment responses at new design points of the current study \hat{Y}_j 's. We present the formula for two phases: Phase 1 (Initialization), in which the data of the current study has not been generated; and Phase 2 (Iterative Experimentations), in which the data of the current study have been generated in an iterative manner.

Phase 1 (Initialization): In the initialization phase—that is before experimental data are generated from the current study—we only use the prior results, with DRPCS, to optimize the current study. We directly apply Eq. 3.2, the IDW formula by Dasgupta [53] to predict \hat{Y}_j 's, as shown below.

$$\hat{Y}_j = \frac{\sum_{i=1}^{n_p} |\mathbf{s}_j - \mathbf{x}_i|^{-2} (u_i + \lambda_i)}{\sum_{i=1}^{n_p} |\mathbf{s}_j - \mathbf{x}_i|^{-2}}$$

Phase 2 (Iterative Experimentations): When data are generated from the current study, the original IDW formula does not apply because DRPCS are included in the data

of prior studies, whereas, the data of the current study does not include DRPCS terms. We generalize the IDW formula so as to simultaneously account for batch experiments and prior data.

Assume that the available experimental data from the current study are represented by (\mathbf{s}_j, y_j) , for $j = 1, 2, \dots, n_c$, where n_c represents the number of data points available in the current study. Note that n_c is not a fixed constant, instead, the value of n_c increases by batch size b after each batch of experiments in the current study. In what follows, we predict the response values of the next batch of experiments; that is, Y_j 's for $j = n_c + 1, \dots, n_c + b$. If the experimental data from the current study are generated in batches, we need to define the index of its experimental batch. For Y_j , $\left\lfloor \frac{j-1}{b} \right\rfloor$ is the index of the last batch of experiments before Y_j , where $\lfloor \cdot \rfloor$ is the floor function. For example, for experiments with batch size of $b = 4$, there are 2 batches of experiments before Y_9 ; and Y_9 is the 1st experiment in its experimental batch, because $Y_9 = Y_{2 \times 4 + 1}$. With this notation, $n_c = \left\lfloor \frac{j-1}{b} \right\rfloor b$.

The predicted value of Y_j is dependent on response data in previous batches $y_1, y_2, \dots, y_{\left\lfloor \frac{j-1}{b} \right\rfloor b}$ and data from prior studies u_1, \dots, u_{n_p} . We predict Y_j by generalizing the IDW formula represented by Eq. 3.2 to account for its dependency on prior data and batch experiments. The generalized IDW formula of our approach for a new design point \mathbf{s}_j is expressed as follows:

$$\begin{aligned}
\hat{Y}_j &= \frac{\sum_{i=1}^{n_p} |s_j - x_i|^{-2} (u_i + \lambda_i) + \sum_{j'=1}^{\lfloor \frac{j-1}{b} \rfloor b} |s_j - s_{j'}|^{-2} y_{j'}}{\sum_{i=1}^{n_p} |s_j - x_i|^{-2} + \sum_{j'=1}^{\lfloor \frac{j-1}{b} \rfloor b} |s_j - s_{j'}|^{-2}} \quad (3.3) \\
&= \sum_{i=1}^{n_p} w_{j,i} (u_i + \lambda_i) + \sum_{j'=1}^{\lfloor \frac{j-1}{b} \rfloor b} v_{j,j'} y_{j'}
\end{aligned}$$

Where

$$w_{j,i} = \frac{|s_j - x_i|^{-2}}{\sum_{i=1}^{n_p} |s_j - x_i|^{-2} + \sum_{j'=1}^{\lfloor \frac{j-1}{b} \rfloor b} |s_j - s_{j'}|^{-2}}$$

represents the weight coefficient of data from

prior studies, and $v_{j,j'} = \frac{|s_j - s_{j'}|^{-2}}{\sum_{i=1}^{n_p} |s_j - x_i|^{-2} + \sum_{j'=1}^{\lfloor \frac{j-1}{b} \rfloor b} |s_j - s_{j'}|^{-2}}$ the weight coefficient of data

from previous batches of experiments in the current study.

The charge function $q(\mathbf{s})$ is a positive, decreasing function of the objective function $y(\mathbf{s})$. For instance, to maximize the relative density of parts built via LBAM, the objective function $y(\mathbf{s})$ is the relative density of parts. Since the relative density of a part ranges from 0 to 1, a natural choice of charge function is $q(\mathbf{s}) = (1 - y(\mathbf{s}))^\gamma$, where γ is a positive tuning constant. A new SMED point \mathbf{s}_j minimizes the total potential energy E , which consists of three components: the potential energy of the design points from prior studies, the potential energy of the design points from the current study, and potential energy between these two groups. The total potential energy function including Y_j is expressed as follows:

$$E_j = \sum_{i=1}^{n_p-1} \sum_{i'=i+1}^{n_p} \frac{q(x_i)q(x_{i'})}{d(x_i, x_{i'})} + \sum_{j=1}^{j-1} \sum_{j'=j+1}^j \frac{q(s_j)q(s_{j'})}{d(s_j, s_{j'})} + \sum_{i=1}^{n_p} \sum_{j=1}^j \frac{q(x_i)q(s_j)}{d(x_i, s_j)} \quad (3.4)$$

The new design point in the current study can be obtained by solving $\mathbf{s}_j = \text{argmin } E_j$. Finding SMED for the next batch of experiments, namely Y'_j 's for $j = n_c + 1, \dots, n_c + b$, is a computationally difficult problem. We can adapt the optimal design algorithms used in the literature such as simulated annealing [54] and stochastic evolutionary algorithm [55] for our purpose. Different from these methods, we implemented the exchange algorithm to generate Y'_j 's for $j = n_c + 1, \dots, n_c + b$ based on Eq. 3.4. The main idea of the exchange algorithm is that an initial proposed batch of potential design points is updated by exchanging one of its design points with a potential one, given that the new design point decreases the total energy. The exchange algorithm has been successfully implemented to generate the batches of SMED [50,56,57]. The details of the exchange algorithm can be found in the textbook by Fedorov and Hackl [58]. We do not include the detailed algorithm and the corresponding properties in this article due to page limitations.

2.6.2.3 Updating DRPCS

Theorem 1 presents the analytical form of the posterior distribution of DRPCS, λ_i , updated using data from the current study (\mathbf{s}_j, Y_j) , for $j = 1, \dots, n_c$, which are generated in batches of size b . *Theorem 1* shows that the posterior distribution of DRPCS still follows a multivariate normal distribution with specific parameters.

Theorem 1: Assume that DRPCS terms, λ_i are independent and identically distributed random variables following the prior distribution $N(\beta_i, \omega_i^2)$ for $i = 1, 2, \dots, n_p$. The posterior distribution of $\boldsymbol{\lambda}$, with $\boldsymbol{\lambda} = (\lambda_1, \dots, \lambda_{n_p})'$, updated using experimental data from the current study $\{(\mathbf{s}_j, y_j): j = 1, 2, \dots, n_c\}$ still follows a multivariate normal distribution with mean vector $\boldsymbol{\mu}_\lambda = \boldsymbol{\Lambda}^{-1}\boldsymbol{\eta}$ and covariance matrix $\boldsymbol{\Sigma}_\lambda = \boldsymbol{\Lambda}^{-1}$, where η_i is the i th element of vector $\boldsymbol{\eta}$ and $\Lambda_{i,k}$ the (i,k) th element of matrix $\boldsymbol{\Lambda}$. $\Lambda_{i,k}$ and η_i can be expressed as follows:

$$\eta_i = \sum_{j=1}^{n_c} \frac{w_{j,i} \delta_j}{\sigma_j^2} + \frac{\beta_i}{\omega_i^2}$$

$$\Lambda_{i,k} = \begin{cases} \sum_{j=1}^{n_c} \frac{w_{j,i}^2}{\sigma_j^2} + \frac{1}{\omega_i^2} & \text{and } i = k \\ \sum_{j=1}^{n_c} \frac{w_{j,i} w_{j,k}}{\sigma_j^2}, & \text{and } i \neq k \end{cases}$$

where

$$w_{j,i} = \frac{|\mathbf{s}_j - \mathbf{x}_i|^{-2}}{\sum_{i=1}^{n_p} |\mathbf{s}_j - \mathbf{x}_i|^{-2} + \sum_{j'=1}^{\lfloor \frac{j-1}{b} \rfloor b} |\mathbf{s}_j - \mathbf{s}_{j'}|^{-2}}$$

$$v_{j,j'} = \frac{|\mathbf{s}_j - \mathbf{s}_{j'}|^{-2}}{\sum_{i=1}^{n_p} |\mathbf{s}_j - \mathbf{x}_i|^{-2} + \sum_{j'=1}^{\lfloor \frac{j-1}{b} \rfloor b} |\mathbf{s}_j - \mathbf{s}_{j'}|^{-2}}$$

$$\delta_j = y_j - \sum_{i=1}^{n_p} w_{j,i} u_i - \sum_{j'=1}^{\lfloor \frac{j-1}{b} \rfloor b} v_{j,j'} y_{j'}$$

Proof. Let $g(\boldsymbol{\lambda}|\mathbf{y})$ represent the posterior function of $\boldsymbol{\lambda}$ given data from the current experiment \mathbf{y} , where $\mathbf{y} = (y_1, \dots, y_{n_c})'$. We estimate the expression of $g(\boldsymbol{\lambda}|\mathbf{y})$ using the Bayesian formula. That is,

$$g(\boldsymbol{\lambda}|\mathbf{y}) \propto \pi(\boldsymbol{\lambda})L(\boldsymbol{\lambda}|\mathbf{y})$$

where $\pi(\boldsymbol{\lambda})$ represents the *prior distribution* of $\boldsymbol{\lambda}$ and $L(\boldsymbol{\lambda}|\mathbf{y})$ the *likelihood function* of $\boldsymbol{\lambda}$ given \mathbf{y} . Recall that λ_i follows a normal prior distribution $N(\beta_i, \omega_i^2)$. Since it is assumed all prior data are from different independent sources, the corresponding DRPCS terms are also assumed to be independent. Thus, the expression of $\pi(\boldsymbol{\lambda})$ can be represented as the product of n_p probability density functions as follows:

$$\pi(\boldsymbol{\lambda}) = \prod_{i=1}^{n_p} (2\pi\omega_i^2)^{-\frac{1}{2}} \exp\left\{\frac{-1}{2\omega_i^2} (\lambda_i - \beta_i)^2\right\}$$

By expanding the prior distribution of λ_i we can re-write $\pi(\boldsymbol{\lambda})$ according to the terms involving λ_i 's as follows (see Appendix A for a detailed calculation):

$$\pi(\boldsymbol{\lambda}) \propto \exp\left\{\frac{-1}{2} \sum_{i=1}^{n_p} \frac{\lambda_i^2}{\omega_i^2} + \sum_{i=1}^{n_p} \frac{\lambda_i \beta_i}{\omega_i^2}\right\}$$

In what follows, we determine the closed-form expression of likelihood function $L(\boldsymbol{\lambda}|\mathbf{y})$ and the probability distribution determined by $g(\boldsymbol{\lambda}|\mathbf{y})$.

Developing likelihood function $L(\boldsymbol{\lambda}|\mathbf{y})$:

The likelihood function $L(\boldsymbol{\lambda}|\mathbf{y})$ has the same expression as the probability density function (pdf) of \mathbf{Y} given parameter $\boldsymbol{\lambda}$ and data from prior studies; that is, $f(\mathbf{Y}|\boldsymbol{\lambda}, \mathbf{u})$. As the design points of the current study are generated in a sequential manner, the resulting responses Y_1, Y_2, \dots, Y_{n_c} are dependent. In this regard, the functional form of $f(\mathbf{Y}|\boldsymbol{\lambda}, \mathbf{u})$ cannot be expressed directly. Based on the conditional probability principles, the functional form of $f(\mathbf{Y}|\boldsymbol{\lambda}, \mathbf{u})$ can be calculated by multiplying the conditional distribution of Y_1, Y_2, \dots, Y_{n_c} . Hence, we can represent $f(\mathbf{Y}|\boldsymbol{\lambda}, \mathbf{u})$ as follows:

$$f(\mathbf{Y}|\boldsymbol{\lambda}, \mathbf{u}) = \prod_{j=1}^{n_c} f_j \left(Y_j \middle| Y_1, Y_2, \dots, Y_{\lfloor \frac{j-1}{b} \rfloor b}, \mathbf{u}, \boldsymbol{\lambda} \right)$$

The conditional distribution of Y_j , for $j = 1, \dots, n_c$, follows a normal distribution

$$Y_j \middle| \left(Y_1, Y_2, \dots, Y_{\lfloor \frac{j-1}{b} \rfloor b}, \mathbf{u}, \boldsymbol{\lambda} \right) \sim N(\mu_j, \sigma_j^2)$$

where

$$\mu_j = \sum_{i=1}^{n_p} w_{j,i} (u_i + \lambda_i) + \sum_{j'=1}^{\lfloor \frac{j-1}{b} \rfloor b} v_{j,j'} y_{j'}.$$

After combining terms that involve λ_i 's, we express the likelihood function $L(\boldsymbol{\lambda}|\mathbf{y})$ as follows (see Appendix B for a detailed calculation):

$$L(\boldsymbol{\lambda}|\mathbf{y}) \propto \exp \left\{ \frac{-1}{2} \left(\sum_{i=1}^{n_p} \lambda_i^2 \sum_{j=1}^{n_c} \frac{w_{j,i}^2}{\sigma_j^2} + 2 \sum_{i \neq k} \lambda_i \lambda_k \sum_{j=1}^{n_c} \frac{w_{j,i} w_{j,k}}{\sigma_j^2} \right) + \sum_{i=1}^{n_p} \lambda_i \sum_{j=1}^{n_c} \frac{w_{j,i} \delta_j}{\sigma_j^2} - \frac{1}{2} \sum_{j=1}^{n_c} \left(\frac{\delta_j}{\sigma_j} \right)^2 \right\}$$

where

$$\delta_j = y_j - \sum_{i=1}^{n_p} w_{j,i} ; \text{ and } u_i = \sum_{j'=1}^{\lfloor \frac{j-1}{b} \rfloor b} v_{j,j'} y_{j'}.$$

Developing the posterior probability density function $g(\lambda|\mathbf{y})$:

Now by multiplying the expanded form of $L(\lambda|\mathbf{y})$ and $\pi(\lambda)$, the posterior distribution of λ_i using Bayesian formula $g(\lambda|\mathbf{y}) \propto \pi(\lambda)L(\lambda|\mathbf{y})$ is expressed as follows (see Appendix C for a detailed calculation):

$$g(\lambda|\mathbf{y}) \propto \exp \left\{ \frac{-1}{2} \left(\sum_{i=1}^{n_p} \lambda_i^2 \left(\sum_{j=1}^{n_c} \frac{w_{j,i}^2}{\sigma_j^2} + \frac{1}{\omega_i^2} \right) + 2 \sum_{i \neq k} \lambda_i \lambda_k \sum_{j=1}^{n_c} \frac{w_{j,i} w_{j,k}}{\sigma_j^2} \right) \right. \\ \left. + \sum_{i=1}^{n_p} \lambda_i \left(\sum_{j=1}^{n_c} \frac{w_{j,i} \delta_j}{\sigma_j^2} + \frac{\beta_i}{\omega_i^2} \right) \right\}$$

The resulting posterior distribution $g(\lambda|\mathbf{y})$ involves the 1st and 2nd order terms of λ_i 's, and thus represents the pdf of a multivariate normal distribution. However, the posterior mean vector and covariance matrix of λ are not in explicit forms.

We utilize the canonical representation of a multivariate normal distribution to determine the posterior mean vector and covariance matrix of λ . For a multivariate normal random variable \mathbf{z} with mean vector $\boldsymbol{\mu}$ and covariance matrix $\boldsymbol{\Sigma}$, the following two representations of multivariate pdf's are equivalent:

$$h_1(\mathbf{z}|\boldsymbol{\mu}, \boldsymbol{\Sigma}) = \frac{1}{(2\pi)^{\frac{n}{2}} |\boldsymbol{\Sigma}|^{\frac{1}{2}}} \exp \left\{ -\frac{1}{2} (\mathbf{z} - \boldsymbol{\mu})^T \boldsymbol{\Sigma}^{-1} (\mathbf{z} - \boldsymbol{\mu}) \right\}$$

and

$$h_2(\mathbf{z}|\boldsymbol{\eta}, \boldsymbol{\Lambda}) \propto \exp \left\{ a + \boldsymbol{\eta}^T \mathbf{z} - \frac{1}{2} \mathbf{z}^T \boldsymbol{\Lambda} \mathbf{z} \right\}.$$

These two representations of pdf's are equivalent via the re-parameterizations:

$$\mathbf{\Lambda} = \mathbf{\Sigma}^{-1}, \mathbf{\eta} = \mathbf{\Sigma}^{-1}\mathbf{\mu}; \text{ and } a = -\frac{1}{2}(n \log(2\pi) - \log|\mathbf{\Lambda}| + \mathbf{\eta}^T \mathbf{\Lambda} \mathbf{\eta}).$$

Applying the canonical representation to $g(\boldsymbol{\lambda}|\mathbf{y})$, we obtain the posterior mean vector and covariance matrix of $\boldsymbol{\lambda}$ as follows: $\mathbf{\Sigma}_{\boldsymbol{\lambda}} = \mathbf{\Lambda}^{-1}$ and $\mathbf{\mu} = \mathbf{\Lambda}^{-1}\mathbf{\eta}$, where (see Appendix D for a detailed calculation)

$$\Lambda_{i,k} = \begin{cases} \sum_{j=1}^{n_c} \frac{w_{j,i}^2}{\sigma_j^2} + \frac{1}{\omega_i^2} & \text{and } i = k \\ \sum_{j=1}^{n_c} \frac{w_{j,i}w_{j,k}}{\sigma_j^2}, & \text{and } i \neq k \end{cases}$$

$$\eta_i = \sum_{j=1}^{n_c} \frac{w_{j,i}\delta_j}{\sigma_j^2} + \frac{\beta_i}{\omega_i^2}$$

It is worth noting that the posterior distributions of λ_i 's are *closed-form* expressions, which requires minimal computational resources and can be embedded in LBAM systems for process optimization. Also, $\mathbf{\Lambda}$ is a real symmetric matrix and can always be inverted. This guarantees the existence of the posterior covariance matrix $\mathbf{\Sigma}_{\boldsymbol{\lambda}}$.

Although we assume independence among the prior distribution of λ , our model can capture the dependence among prior data via specifying the values of the prior mean of λ_i , namely β_i . The prior data from the same or similar experimental conditions tend to have similar values for β_i . For example, if we have 3 prior data from the same experimental condition, and we know that this experimental condition tends to generate parts with higher density than the current experimental condition, we may specify appropriate positive values of prior means; for example, $\beta_1 = 0.002, \beta_2 = 0.003, \beta_3 = 0.0025$. If we have 2 additional prior data from another experimental condition, which results in lower density,

we can set negative values of the corresponding prior means; for example, $\beta_4 = -0.002, \beta_5 = -0.003$. Moreover, if λ_i 's are dependent, this dependency will be captured in their posterior distribution. We showed, in *Theorem 1*, that posterior distribution of λ_i 's follows a multivariate normal distribution, which allows for dependence between the λ_i values.

2.7 Numerical studies

We examine the efficiency and robustness of the proposed process optimization method via a series of simulation studies, which simulate the relative density of parts based on an empirical relative density model developed by Spierings et al.[59]; and a real-world case study, which aimed at maximizing the part density of SLM 17-4 PH stainless steel (SS). We measure the efficiency of the optimization method using the number of experiment runs needed to reach a targeted part relative density. In the simulation studies, we tested how different characteristics of DRPCS affected the efficiency of our proposed method. The results were compared to two existing DOE methods: traditional full factorial DOE and SMED.

2.7.1 Simulation studies

We performed a series of simulation studies so that we could generate prior data with various types of DRPCS and examine how they affect the efficiency of our proposed optimization method. We focused on the effect of four process parameters (laser power, laser velocity, hatch distance, and powder layer thickness) on the relative density of parts built via SLM, simulated using the empirical relative density function developed in Ref. [59] as shown in Eq. 3.5 and Figure 2.12 below:

$$y = 0.92 + 12.2a^{-1} - 514a^{-2} + 4318a^{-3} \quad (3.5)$$

in which a is the energy density with $a = \frac{\text{Laser Power}}{\text{Laser Velocity} \times \text{Hatch Distance} \times \text{Layer Thickness}}$.

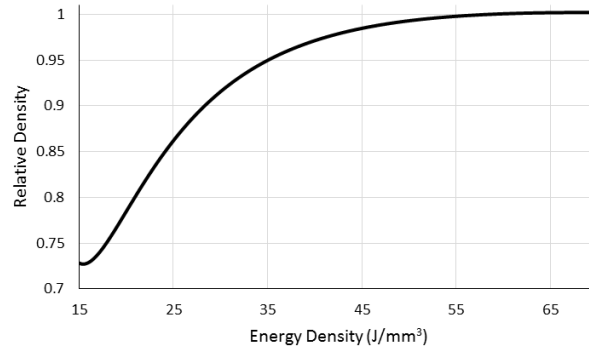


Figure 2.12 Empirical relation between relative part density and energy density [59].

This empirical model is resulted from a full factorial DOE for SLM built stainless steel 17-4PH/AISI-630 material. The type of SLM machine used in the experiments was a Concept Laser M2. A chess-board scanning structure was applied to fabricate tensile samples. Two levels were assumed for five process parameters as provided in Table 2.10. In addition, hatch distance was fixed at 0.0975mm.

Table 2.10 DOE factors and levels applied for empirical density empirical function, Eq. 3.5.

Factors	Level 1	Level 2
Build orientation	Vertical	Horizontal
Layer thickness (μm)	30	50
Laser velocity (mm/s)	800	1300
Laser power (W)	105	190

Equation 5 was used to generate the y_j values, the part density given the process parameters of the current study. To simulate u_1, \dots, u_{n_p} , we artificially added DRPCS to

y_j values computed using Eq. 3.5 that represent the differences in density caused by different experimental conditions in prior and current studies. Five different groups of prior data representing different types of DRPCS were generated as shown in Table 2.11, and the corresponding performance of our approach was examined and is reported in this section. For example, the first row of the Table 2.11 represents one prior data with a reported relative density of 50%; that is, $u_1 = 0.5$. We set the corresponding DRPCS $= -0.33$, meaning that the true value of $\lambda_1 = -0.33$. The true value of λ_i was only used for the purpose of data simulation. We did not use this information in the process of optimization. In the first four scenarios, we investigated how different characteristics (e.g. sign and magnitude) of the DRPCS affect the number of experiments conducted. Two prior data points were used for the purpose of demonstration. In the 5th scenario, we increased the number of prior data points from 2 to 5 and examined the effect of n_p .

Table 2.11 Different types of DRPCS for SLM SS 17-4 PH.

Data number	Laser power (W)	Laser velocity (mm/s)	Hatch distance (mm)	Layer thickness (mm)	Relative density from prior studies u_i	DRPCS
Scenario 1: negative DRPCS						
1	50	1850	0.05	0.04	0.5	- 0.33
2	120	1756	0.1	0.032	0.6	- 0.25
Scenario 2: negative DRPCS (small magnitude)						
1	50	1850	0.05	0.04	0.63	- 0.16
2	120	1756	0.1	0.032	0.70	- 0.13
Scenario 3: negative and positive DRPCS						
1	50	1850	0.05	0.04	0.50	- 0.33
2	120	1756	0.1	0.032	0.90	0.11
Scenario 4: positive DRPCS						
1	50	1850	0.05	0.04	0.92	0.22
2	120	1756	0.1	0.032	0.98	0.22
Scenario 5: more prior data points						
1	50	1850	0.05	0.04	0.57	-0.24
2	120	1756	0.1	0.032	0.65	-0.19
3	70	1500	0.07	0.034	0.6	-0.22
4	100	1200	0.08	0.036	0.74	-0.18
5	60	604	0.1	0.038	0.7	-0.19

We set the values of β_i to zero, as there was no prior knowledge available. We also let $\omega_i^2 = 3.5 \times 10^{-2}$, as λ_i ranged from zero to one. We estimated σ_j^2 using generated repeated measurements of Y_j and obtained that $\sigma_j^2 = 4 \times 10^{-3}$. For all scenarios, we conducted simulation experiments with a batch size $b = 2$. We considered $\gamma = 3$ for all simulation and case studies as the tuned parameter in the charge function $q(\mathbf{s}) = (1 - y(\mathbf{s}))^\gamma$, as it is recommended by Dasgupta [51]. (Note that a set of simulated experiments are shown in Appendix F to illustrate the superiority the optimization performance of $q(\mathbf{s}) = (1 - y(\mathbf{s}))^\gamma$ for $\gamma = 3$ in our method.)

2.7.1.2 Comparing our approach with full factorial DOE

We measure the number of experiments needed to reach a targeted relative density of 99.65%, which represents a reasonable target. This target value can be replaced by any other criterion. We first compare our approach with the full factorial design, which has been used by other researchers to optimize the SLM process [17,33,45]. Note that experiments using the full factorial design approach were performed at the same time, as opposed to a sequential manner. We vary the number of levels for each factor so that the optimal relative density could be achieved. The possible combinations of process parameters and levels that result in the targeted density are summarized in Table 2.12: 10 levels for laser power, 3 levels for laser velocity, 3 levels for hatch distance, and 2 levels for layer thickness. Without considering replicated measurements, which leads to higher number of experiments, the minimum number of experiments needed to achieve the target density using the full factorial design approach was $10 \times 3 \times 3 \times 2 = 180$ experiments. In contrast, the maximum number of experiments needed to achieve the targeted density using our approach was 21.

Table 2.12 Process optimization using full factorial DOE.

Process Parameter	Min	Max	Levels
Laser power (W)	40	50	10
Laser velocity (mm/s)	400	2000	3
Hatch distance (mm)	0.05	0.15	3
Layer thickness (mm)	0.03	0.01	2

2.7.1.3 Comparing our approach with sequential minimum energy design (SMED)

We compare our approach with SMED approach proposed by Dasgupta [51]. Figure 2.13 compares the number of experiments under various scenarios needed to achieve the targeted relative density by applying both SEMD and our method. Figure 2.14 illustrates percentage improvement in terms of the number of experiments by applying our method rather than SMED. Detailed experimental results are summarized in Appendix E.

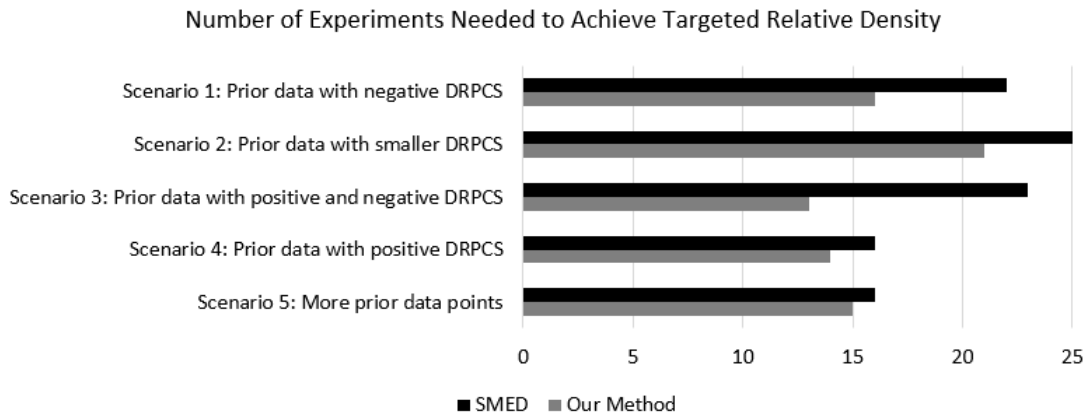


Figure 2.13 Comparison between SMED and our method's performance.

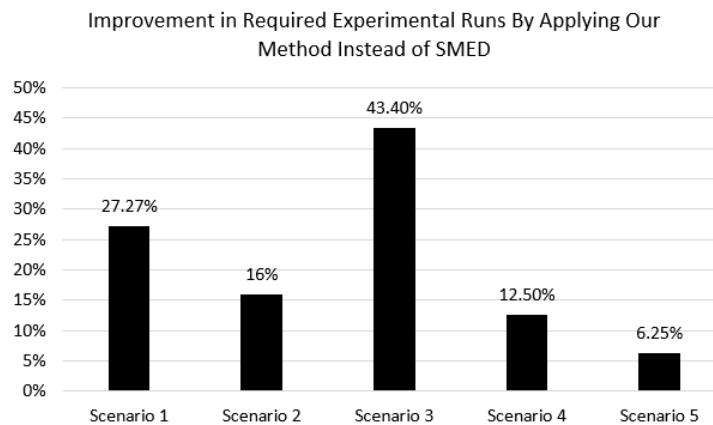


Figure 2.14 Resulted improvement by applying our method instead of SMED.

Since the SMED method does not account for the error in the prior data, we applied SMED to prior data without characterizing and updating DRPCS. We also report the computational time needed for each method and each scenario in Table 2.13. All computations were coded in MATLAB 2013 on a desktop with Intel Core i7 3.60 GHz processor and 16.0 GB RAM. We made the following observations:

- The simulation studies show consistent improvement in the number of experiment runs of our proposed method, compared with SMED, this is due to our method being able to characterize the DRPCS distribution and update DRPCS using data from the current study. The updated distribution of DRPCS facilitates the generation of new optimization experiments.
- When the magnitude of DRPCS increases, the improvement of our method is greater; for example, 16 to 27% (see scenarios 1 and 2 in Figure 2.14). This is because the strength of our method is characterization of DRPCS. On the other hand, when the magnitude of DRPCS is relatively insignificant, our method and SMED have a relatively similar performance.
- The largest improvement in experiment runs (43%) is observed when there are positive and negative DRPCS (See scenario 3 in Figure 2.14). The DRPCS with different signs may occur when the prior data come from different sources, which might contradict each other. The simulation results of scenario 3 indicate that our method can be implemented to handle contradicting prior studies, as even if contradicting prior results are included in our database, our method is capable of updating the DRPCS using data

from the current study and eventually generating an accurate DOE for the purpose of optimization.

- For all five scenarios, our method requires less computational time compared with SMED, as our method can obtain the optimal parameters with fewer experiments.

Table 2.13 Computational time needed to obtain optimal process parameters.

Scenario	Computational time (Second)	
	SMED	Our method
Negative DRPCS	44	16
Negative DRPCS with small magnitude	51	27
Negative and positive DRPCS	38	6
Positive DRPCS	11	7
More prior data points	13	11

2.7.1.4 Comparing various charge functions

We performed a sequence of numerical studies to examine the performance of our methodology with other possible choices of charge functions. Dasgupta [51] recommended the use of a charge function with the form $q(x_i) = (1 - \alpha p(x_i))^\gamma$, where α and γ are positive tuning constants with $\alpha \leq [\max_x p(x)]^{-1}$. We used the recommended functional form of the charge function and compared the performance of our method and SMED for different values of the tuning parameters. Note that, in our model, $p(x)$ represents the relative part density and thus $\alpha \leq [\max_x p(x)]^{-1} = 1$. We varied the values of the tuning parameter γ . To systematically compare the performance of our method with different $q(s)$ functions, we tested the performance of our methodology with different values of γ ($= 1, 3, 5$) and for multiple scenarios of DRPCS (negative, positive, and both). The results are summarized in Table 2.1 (detailed numerical results can be found in Appendix F).

Table 2.1 Number of experiment runs needed to achieve the target density with various choices of change functions and various scenarios of DRPCS.

Scenario of DRPCS	Method	Choices of charge function		
		$\gamma = 1$	$\gamma = 3$	$\gamma = 5$
Negative DRPCS	SMED	12	22	38
	Our method	12	16	14
Negative and positive DRPCS	SMED	11	23	26
	Our method	11	13	26
Positive DRPCS	SMED	12	16	17
	Our method	11	14	14

We observe that, for most cases ($\gamma = 3$ or 5), our methodology requires fewer experiments to obtain the process parameters of the targeted density value, compared with SMED. When $\gamma = 1$, the performance of our method and SMED is similar, although our method has slightly better performance for the scenario of positive DRPCS. This is partially due to the correlation between the results of prior studies and current study being weak at low γ values. In this case, the incorporation of DRPCS does not have a significant impact on the predicted value of the response in the current study. Thus, our method and SMED have a similar performance. An extreme example is that $q(x) = 1$ if $\gamma = 0$. In this case, experiment results are not correlated with each other, and prior results cannot be used to guide future experiments.

2.7.2 Case study

We verify the performance of our method in a real-world case study that aims at maximizing the relative density of parts (test coupons in this case) built in a ProX 100 SLM System using PH 17-4 SS powder (see Figure 2.15). The fabrication of steel alloys has been frequently studied in the literature on metal-based AM, including austenitic 316 L SS [32,60–62], H13 tool steel [63–65], and maraging steel [34,66]. In this case study, we focus

on precipitation hardening martensitic steel (17-4 PH SS) which is widely used in industrial applications that require a combination of high strength and a moderate level of corrosion resistance [67]. This alloy is more common than any other type of precipitation hardening SS, and has been frequently used in parts such as oil field valve parts, aircraft fittings, nuclear reactor components, paper mill equipment, missile fittings and jet engine parts [68]. Some researchers have studied the additive manufacture of 17-4 PH SS using SLM; focusing on its manufacturability and analyzing the resulting microstructural/mechanical properties of the manufactured samples [69–72].

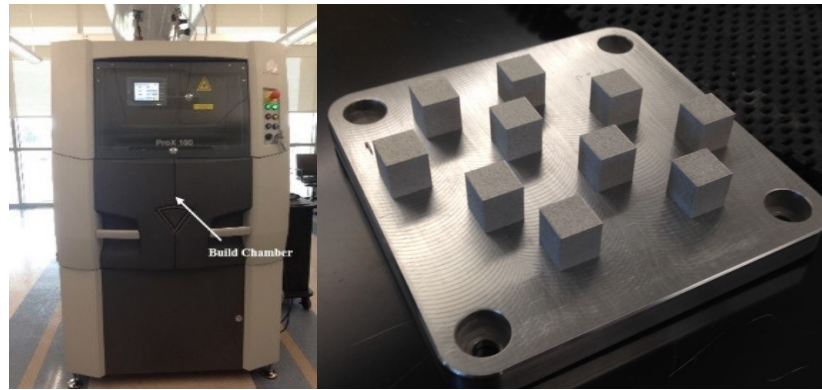


Figure 2.15 ProX 100 SLM System (left) and test coupons (right).

We found three prior studies that reported on the density of 17-4 SS parts fabricated via SLM [49,59,72]. Despite using the same type of SLM process, the capacities of these machines are different. For instance, the EOS M270 system used in the study of Gue et al. [73] can output a maximum laser power of 200W. The maximum relative part density is achieved when laser power is set at the level of 195W, which exceeds the maximum laser power capacity of our SLM system and that of Kumar and Kruth [72]. Thus, the optimized process parameters obtained from the study of Gue et al. [73] cannot be applied directly to

manufacturing fully dense parts in our study. Other than the maximum laser power, there exist differences in other experimental conditions, such as laser profile and powder morphology. One of the key differences is the powder feed mechanism. The SLM system used in our study uses a roller that first feeds the powder in the feeding piston, and then spreads the layer using counter-rotation, whereas the other systems used in the prior studies use a blade for powder feeding. A detailed summary of the experimental conditions of prior studies and our study are presented in Table 2.14.

Table 2.14 Experimental conditions in prior and current studies for SLM of 17-4 PH SS.

	Prior study 1 [73]	Prior study 2 [59]	Prior study 3 [74]	Our study
System	EOS M270 (EOS GmbH)	M2 Laser CUSING (Concept Laser)	In-house developed SLM machine	ProX 100™
Maximum laser power	200W	200W	150W	50W
Laser spot diameter	100-500μm	50-500μm	N/A	70μm
Raw powder	GP1 by EOS (Proprietary)	AISI-630 Stainless steel (Standard)	GP1 by EOS (Proprietary)	PS4542A by 3D Systems (Proprietary)
Powder particle size distribution	37.13μm mean diameter	D10 = 16.4μm D50 = 26.8μm D90 = 42.7μm	37.13μm mean diameter	10 < D50 <13.5μm D80 < 22μm

Due to these differences in experimental conditions and the sensitivity of part density to process parameters, the optimal process parameters in these prior studies cannot be directly applied in our study. We applied the proposed knowledge-guided process optimization method and used data from prior studies (see Table 2.15) as prior data in our study.

Table 2.15 Experimental data from prior studies [49,59,72]

Laser power(W)	Scan velocity(mm/s)	Hatch spacing(mm)	Layer thickness(mm)	Relative density(%)
Prior study 1 [73]				
195	1200	0.1	0.04	98.66
195	1100	0.1	0.04	99.75
195	1000	0.1	0.04	99.75
195	900	0.1	0.04	99.58
195	800	0.1	0.04	100.00
195	700	0.1	0.04	100.00
195	600	0.1	0.04	99.83
195	800	0.1	0.04	100.00
170	679	0.1	0.04	100.00
145	594	0.1	0.04	100.00
120	492	0.1	0.04	99.63
95	389	0.1	0.04	95.85
70	287	0.1	0.04	94.60
Prior study 2 [59]				
105	800	0.0975	0.03	98.44
190	800	0.0975	0.03	100.00
105	1300	0.0975	0.03	89.28
190	1300	0.0975	0.03	99.29
105	800	0.0975	0.05	88.53
190	800	0.0975	0.05	99.12
105	1300	0.0975	0.05	73.33
190	1300	0.0975	0.05	91.53
Prior study 3 [72]				
95	350	0.14	0.03	98.00

The experiments were designed by batch size two; that is, $b = 2$. For each design point of our study, we printed 4 samples to account for variability in the data. The experimental data of our study are shown in Table 2.2. We stopped the optimization process at the 5th experiment at a laser power of 49W, laser velocity of 350mm/s, hatch spacing of 0.05mm, and layer thickness of 0.03mm, which resulted in an average part density of 99.20%. We believe that this level of relative density is sufficiently high for many engineering applications. Moreover, this combination of process parameters is

exactly the recommended process parameters by the manufacturer, which was not used in our optimization procedure. In other words, our proposed optimization method can achieve the manufactured recommended setup within 5 experiments.

Table 2.2 Density optimization data of the case study.

	Laser power(W)	Laser velocity(mm/s)	Hatch spacing(mm)	Layer thickness(mm)	Average relative density (%)
1	50	300	0.07	0.03	98.41
2	40	200	0.07	0.03	96.53
3	50	200	0.14	0.03	92.27
4	50	440	0.07	0.03	97.14
5	49	350	0.05	0.03	99.20

2.8 Summary and conclusions

This article presented a novel approach for systematically optimizing controllable process parameters in LBAM processes via a novel sequential DOE approach. The proposed method was developed on the premise that studies related to various metal-based LBAM processes share similar transformations from raw material to final part (that is, powder melting) and thus the microstructural and mechanical properties of LBAM parts may be correlated, despite differences in experimental conditions, material properties, system capacity, etc. We utilized data from prior, related studies to accelerate and characterize the DRPCS using statistical distributions. We developed a closed-form expression to update the distribution of DRPCS using data from the current study. As a result, prior data can be directly used as initial experiments, and this reduces the total number of experiments needed for optimization. To evaluate the performance of our approach, we conducted a series of validation experiments that used an empirical relative

density model with four process parameters (laser power, laser velocity, hatch spacing, and layer thickness). We focused on the number of experiments needed to achieve a target relative density level. To test the performance of our method, we studied the effects of two key factors related to prior data: the signs and magnitudes of DRPCS.

The results demonstrate significant promise for accelerating the optimization of LBAM processes. Comparisons with two benchmark models; full-factorial design, which does not account for the optimization objective, and SMED, which does not utilize prior data, illustrate the importance of leveraging prior data. We further verified our method using a real-world case study that aimed at optimizing the relative part density of PH 17-4 SS parts using a SLM system. Optimized process parameters from prior studies could not be applied directly due to difference scales of LBAM systems. We utilized these studies as prior data and applied our optimization method. The optimal process parameters were achieved within five experimental runs.

The proposed method is not limited to solely optimizing part density in parts built via SLM systems. In fact, the proposed methodology provides a formal framework for better understanding the similarities among AM machines and the correlation of microstructural/mechanical properties, not through complex physics-based models that are often computationally cumbersome but through a more practical approach that relies on building a genome (database) of related experiment studies and modeling correlations among the experimental data. The proposed method is established based on two major assumptions: first, the availability of prior experimental data from similar systems and, second, the normally distributed DRPCS together with the prior data to guide the process optimization. Assuming a normal distribution for DRPCS terms may be seen as a limitation

of the proposed method; however, it could be an appropriate and natural choice with which to start the study. Future work is needed to characterize the distribution of DRPCS. Also, there is a need to optimize multiple mechanical properties, which may be conflicting. Multi-objective optimization remains an open area, and more research efforts are needed to develop an efficient and effective optimization scheme.

CHAPTER III

MULTI-OBJECTIVE ACCELERATED PROCESS OPTIMIZATION OF PART
GEOMETRIC ACCURACY IN ADDITIVE MANUFACTURING

2.9 Introduction

2.9.1 Objective and hypothesis

The goal of this work is the optimization of Additive Manufacturing (AM) process parameters at which parts with the least geometric inaccuracy are obtained. This goal is a key milestone in ensuring the commercial viability of AM. Despite extensive automation, the poor geometric consistency of AM parts prevents their use in mission-critical components in aerospace and defense applications [75]. Currently, cumbersome factorial-based design of experiments tests are used to find the optimal set of AM process parameters that will minimize the geometric inaccuracy of the part, often assessed in terms of the geometric dimensioning and tolerancing (GD&T) characteristics. To overcome this challenge, the objective of this work is to develop and apply a multi-objective optimization approach to balance between multiple requirements, and thereby produce parts with the least geometric inaccuracy with the fewest trials. The central hypothesis is that decomposing the multi-objective problem of minimizing the geometric inaccuracy into a series of simpler single-objective optimization problems leads to reduction of experimental trials compared to conventional full factorial designed of experiments (DoE) method. This hypothesis is tested against experimental data from the Fused Filament Fabrication (FFF)

process. This work leads to understanding how to balance different GD&T characteristics specified for a part using FFF process parameters, namely, (I_f) and extruder temperature (t_e) as the primary control.

2.9.2 Motivation

The motivation for this work, stemming from our previous studies, is demonstrated in Figure 2.16 [6,76–78]. At the outset, we note that the intent of this example is not to claim that there is an inadequacy with the standardized geometric dimensioning and tolerancing (GD&T) characteristics but to illustrate the difficulty in balancing between several tight geometric accuracy requirements for an AM part (in terms of GD&T characteristics).

For instance, Figure 2.16 shows the flooded contour plot for four different parts fabricated by FFF process. A flooded contour plot translates the geometric deviations of the part to the corresponding spatial locations in terms of colors. Each flooded contour plot in Figure 2.16 is constituted from 2 million three-dimensional coordinate data points for a benchmark test artifact part called circle-square-diamond used in this research; see Sec. 3.1 for details. It is visually evident in Figure 2.16 that printing under different infill percentages (I_f)—a FFF process parameter—results in different part geometric accuracies. It is apparent that the parts in Figure 2.16 (a), (b), and (c) with $I_f = 70, 80$ and 90% , respectively, are better overall than the last one shown in Figure 4.1 (d) with $I_f = 100\%$ in terms of geometric accuracy; however, it is often difficult to find a set of process parameters that will globally minimize all the specified geometric inaccuracies.

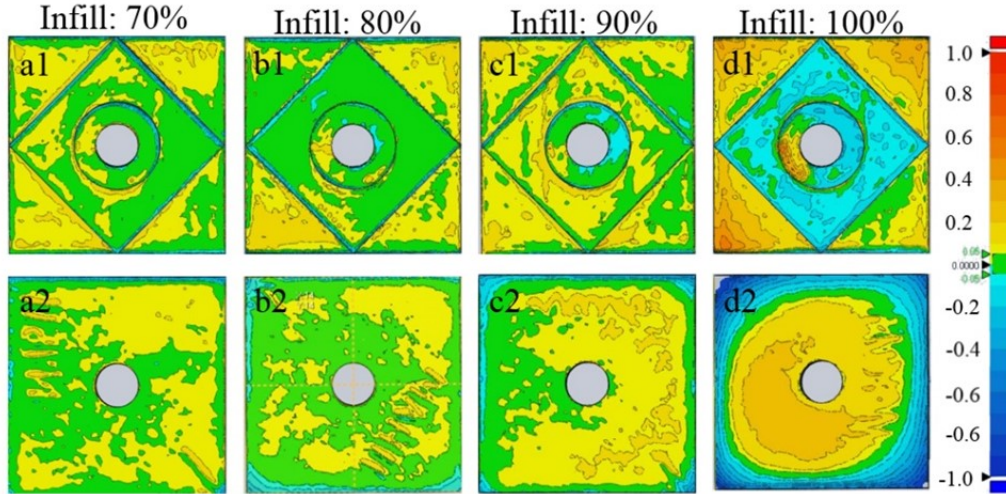


Figure 2.16 Flooded contour plots (deviation maps) of the benchmark part used in FFF experiments detailed in Sec. 2.11.1.

The material is ABS polymer. The first row (1) shows the top-views and the second row (2) contains the bottom-views of the parts. Figures a-d represent different parts, printed under 70%, 80%, 90%, and 100% infill percentages at 230 °C, respectively. The reference scale is in mm [6,76–78].

The geometric accuracy for parts shown in Figure 2.17 were specified in terms of GD&T characteristics, such as circularity, flatness, cylindricity, etc. (see Sec. 2.11.1 for details). Experimental data, plotted in Figure 2.17 reveals the difficulty in balancing between the geometric accuracy requirements based on adjusting a few process parameters. Specifically, in Figure 2.17 it is evident that both concentricity and flatness deviations for parts made by varying infill (I_f) and extruder temperature (t_e) cannot be minimized simultaneously. The combination of high I_f and low t_e tends to result in low deviations in concentricity (blue area in the upper left corner of Figure 2 (a)). However, the same process parameter set results in high level of geometric deviations in terms of part flatness (green area in the upper left corner of Figure 2.17 (b)). Accordingly, this work addresses the

following open research question in AM: what experimental plan is required to optimize process parameters with respect to multiple geometric accuracy requirements?

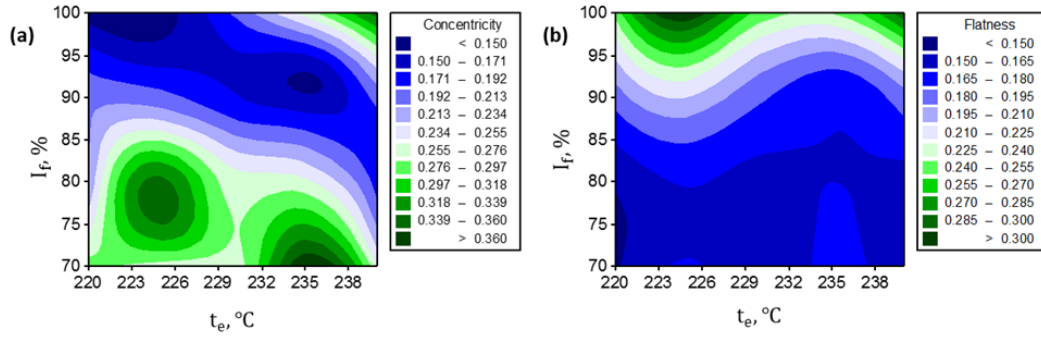


Figure 2.17 Contour plot of (a) part concentricity and (b) flatness vs. infill percentage (I_f) and extruder temperature (t_e).

2.9.3 Research challenges and overview of the proposed approach

AM offers the unique opportunity to create complex geometries and tailored surface morphologies with multiple materials; enable rapid repairs and replacement of parts in battlefield environments; simplify the overall prototyping cycle; and significantly shorten the logistical supply chain [2]. Despite these paradigm-shifting capabilities, poor process repeatability remains an imposing impediment to commercial-scale exploitation of AM capabilities. The uncertainty associated with the morphology of the sub-surface and microstructure, surface finish, and geometry of the finished part is a major concern for use of AM parts in strategic industries important to the national interest, such as aerospace and defense [75].

Efforts are ongoing in industry and academia to understand the causal AM process interactions that govern part quality. Thermo-mechanical models have been proposed as

an avenue for predicting the part properties, e.g., geometric shrinkage of AM parts [15,79]. However, the current research is in its embryonic stage and largely restricted to simple geometries such as cubes and cylinders. These elementary models cannot, as yet, capture the complex process interactions that affect parts with intricate geometries. Accordingly, data-driven approaches for compensating for AM part geometry distortions have been recently proposed [8–10]. However, these studies are also restricted to elementary shapes, and are limited to modeling of uniaxial geometry deviations.

Hence, in the absence of practically applicable physical models, DoE methods are employed to identify, quantify, and optimize key process parameters with respect to mechanical properties, such as surface roughness, fatigue, tensile strength, among others, in AM processes. These methods traditionally involve identifying existing patterns in experimental data; sampling the process space at predefined levels; and subsequently developing surrogate statistical models to approximate targeted objective functions.

For most practical cases, several geometric accuracy requirements must be satisfied together. This is a multi-objective process optimization problem with multitude of open research challenges:

- Understanding how to balance different GD&T characteristics specified for the part using process parameters as the primary control.
- The correlations amongst responses of interest are not typically known *a priori*. There is often a tradeoff between different responses. A process parameter set that produces favorable results for one geometric characteristic of part (e.g., concentricity) may be detrimental for another geometric characteristic (e.g., flatness).

- Developing a reliable empirical model for multiple responses requires a large number of experimental runs. Hence, building parts with various AM processing parameters and subsequent testing for each response mandates significant investment of both time and resources.

This work addresses these challenges by forwarding a Multi-objective Accelerated Process Optimization (m-APO) approach to find the AM process parameters that minimizes part geometric inaccuracies with fewer experimental trials compared to existing DOE methodologies. This method, presented in Sec. 3, consists of the following sequential steps:

- (1) The concept of scalarization is used to convert the multi-objective problem into a sequence of single-objective sub-problems.
- (2) The Accelerated Process Optimization (APO) method—developed in a previous study [1]—is used to solve the single objective sub-problems.
- (3) A stopping criterion is defined for the current sub-problem.
- (4) Sub-problems are chosen to uncover intermediate sections of the Pareto front (Pareto front is the set of non-dominated or non-inferior solutions in the objective space.).

By applying the proposed multi-objective optimization scheme, experimental results from previous sub-problems are leveraged as prior data for the remaining sub-problems to accelerate the multi-objective process optimization. Information captured from previous sub-problems facilitates an experimental design for accelerated optimization of the remaining sub-problems. This eschews conducting experiments again for each sub-problem and this subsequently reduces experimental burden. The practical utility of the proposed methodology is validated in Sec. 2.12.1 for the geometric accuracy optimization

of parts made using FFF polymer AM process. The applicability of the approach to a broader set of challenging non-convex optimization domains is demonstrated in a series of simulation studies in Sec. 2.12.2.

The remainder of this article is organized as follows. In Sec. 2.10, we review the existing literature addressing the problem of geometric accuracy optimization in AM processes and the multi-objective optimization techniques. In Sec. 2.11, the proposed approach is described in-depth. In Sec. 2.12, the proposed approach is demonstrated in context of the FFF process, as well as simulated cases. Lastly in Sec. 2.13, conclusions are summarized and directions for future work are discussed.

2.10 Literature review

We divide the literature review into two subsections: (1) the existing literature in AM process optimization specific to geometric accuracy; and (2) relevant multi-objective optimization approaches.

2.10.1 Existing literature in geometric accuracy optimization in AM processes

We summarize some of the existing research efforts pertaining to geometric accuracy in AM processes. Bochmann *et al.* [80] studied the cause of imprecision in fused filament fabrication (FFF) systems with respect to surface quality, accuracy and precision. They found that the magnitude of errors significantly varies in x, y and z directions. Mahesh *et al.* [81] proposed a benchmark part incorporating critical geometric features for evaluating the performance of rapid prototyping systems with respect to geometric accuracy. The proposed benchmark includes geometric features such as freeform surfaces and pass-fail features.

El-Katatny *et al.* [82] measured and analyzed the error in major geometric characteristics of specific landmarks on anatomical parts fabricated by the FFF process. Weheba and Sanchez-Marsa [83] determined the optimal process settings for stereolithography (SLA) process with respect to surface finish, flatness, and deviations of diameter measures from nominal values. Second-order empirical models were developed for the different characteristics, but only a single set of process parameters was given as the optimal design. Indeed, there should be tradeoffs for the different responses. Tootooni *et al.* [76,77] and Rao *et al.* [7] used a spectral graph theory methodology to quantify and assess geometric accuracy of FFF parts using deviations of 3D point cloud coordinate measurements from design specifications. Although the proposed indicator facilitates comparing the geometric accuracy of parts it DoEs not propose a relationship between process parameters and geometric accuracy in terms of GD&T characteristics. Huang *et al.* [8–10] developed a framework to model part shrinkage in SLA, thereby optimizing shrinkage for better geometric accuracy. This work is limited to elementary geometric shapes and DoEs not determine an optimal range of process parameters for the best geometric accuracy of parts.

Experimental data from our initial screening studies (see Sec. 2.11.1) show that the optimization of geometric accuracy for AM parts is a multi-objective optimization problem (i.e., the correlations among geometric characteristics are negative). As an example of multi-objective optimization in AM, Fathi and Mozaffari [28] optimized the direct energy deposition process in terms of three response characteristics—clad height (deposition layer thickness), melt-pool depth and dilution—in a two stage manner. First, empirical models that represent the relationship between the key process parameters, i.e., laser power,

powder mass flowrate, and scanning speed, and the two response characteristics were developed using a smart bee algorithm and a fuzzy inference system. Then, in the second stage, NSGA-II (Non-dominated Sorting Genetic Algorithm)—a well-known multi-objective optimization evolutionary algorithm—is employed to achieve the best Pareto points in the objective space. Although this work was able to handle a multi-objective process optimization problem, it required several experimental runs (50 experiments) to establish a set of viable empirical models. As mentioned previously, the prohibitive experimental effort remains an intrinsic challenge with the conventional DoE methods.

2.10.2 Background in multi-objective optimization

Multi-objective optimization methods can be grouped in two main categories: (i) scalarization or aggregation-based methods; and (ii) evolutionary algorithms [84]. Scalarization methods, which represent a classic approach, combine multiple objective functions into a single-objective problem, enabling the use of single objective optimization methods to solve the problem [85]. These methods are not adaptable for the current multi-objective geometric accuracy optimization problem in AM because the individual objective functions are not explicitly known. In contrast, evolutionary algorithms iteratively generate groups of potential solutions that represent acceptable compromises between objective functions [86]. The disadvantage of this approach is that the objective functions require a large number of candidate solutions to be evaluated, i.e. many AM experiments for the current multi-objective geometric accuracy optimization problem.

Other multi-objective optimization approaches share similar disadvantages. For instance, Kunath *et al.* [87] applied a full factorial design of experiments for three process parameters to develop a set of regression models as the functional form of objective

functions representing the binding properties of a molecularly imprinted polymer. Then by assigning predefined desirability values, i.e., weight coefficients, for dependent response variables, a range of process parameters resulting in the highest desirability values is introduced as optimal. Again, this approach presents challenges for most AM processes since many process parameters are involved and a large number of experiments may be required to fit regression models within tight confidence bounds. Therefore, there are critical research gaps and numerous technical challenges pertaining to process optimization for geometric accuracy of multiple AM part geometric characteristics.

2.11 Methodology

2.11.1 Description of the experimentally obtained geometric accuracy data

A systematic optimization approach for improving the geometric accuracy of AM parts is motivated by the experimental response data collected for a benchmark part. The presented experimental data in this work is generated in the authors' previous research [6,76–78]. The so-called circle-diamond-square part is designed as the benchmark part of interest for geometrical optimization (Figure 2.18) [88,89]. This is based on the NAS 979 standard part used in the industry for assessing the performance of CNC machining centers [90]. Circle-diamond-square is useful for assessing the performance of AM machines with respect to part geometric accuracy. For instance, the outside square (lowest layer) can be used to measure the straightness of an individual axis and the squareness across two axes in FFF. The diamond feature (middle layer) can be used to measure the rotation among two axes (i.e., from the bottom to middle layer). The large circle feature (top layer) can be used to measure the circular interpolation of two axes [88,91]. By axes we refer to the FFF machine gantry on which the nozzle is rastered.

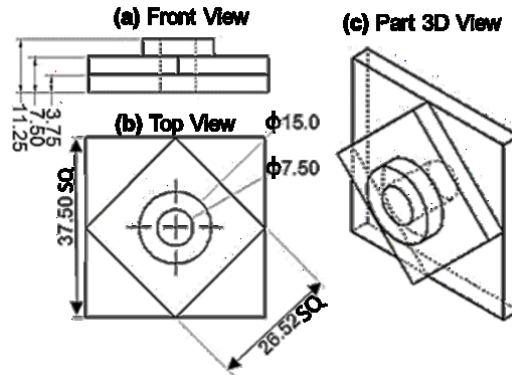


Figure 2.18 Design of the circle-square-diamond part.

A simplified embodiment of the NAS 979 standard test artifact for testing accuracy of machining centers [90]. The dimensions are in millimeters. (a) and (b) are front view and top view of the part, respectively; and (c) is an isometric projection of the part [6,76–78].

Five important GD&T characteristics are specified: flatness, circularity, cylindricity, concentricity and thickness (see Figure 2.19). These GD&T characteristics are chosen because they are independent of the feature size - also called regardless of feature size (RFS) characteristics. More detail about GD&T characteristics can be found in [92]. We did not specify positional tolerances on the part because matching a datum surface from laser scanned point cloud data was found to be exceedingly error prone. Additionally, we concede another weakness with this work; it is likely that the GD&T characteristics specified for the circle-square-diamond test artifact might entail that the part is over tolerated or constrained and probably beyond the capability of the desktop FFF machine used in this work. Our rationale is to use this test artifact, albeit as an extremely contrived case, to explore a larger theme — understanding how to balance different GD&T characteristics specified for the part using FFF process parameters, namely, (I_f) and extruder temperature (t_e) as the primary control. This is the primary contribution of this work.

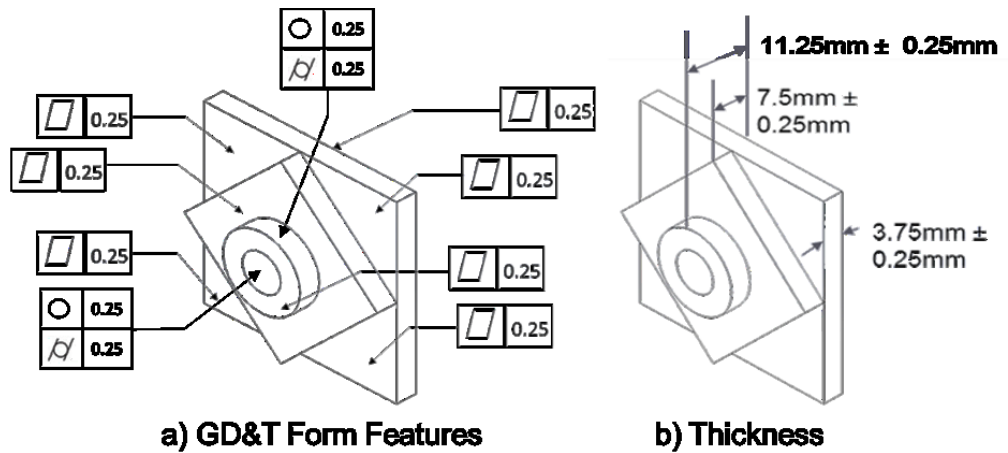


Figure 2.19 The areas used to measure GD&T form the design part.

Sub-figure (a) shows the faces used to measure flatness (\square), circularity (\bigcirc), and cylindricity (||); and (b) shows the planes used to measure the thickness – three thickness measurements are taken on each plane [6,76–78].

The aim is to minimize the magnitude of deviations within these five GD&T characteristics of parts from the targeted design specifications. A NextEngine HD 3D laser scanner was used to capture part geometric data and the QA Scan 4.0 software¹ was used to estimate the deviations from the targeted design specifications [6,76–78]. Figure 2.17 (see Sec. 2.9.2) shows examples of contour plots of absolute value for deviations within flatness and concentricity versus two controllable FFF process parameters: infill percentage (I_f) and extruder temperature (t_e).

In practice, the laser scanning is a heuristic process that requires adhering to a carefully attuned procedure, particularly, in the manner in which the part is aligned to the computer-aided design (CAD) model to obtain consistent results. The alignment step requires matching of at least four landmark points from the raw point cloud data with CAD model. Several trials are conducted and herewith summarized is a method that showed the

¹ <http://www.nextengine.com/products/qa-scan/intro>

least variability. Four points each on the square and diamond portions are used to align the part as depicted in Figure 2.20. Additionally, laser scanning was conducted on a sturdy, vibration-free table in a darkened closure, and by coating the part with a thin layer of anti-reflective gray modeling paint.

The data scatter plot matrix for the GD&T characteristics, called correlation matrix is shown in Figure 2.21. The slope of lines represents the Pearson correlation coefficient (ρ) for pairs of GD&T characteristics. It is evident from Figure 2.17, Figure 2.21, and Table 2.17 (see Sec. 2.12.1) that flatness and concentricity are not positively correlated ($\rho = -0.21$). Similarly, thickness and concentricity are negatively correlated ($\rho = -0.63$). In other words, it is not possible to simultaneously optimize GD&T characteristics. Hence, optimization for geometric accuracy is best considered as a multi-objective optimization problem, and the set of process parameters setups should consider the tradeoff between multiple geometric characteristics.

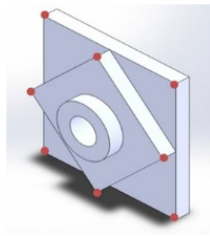


Figure 2.20 The eight points used for alignment of the scan points with the CAD model.

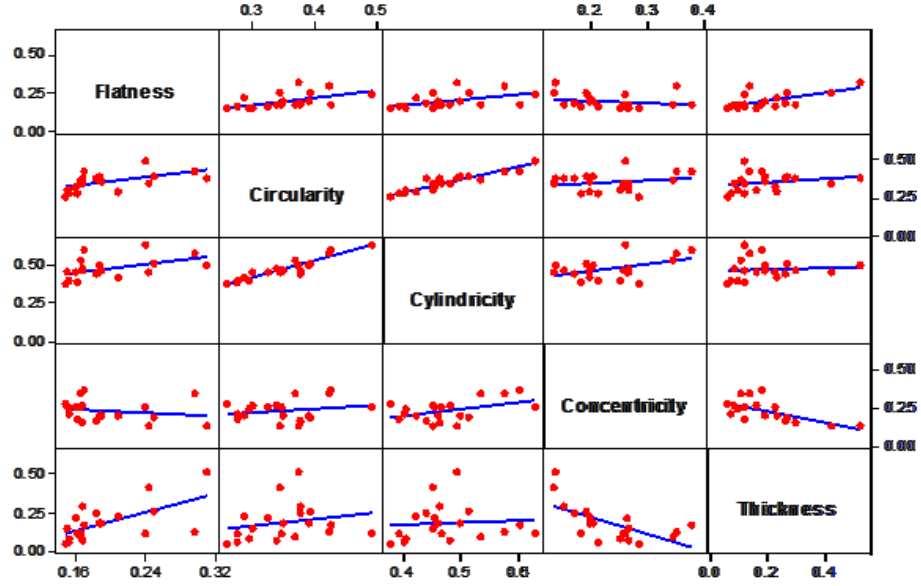


Figure 2.21 The representation of the data scatter plot matrix to illustrate both positive and negative correlations among pairs of part geometric characteristics.

The slope of lines illustrates the Pearson correlation coefficient (ρ) for pairs of GD&T characteristics.

2.11.2 Multi-objective process optimization

The aim of this section is to elucidate the mathematical foundation for multi-objective process optimization in AM. We illustrate the case with two objective functions. The proposed methodology is extensible to multi-objective cases.

2.11.2.1 Scalarization of multi-objective optimization and Pareto front

The methodology developed herein is a generalization of an existing Accelerated Process optimization (APO) methodology, developed in the form of maximization [1]. A minimization problem can be expressed in the form of maximization by multiplying the objective function by negative sign (and vice versa).

Suppose the problem is to maximize two objective functions (or response variables Y_1 and Y_2). The bi-objective maximization problem is expressed as follows:

$$\text{Max } \mathbf{Y}(\mathbf{s}) = (Y_1(\mathbf{s}), Y_2(\mathbf{s}))' \quad (4.1)$$

$$\text{s.t. } \mathbf{s} \in \mathbf{S}$$

$\mathbf{Y}(\mathbf{s})$ denotes the vector of objective functions $(Y_1(\mathbf{s}), Y_2(\mathbf{s}))'$, and \mathbf{s} is the vector of process parameters (e.g., infill percentage (I_f) and extruder temperature (t_e)); and \mathbf{S} denotes the design space, which includes all possible values of \mathbf{s} . The objective space, i.e., the set of all possible response vectors \mathbf{Y} corresponding to the design space, is denoted by $\mathbf{C} = \{(Y_1(\mathbf{s}), Y_2(\mathbf{s}))' \in \mathbb{R}^2: \mathbf{s} \in \mathbf{S}\}$.

For most AM applications, the functional expressions of $(Y_1(\mathbf{s}), Y_2(\mathbf{s}))$ are unknown; the empirical relationship between geometric accuracy responses and AM process parameters is yet to be understood and quantified. Moreover, the correlation between $Y_1(\mathbf{s})$ and $Y_2(\mathbf{s})$ is also unknown. Higher value of $Y_1(\mathbf{s})$ may result in lower value of $Y_2(\mathbf{s})$ or converse. In other words, the optimized process parameters for Y_1 may not necessarily result in favorable Y_2 due to the possible low or even negative correlation between two response variables. For instance, concentricity and flatness shown in Figure 2.17 are negatively correlated. Consequently, improving the response value of flatness will result in worsening concentricity. Therefore, the optimal solution to the multi-objective optimization problem is non-unique. Our objective is to develop a systematic and sequential DOE procedure that efficiently identifies sets of optimal solutions as a tradeoff between such contradictory response behaviors.

For this purpose, the optimization problem is converted into a sequence of single-objective problems by defining weight coefficients for each objective. In this way, the bi-objective optimization problem can be presented as a sequence of single objective

optimization problems, each defined by the sub-problem index variable h , with $h = 1, 2, 3, \dots, m$ as shown below:

$$\text{Max } Z^h(\mathbf{s}) = \gamma_1^h \cdot Y_1(\mathbf{s}) + \gamma_2^h \cdot Y_2(\mathbf{s}) \quad (4.2)$$

$$\text{s. t. } \mathbf{s} \in \mathbf{S}$$

$$\text{where } \gamma_1^h + \gamma_2^h = 1$$

$$\gamma_k^h \geq 0, \quad \forall k = 1, 2$$

For each sub-problem with index h , γ_k^h denotes weight coefficient corresponding to the k^{th} objective function. $k = 1$ and $k = 2$ in the formulation above, satisfying the constant $\gamma_1^h + \gamma_2^h = 1$. Different weight coefficients correspond to different sub-problems and will accordingly lead to different optimal solutions.

For example, consider a sub-problem with $\gamma_1^1 = 0.8$ and $\gamma_2^1 = 0.2$. In this case, the single objective optimization problem is expressed in the form of $\text{Max } (0.8Y_1(\mathbf{s}) + 0.2Y_2(\mathbf{s}))$. The weight coefficients (γ_k^h) are graphically shown in Figure 2.22 by the tangent of a line, which represents the desired search direction for the current single objective maximization function (sub-problem h). Changing the corresponding weight coefficients changes the single objective function being optimized. For example, consider a second sub-problem with $\gamma_1^2 = 0.2$ and $\gamma_2^2 = 0.8$; the optimum solution for problem $\text{Max } (0.2Y_1(\mathbf{s}) + 0.8Y_2(\mathbf{s}))$ is not the same as that in the first sub-problem. In real-world applications simultaneously achieving the best individual solution for two negatively correlated (or uncorrelated) objectives is intractable. Hence, in these cases, the optimum solution is a subset of objective space \mathbf{C} which can recognize and identify the best tradeoff among the

value of Y_1 and Y_2 . In what follows, we discuss in details the approach to identify the sets of process parameter setups that results in an optimal objective value with different weight coefficients.

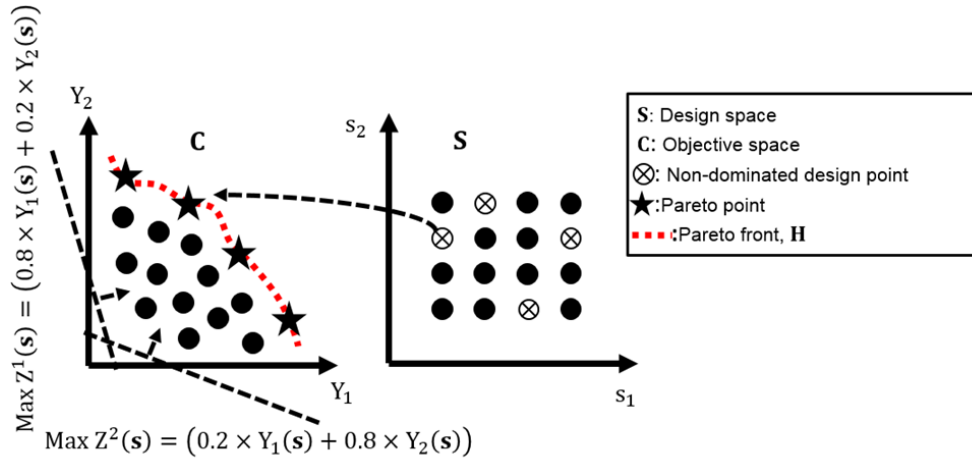


Figure 2.22 Schematic illustration of design space, objective space, non-dominated design points, Pareto points and Pareto front.

We focus on identifying the Pareto optimal solutions associated with the multi-objective optimization problem. A Pareto optimal solution is not dominated by any other feasible solution and represents the best compromise between multiple objective functions. We define each member of Pareto optimum as a design point $\mathbf{s}^* \in \mathbf{S}$ if and only if there is no other $\mathbf{s} \in \mathbf{S}$ such that $Y_k(\mathbf{s}) \geq Y_k(\mathbf{s}^*)$ for $k = 1, 2$. Here, \mathbf{s}^* is called a non-dominated design point and its corresponding response vector in the objective space is a Pareto point, $Y_k(\mathbf{s}^*)$. Regarding geometric accuracy optimization, a Pareto point indicates an optimal design point where there is no other solution that results in better values in term of any geometric responses. The Pareto optimum set is denoted by \mathbf{E} . In the bi-objective

optimization problem shown in Eq. (4.1), the Pareto front representing response vectors of the Pareto set in the objective space \mathbf{C} is defined by \mathbf{H} , that is $\mathbf{H} = \{(Y_1(\mathbf{s}), Y_2(\mathbf{s}))' \in \mathbb{R}^2: \mathbf{s} \in \mathbf{E}\}$. Given two controllable process parameters for the purpose of demonstration the terms design space, objective space, non-dominated design point, the Pareto point and Pareto front for a bi-objective optimization problem are illustrated in Figure 2.22.

2.11.2.2 Multi-objective Accelerated Process Optimization (m-APO)

Our approach is to solve the bi-objective optimization problem presented in Eq. (4.2) by obtaining a well-distributed set of Pareto points and thereby approximate the Pareto front with reduced number of experimental runs. Conventional scalarization divides the multi-objective optimization problem into individual single-objective problems and optimizes them individually. The proposed Multi-objective Accelerated Process Optimization (m-APO) method, in contrast, leverages a knowledge-guided optimization approach based on the similarity among different sub-problems. The proposed methodology is initially developed by preliminary studies [93,94] to deal with multi-objective AM process optimization problems.

Each single objective sub-problem is solved using the Accelerated Process Optimization (APO) method, which uses results from prior experiments to accelerate the process optimization [1]. APO balances two important properties simultaneously, i.e., optimization and space-filling. For optimization, more trial runs are needed in the regions of \mathbf{s} which potentially result in the maximum value of the response function $Z^h(\mathbf{s})$. In contrast, to avoid being trapped in a local optimum, the space-filling aspect is also considered. In the APO approach, each design point is assigned a so-called positive charge

denoted by $q^h(\mathbf{s}_j)$. Selection of the charge function $q^h(\mathbf{s})$ relies on the optimization objective. Considering the maximization objective in our case, the charge function $q^h(\mathbf{s})$ should be inversely proportional to the weighted single objective response values $Z^h(\mathbf{s})$ from Eq. (4.2) [1,51]. Thus, higher magnitude charges are assigned to design points with lower $Z^h(\mathbf{s})$ and vice versa. Analogous to the physical laws of static charged particles, the design points repel each other apart to minimize the total electrical potential energy amongst them. Hence, design points with lower $Z^h(\mathbf{s})$, i.e., with higher charge, strongly repel other design points. On the other hand, design points with higher $Z^h(\mathbf{s})$, i.e., with lower electrical charge, accommodate more design points in their neighborhood. The resulting positions correspond to the minimum potential energy amongst charged particles. Accordingly, more design points with lower charge potentials (i.e., higher $Z^h(\mathbf{s})$ values) are selected to sequentially maximize the objective function of interest in the current sub-problem, i.e., $Z^h(\mathbf{s})$.

The potential energy between any two design points \mathbf{s}_i and \mathbf{s}_j is equal to $q(\mathbf{s}_i)q(\mathbf{s}_j)/d(\mathbf{s}_i, \mathbf{s}_j)$, where $d(\mathbf{s}_i, \mathbf{s}_j)$ represents the Euclidean distance between \mathbf{s}_i and \mathbf{s}_j . Hence, total potential energy function within h^{th} sub-problem including the n^{th} new design is formulated as follows:

$$E_n^h = \sum_{i=1}^{n-1} \sum_{j=i+1}^n \frac{q^h(\mathbf{s}_i)q^h(\mathbf{s}_j)}{d(\mathbf{s}_i, \mathbf{s}_j)} \quad (4.3)$$

The new design point can be obtained by solving $\mathbf{s}_n = \text{argmin } E_n^h$.

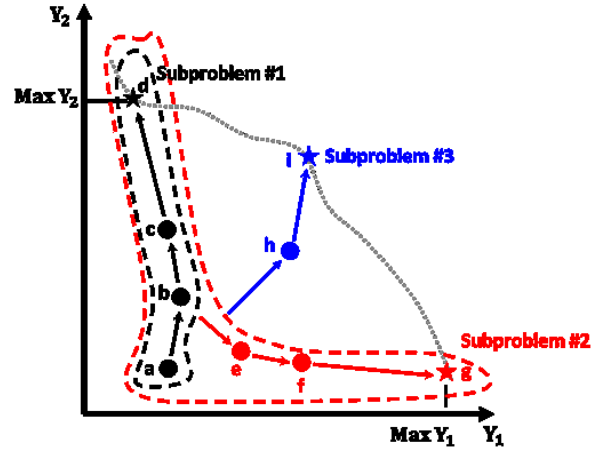


Figure 2.23 Leveraging the information from prior data to accelerate solving subsequent sub- problems.

At each step, Pareto points are identified based on the non-domination concept. Afterwards, the appropriate weight coefficients for the next sub-problem are chosen to lead the next sub-problem optimization in such a way that maximizes the distribution of the Pareto points. Instead of solving each optimization sub-problem individually and independently, experimental data obtained from previous sub-problems are used as prior data to accelerate optimization process for the subsequent sub-problems. For example, in Figure 2.23 experimental data from sub-problem 1 and 2 (represented by segments a-b-c-d and e-f-g, respectively) accelerate the optimization process for sub-problem 3 (segments h-i). In other words, fewer numbers of experiments are needed to reach the Pareto point corresponding to the sub-problem 3. This is due to the fact that experimental data obtained from previous sub-problems contribute to designing experiments for the next sub-problems. Hence, we do not need to design the experiments from scratch for each sub-problem. This process is continued until the improvement in the resulting Pareto front is

insignificant. The area dominated by Pareto points on the objective space is used to measure the efficiency of the resulting Pareto points. The proposed method accelerates the bi-objective optimization process by jointly solving the sub-problems in a systematic manner. In fact, the method maps and scales experimental data from previous sub-problems to guide remaining sub-problems that improve the Pareto front while reducing the number of experiments required. The algorithm is described herewith in detail, and summarized in Figure 2.24.

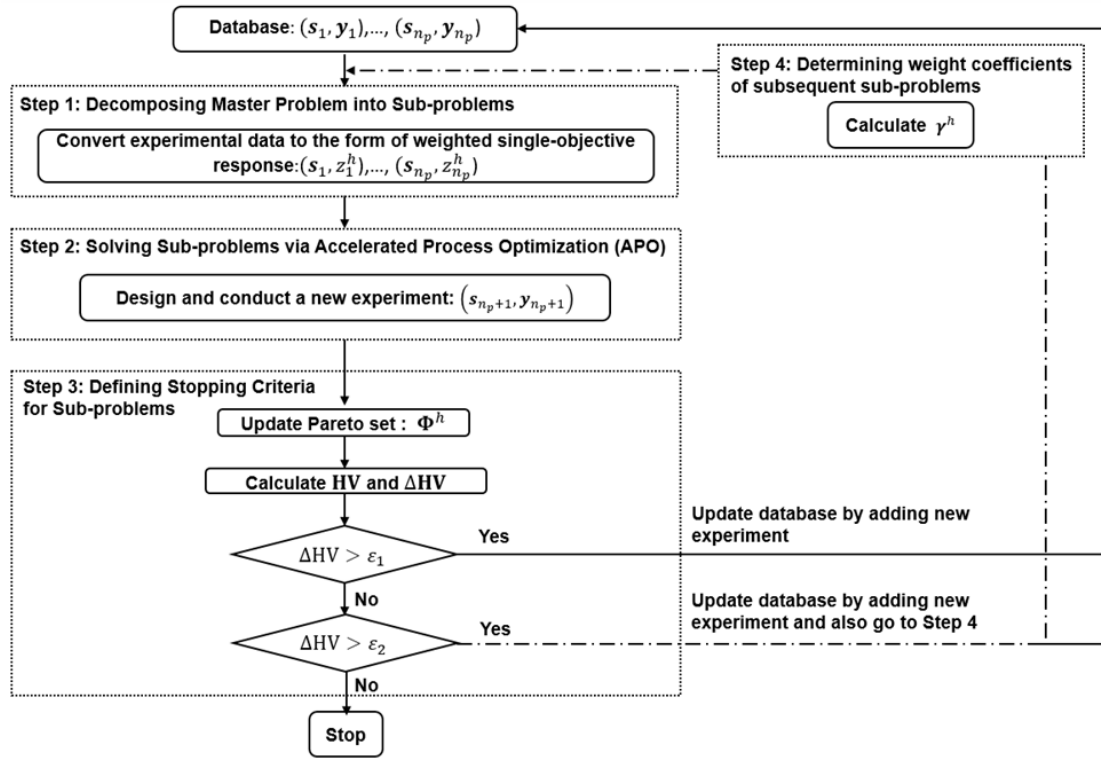


Figure 2.24 Multi-objective Accelerated Process Optimization (m-APO) flowchart.

- **Step1: Decomposing master problem into sub-problems**

The master bi-objective optimization problem $\text{Max } \mathbf{Y}(\mathbf{s}) = (Y_1(\mathbf{s}), Y_2(\mathbf{s}))'$ (see Eq. (4.1)) is decomposed into a sequence of single objective functions, each of which is expressed as a convex combination of the objective functions (see Eq. (4.2)). We initialize the algorithm with optimizing two boundary sub-problems with $(\gamma_1^1 = 0, \gamma_2^1 = 1)$ and $(\gamma_1^2 = 1, \gamma_2^2 = 0)$. The solution to the first two sub-problems resulted in two end points of the Pareto front (i.e., points d and g in Figure 2.23).

- **Step2: Solving sub-problems via accelerated process optimization (APO)**

Using APO [1], we sequentially design experiments to optimize the constructed single objective sub-problems. Experimental data generated from previous sub-problems are treated as prior data for subsequent sub-problems. Assuming that weight coefficients (γ_1^h, γ_2^h) are determined, all the design points represented in the response vector form, $(\mathbf{s}_i, \mathbf{Y}_i)$, are converted to the form of weighted single-objective response data as (\mathbf{s}_i, Z_i^h) in the framework of APO.

The design points and corresponding weighted single objective response are incorporated and applied throughout the APO algorithm, i.e., \mathbf{s}_i and $Z_i^h(\mathbf{s}_i) = \gamma_1^h \cdot Y_1(\mathbf{s}_i) + \gamma_2^h \cdot Y_2(\mathbf{s}_i)$. All the experimental data attained during the optimization process of prior sub-problems (i.e., sub-problems 1, 2, ..., $h - 1$) are transformed and fed into the APO of the h^{th} sub-problem as prior data to accelerate optimization process of the current sub-problem by predicting the weighted single objective responses in a more accurate manner. The new design point can be obtained by solving $\mathbf{s}_n = \text{argmin } E_n^h$, where E_n^h is the total energy function defined in Eq. (4.3). Detailed discussion about the computation of the energy

function and predicting the single-objective response values for the new untested design points can be found in Ref. [1].

- **Step3: Defining stopping criteria for sub-problems**

To define the stopping criteria, we use the Hyper-Volume (HV) metric as measure of the Pareto points' contribution [95]. By definition, HV is the volume in the objective space dominated by resulting Pareto points; a higher HV results in better coverage of the Pareto front and thus provides the better solution. In Figure 2.25 light gray area is the HV associated with gray Pareto points. ΔHV , which is the contribution of new Pareto point, is represented by the dark gray rectangle area. The algorithm is repeated designing experiments for the current sub-problem until ΔHV is less than a pre-specified threshold (i.e., $\Delta HV < \varepsilon_1$). The proposed algorithm stops continuing introducing further sub-problems and designing more experiments when we do not observe significant improvement in ΔHV (i.e., $\Delta HV < \varepsilon_2$).

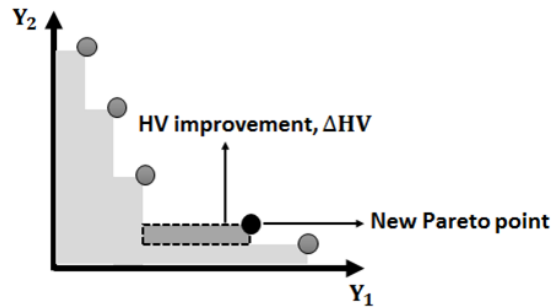


Figure 2.25 Schematic illustration of HV (Hyper-Volume) as the measure of the contribution of Pareto points.

- **Step4: Determining weight coefficients of subsequent sub-problems**

Based on the resulting Pareto points obtained at the end of each sub-problem, weight coefficients for the next sub-problem, γ^h , are calculated as follows. Noting that upper case letters represent the unknown variables in this paper, while lower case letters are used for known variables. Assuming that after solving the $(h - 1)^{th}$ sub-problem, the Pareto set $\Phi^{h-1} = \{(\mathbf{s}_1^*, \mathbf{y}_1^*), (\mathbf{s}_2^*, \mathbf{y}_2^*), \dots, (\mathbf{s}_m^*, \mathbf{y}_m^*)\}$ including m non-dominated design points and corresponding actual response vectors are obtained. Thereafter all the existing optimal parameter setups are sorted in increasing order of $y_1(\mathbf{s})$ and labeled as $\Psi^{h-1} = \{\mathbf{s}_{(1)}^*, \mathbf{s}_{(2)}^*, \dots, \mathbf{s}_{(m)}^*\}$. At this stage, the Euclidean distance between all of the neighboring Pareto points is calculated as follows:

$$\delta_j = |\mathbf{y}(\mathbf{s}_{(j+1)}^*) - \mathbf{y}(\mathbf{s}_{(j)}^*)| \quad \text{for } j = 1, \dots, (m - 1)$$

Then, the maximum gap on the existing Pareto front is determined by $\Delta = \max_{j=1, \dots, (m-1)} \delta_j$. If two neighboring Pareto points corresponding to Δ are \mathbf{s}_a^* and \mathbf{s}_b^* , where $y_1(\mathbf{s}_a^*) < y_1(\mathbf{s}_b^*)$, the weight coefficients for the next sub-problem is computed as $\gamma^h = c^h(y_2(\mathbf{s}_a^*) - y_2(\mathbf{s}_b^*), y_1(\mathbf{s}_b^*) - y_1(\mathbf{s}_a^*))$, where c^h is a constant leading to $\gamma_1^h + \gamma_2^h = 1$. Accordingly, we can achieve a uniform coverage of Pareto front in an efficient manner.

2.12 Experimental and numerical studies

We now apply and demonstrate the proposed approach to experimental and simulated data. We first apply our method to a real-world case study for minimizing the deviation in geometric characteristics of parts produced using FFF AM process. Since the experimental data includes measurement of five GD&T characteristics, we first use the PCA (Principal Component Analysis) procedure to reduce the dimension of objective space

to the first two PCs, which account for 88.15% of total data variation. Subsequently, the proposed optimization method is applied to minimize absolute values of the first two PCs. The results show that m-APO methodology achieves all true Pareto points in the objective space with 20% fewer experiments compared to a full factorial DOE plan.

To further validate our methodology and test its robustness, we also conducted numerical studies with different number of input parameters and characteristics of objective space and Pareto fronts [95–98].

2.12.1 Experimental case study: multi-geometric characteristic optimization of parts fabricated by FFF system

The aim of this section is to apply the proposed m-APO method for optimizing the geometric accuracy of AM parts. Samples are fabricated using a polymer extrusion AM process called Fused Filament Fabrication (FFF). They are made with acrylonitrile butadiene styrene (ABS) thermoplastic on a desktop machine (Makerbot Replicator 2X). A schematic of the FFF process is shown in Figure 2.26. Based on the initial screening designs we take two important controllable process parameters including percentage infill (I_f) and extruder temperature (t_f) [6,76–78]. Extruder temperature is the temperature at which the filament is heated in the extruder. Infill relates to the density of the part, for instance 100% infill corresponds to a completely solid part. The target is to minimize absolute deviations concerning five major GD&T characteristics, namely flatness, circularity, cylindricity, concentricity and thickness, from the targeted design specifications. Since the m-APO methodology is expressed in the form of maximization problem, the response values in case study are multiplied by a negative sign.

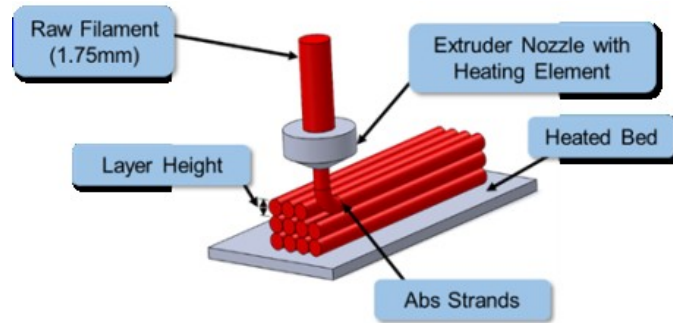


Figure 2.26 A schematic diagram of the FFF process [76,77].

The twenty experimental data used in the present study are resulted from previous published works [6,76–78] which uses a full factorial DOE plan. Factors and levels corresponding to this design are illustrated by Table 2.16.

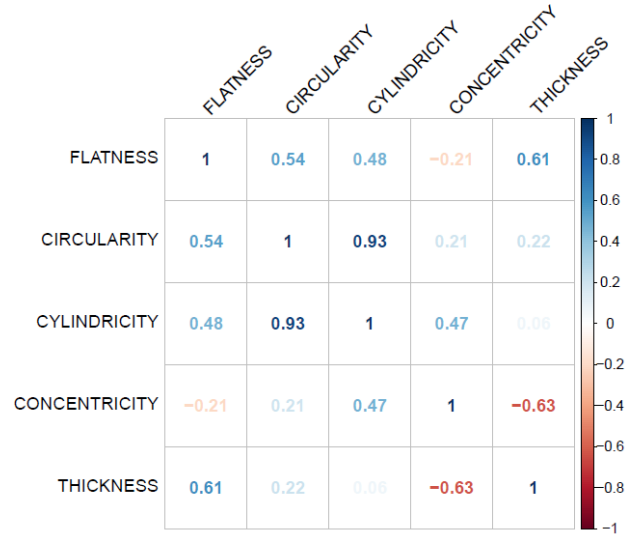
Table 2.16 Levels of the process parameters applied to generate experimental data based on full factorial DOE plan.

T_e (°C)	220	225	230	235	240
I_f (%)	70	80	90	100	

The correlation among deviations within GD&T characteristics is illustrated in Table 2.17 in terms of the Pearson correlation coefficient (ρ) for pairs of GD&T characteristics. The higher correlation coefficients are more noticeable compared with low coefficients. The correlation between cylindricity and circularity is extremely high ($\rho = 0.93$) in that both contribute to describing the circular feature of the test part in different ways. There is no any discernible pattern amongst the other GD&T correlations. In other words, the GD&T characteristics are positively correlated (e.g. $\rho = 0.93$ for cylindricity

and circularity); negatively correlated (e.g. $\rho = -0.63$ for concentricity and thickness); and nearly uncorrelated (e.g. $\rho = 0.06$ for cylindricity and thickness).

Table 2.17 Signed correlation among GD&T characteristics of benchmark part samples.



Principal component analysis is first applied to reduce the dimension of the objective space from five to two. Accordingly, the proposed bi-objective process optimization can be directly applied to the geometric accuracy optimization problem for FFF system. The principal component analysis results (see Table 2.18) show that 88.15% of variability within the parts' geometric characteristics data is captured by the first two principal components (i.e., PC_1 and PC_2). Hence, the first two PCs can sufficiently describe the data variations with very negligible loss of information. All the five variables contribute to the PC_1 by positive coefficients (Table 2.19). Flatness, circularity and cylindricity are about equally important to PC_1 with largest weight. Although concentricity's contribution is negligible in PC_1 , thickness plays a significant role in this component. Hence, PC_1 can be considered as representative of average deviations within all GD&T characteristics.

However, we see an unique pattern within PC_2 's coefficients. The variables that are related to the analogues features—i.e., circularity, cylindricity and concentricity—contribute to PC_2 with negative coefficients. Hence, PC_2 can be inferred as difference of deviations within two clusters of geometric characteristics: roundness characteristics (circularity, cylindricity and concentricity) and others (flatness and thickness).

Table 2.18 The 88.15% of variability within the parts' geometry characteristics data is captured by the first two principal components.

	PC_1	PC_2	PC_3	PC_4	PC_5
Standard deviation	1.576	1.3866	0.58981	0.46713	0.16190
Proportion of variance	0.497	0.3845	0.06958	0.04364	0.00524
Cumulative proportion	0.497	0.8815	0.95112	0.99476	1

Table 2.19 Illustrating principal components' coefficients.

	PC_1	PC_2	PC_3	PC_4	PC_5
Flatness	0.5046	0.2895	-0.7181	-0.3824	0.0481
Circularity	0.5854	-0.1598	0.4859	-0.1831	0.6016
Cylindricity	0.5607	-0.3161	0.1710	0.0901	-0.7404
Concentricity	0.0650	-0.6677	-0.4659	0.5000	0.2877
Thickness	0.2895	0.5895	0.0425	0.7496	0.0687

All the five variables contribute in the PC_1 by positive coefficients. Flatness, circularity and cylindricity are about equally important to PC_1 with largest weight.

Using the first two PCs the geometric accuracy optimization problem is formulated as follows:

$$\begin{aligned} \text{Min } \mathbf{PC}(\mathbf{s}) &= (|\mathbf{PC}_1(\mathbf{s})|, |\mathbf{PC}_2(\mathbf{s})|)' \\ \text{s.t. } &\mathbf{s} \in \mathbf{S} \end{aligned}$$

$\mathbf{PC}(\mathbf{s})$ denotes the vector of first two principal components of deviations within GD&T characteristics of the part; \mathbf{s} the vector of process parameters; and \mathbf{S} the design space.

After conducting 20 experiments using full factorial DOE plan, we attain three Pareto points in the objective space (red dots in Figure 2.27). Note that the Pareto set in this case study naturally forms a convex Pareto front. After choosing a random initial experiment (blue dot in Figure 2.27) we iteratively apply m-APO. The m-APO methodology leads to the same Pareto points after 16 experimental runs, which translates to a 20% reduction of experiment runs compared with full factorial design. Optimal process parameters and GD&T characteristics corresponding to the Pareto points are presented by Table 2.20.

Table 2.20 Optimal process parameters and corresponding GD&T values achieved in the case study

t_e (°C)	I_f (%)	Flatness	Circularity	Cylindricity	Concentricity	Thickness
220	90	0.1869	0.3905	0.5011	0.2061	0.1861
230	90	0.1823	0.3783	0.4407	0.1733	0.2604
240	90	0.1887	0.3500	0.4624	0.2001	0.1910

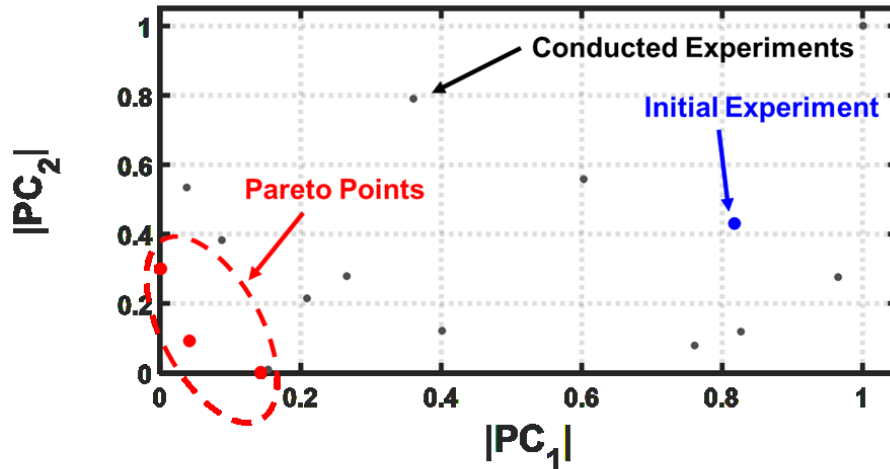


Figure 2.27 Demonstrating the Pareto points and conducted experiments for the case study.

2.12.2 Numerical simulation studies for non-convex Pareto front

As presented in the FFF case study (Sec. 2.12.1), the m-APO methodology is effective for a convex bi-objective problem. In the numerical simulation studies, the aim is to evaluate the robustness of m-APO in case of more challenging non-convex Pareto fronts, which is usually challenging for multiple objective optimization. To simulate various experimental conditions, three different combinations of design space structures and Pareto front characteristics are considered: (a) non-convex Pareto front and well-distributed objective space, (b) non-convex Pareto front and congested objective space; and (c) high dimensional design space. The ultimate goal of the simulation study is achieving a set of high quality uniformly spread Pareto points representing the true ones. We note that in reality the functional form of objectives, i.e., $Y_1(\mathbf{s})$ and $Y_2(\mathbf{s})$, are unknown and here we just present them to simulate the real experimentation.

We measure the efficiency of the m-APO methodology using GD (General Distance) and PHV (Proportional Hyper-Volume) defined as follows:

- GD (General Distance) quantifies the difference between the true Pareto points and those obtained with m-APO. Assuming that at the end of simulation N Pareto points are obtained, GD is calculated as follows [99,100]:

$$GD = \frac{\sqrt{\sum_{i=1}^N \tau_i^2}}{N}$$

where τ_i represents the minimum Euclidean distance between i th Pareto point from m-APO and true Pareto points. Smaller values in GD indicate that the Pareto points obtained from m-APO are closer to true ones; and in an ideal case, $GD = 0$.

- PHV (Proportional Hyper-Volume) is the ratio of the Hyper-Volume of the Pareto points obtained using m-APO and the Hyper-Volume of the true Pareto points:

$$\text{PHV} = \frac{\text{HV}(\text{Pareto Points obtained from m - APO})}{\text{HV}(\text{True Pareto Points})}$$

By definition, PHV falls within $[0, 1]$. In an ideal case, $\text{PHV} = 1$.

We benchmark the m-APO method against full factorial DOE by comparing GD, PHV within fix number of experiments. The results show that the m-APO method achieves significantly higher PHV and lower GD compared to full factorial DOE.

2.12.2.1 Case A: non-convex Pareto front and well-distributed objective space

The m-APO method is applied to an equally-spaced discrete design space from a commonly used bi-objective optimization test problem, OKA1. This test problem is applied to evaluate the performance of ParEGO algorithm proposed in Ref. [95,96] and benchmark it against NSGA-II (Non-dominated Sorting Genetic Algorithm). The relationship between process parameters and two objective functions are as follows:

$$\text{Max } \mathbf{f}(\mathbf{s}) = -(Y_1(\mathbf{s}), Y_2(\mathbf{s}))$$

$$Y_1(\mathbf{s}) = s_1'$$

$$Y_2(\mathbf{s}) = \sqrt{2\pi} - \sqrt{|s_1'|} + 2|s_2' - 3 \cos(s_1') - 3|^{\frac{1}{3}}$$

$$s_1' = \cos\left(\frac{\pi}{12}\right)s_1 - \sin\left(\frac{\pi}{12}\right)s_2$$

$$s_2' = \sin\left(\frac{\pi}{12}\right)s_1 + \cos\left(\frac{\pi}{12}\right)s_2$$

Where

$$s_1 \in \left[6 \sin\left(\frac{\pi}{12}\right), 6 \sin\left(\frac{\pi}{12}\right) + 2\pi \cos\left(\frac{\pi}{12}\right)\right]$$

$$s_2 \in \left[-2\pi \sin\left(\frac{\pi}{12}\right), 6 \cos\left(\frac{\pi}{12}\right) \right]$$

A design space which includes 342 design points is chosen to construct a well-distributed objective space. This objective space with normalized values consisting of 11 true Pareto points is illustrated in Figure 2.28. Because many design points with different set of process parameters result in same points in objective space, hence, visually the number of design points in the objective space appears to be less than 342.

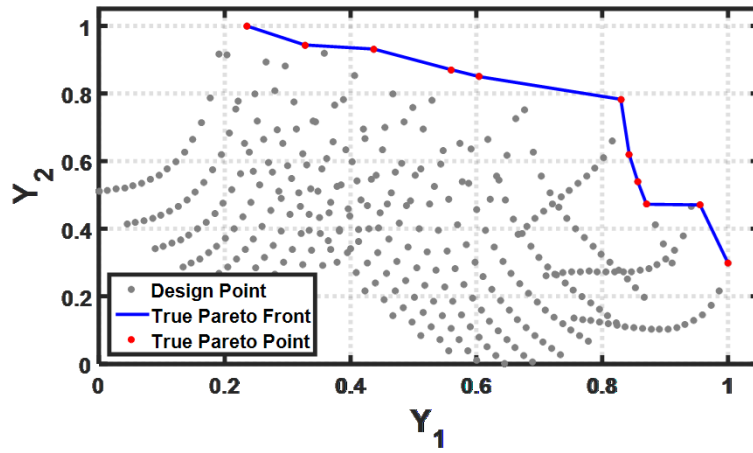


Figure 2.28 Case A—Discretization of objective space for test problem with non-convex Pareto front and well-distributed objective space.

2.12.2.2 Case B: non-convex Pareto front and congested objective space

An equally-spaced discrete design space is selected based on another bi-objective test problem. This is a more challenging case in that the objective space includes very congested points at the middle farther from the Pareto front. This test problem is constructed to test the performance of adaptive-weighted-sum method for solving bi-objective optimization problems [97]. A discretized design space within 441 design points

is chosen. The objective space consists of 19 true Pareto points (Figure 2.29). The functional form of objective functions are as follows:

$$\text{Max } \mathbf{f}(\mathbf{s}) = (Y_1(\mathbf{s}), Y_2(\mathbf{s}))$$

$$Y_1(\mathbf{s}) = 3(1 - s_1)^2 e^{-s_1^2 - (s_2 + 1)^2} - 10 \left(\frac{s_1}{5} - s_1^3 - s_2^5 \right) (e^{-s_1^2 - s_2^2}) - 3e^{-(s_1 + 2)^2 - s_2^2} + 0.5(2s_1 + s_2)$$

$$Y_2(\mathbf{s}) = 3(1 + s_2)^2 e^{-s_2^2 - (1 - s_1)^2} - 10 \left(-\frac{s_2}{5} + s_2^3 + s_1^5 \right) (e^{-s_2^2 - s_1^2}) - 3e^{-(2 - s_2)^2 - s_1^2}$$

where $s_1, s_2 \in [-3, 3]$.

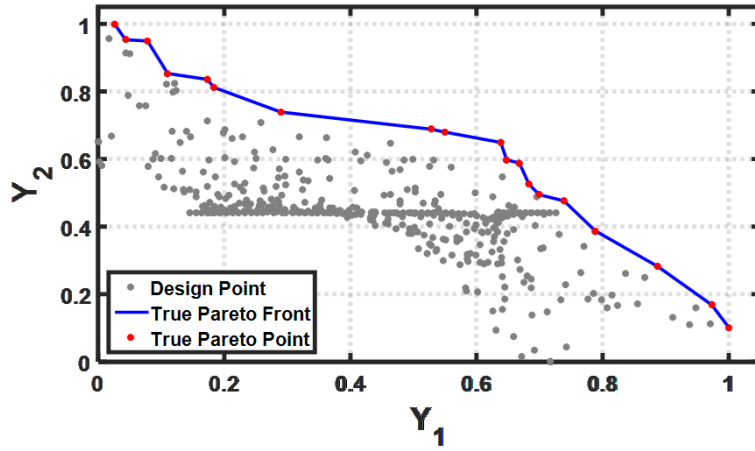


Figure 2.29 Case B—Discretization of objective space for test problem with non-convex Pareto front and congested objective space.

2.12.2.3 Case C: high dimension design space

To test the performance of our methodology in cases with more than two process parameters, we test a bi-objective problem with four process parameters, SK2 [98]. The design space includes 625 design points and the objective space consists of 5 true Pareto

points as illustrated in Figure 2.30. The functional form of objective functions are as follows:

$$\text{Max } \mathbf{f}(\mathbf{s}) = (Y_1(\mathbf{s}), Y_2(\mathbf{s}))$$

$$Y_1(\mathbf{s}) = -(s_1 - 2)^2 - (s_2 + 3)^2 - (s_3 - 5)^2 - (s_4 - 4)^2 + 5$$

$$Y_2(\mathbf{s}) = \frac{\sin s_1 + \sin s_2 + \sin s_3 + \sin s_4}{1 + (s_1^2 + s_2^2 + s_3^2 + s_4^2)/100}$$

where $s_1, s_2, s_3, s_4 \in [-3, 3]$.

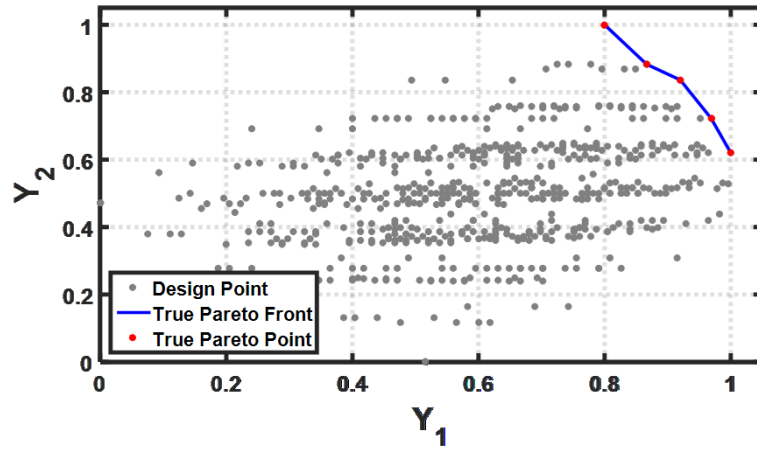


Figure 2.30 Case C—Discretization of objective space for test problem with increased number of process parameters.

2.12.2.4 Simulation results: Pareto front estimation

The performance of the m-APO methodology is compared with full factorial DOE. The estimated Pareto front achieved by each method with 25 experiments is depicted in Figure 2.31—Figure 2.33, overlaid with the true Pareto fronts. We report that, the m-APO method quickly converges towards the true Pareto points much faster than full factorial DOE.

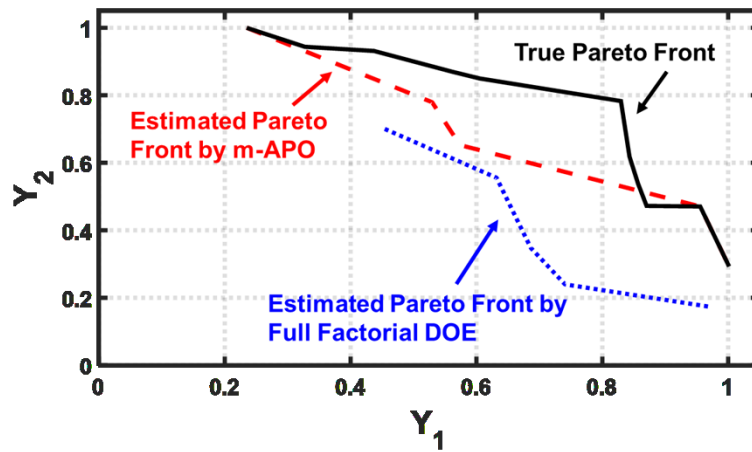


Figure 2.31 Case A—Comparing estimated Pareto front resulted by m-APO and full factorial DOE with true Pareto front (test problem with non-convex Pareto front and well-distributed objective space).

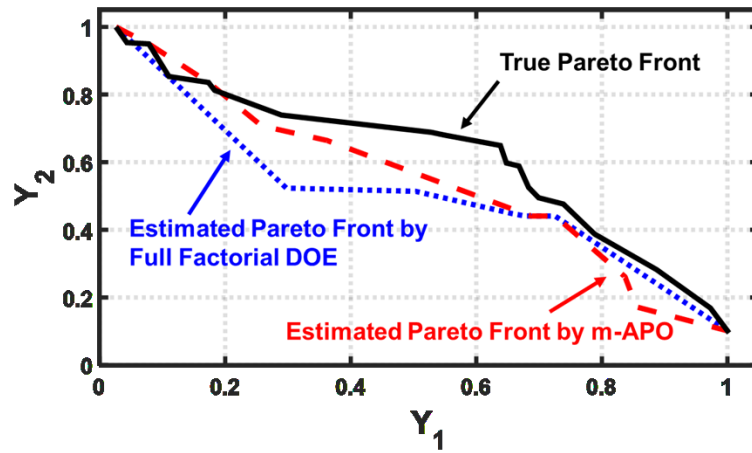


Figure 2.32 Case B—Comparing estimated Pareto front resulted by m-APO and full factorial DOE with true Pareto front (test problem with non-convex Pareto front and congested objective space).

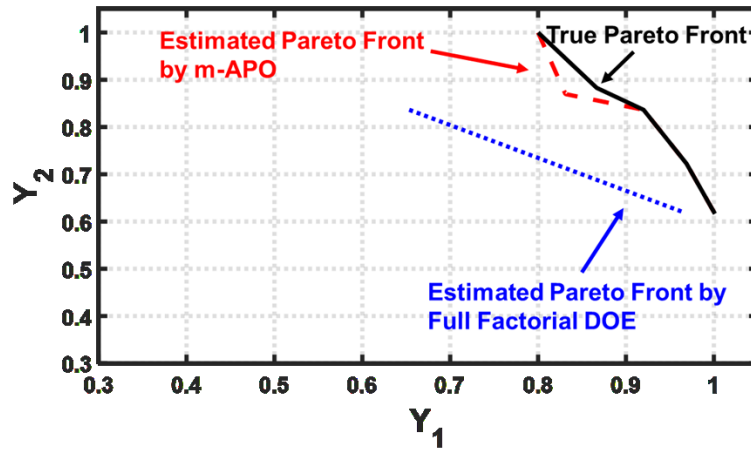


Figure 2.33 Case C—Comparing estimated Pareto front resulted by m-APO and full factorial DOE with true Pareto front (test problem with increased number of process parameters).

Table 2.21 illustrates the improvement in terms of the performance measures (GD,PHV) achieved by applying the m-APO methodology compared with full factorial DOE. Because a smaller GD is preferable to a larger GD, the GD improvement is reported by a negative sing; and since a larger PHV is preferred, an improvement in PHV is reported as a positive number. We observe significant PHV and GD improvement in all cases by applying the m-APO methodology compared with full factorial DOE. It is therefore concluded that the proposed methodology outperforms the full factorial DOE in multi-objective process optimization cases. This is because conventional DOE methods are performed simultaneously—as opposed to the sequential approach developed in this work. Furthermore, this work forwards an approach to balance multiple, and potentially negatively correlated (or uncorrelated) geometric accuracy requirements, while conventional empirical approaches are not capable of this trade-off.

Table 2.21 Improvement achieved in simulation studies by m-APO in terms of decreasing General Distance (GD) and increasing Proportional Hyper-Volume (PHV) for three test problems.

Test Problem Specifications	GD	PHV
Non-convex Pareto front and well-distributed objective space	-55 %	42 %
Non-convex Pareto front and congested objective space	-57 %	24 %
High dimension design space	-93 %	29 %

2.13 Conclusions

This work presented an approach invoking the concept of Multi-objective Accelerated Process Optimization (m-APO) to optimize Additive Manufacturing (AM) process parameters such that parts with least geometric inaccuracy were obtained. The proposed m-APO technique decomposes a multi-objective optimization problem into a series of simpler single-objective optimization problems. The essence of the approach is that, prior knowledge is used to determine the parameter settings for the next trials. This sequential/evolving approach to experimentation has the effect of guiding trials which lead to the process parameter setups resulting in the least geometric inaccuracy more quickly, compared to a priori determined trial parts, as done in conventional design of experiments. In other words, instead of conducting experimental trials in the vicinity of process parameter setups where poor results are more probable, the m-APO methodology suggests experimentation at process parameter setups more inclined to favorable outcomes.

This approach is tested against both experimental datasets obtained from Fused Filament Fabrication (FFF) AM process, and numerically generated data. The specific outcomes are as follows:

The proposed approach was able to effect a tradeoff among geometric accuracy requirements and reached the optimal process parameter settings with 20% fewer trials compared to full factorial experimental plans.

We further tested the performance of the proposed approach to accommodate various simulated cases, such as non-convex Pareto front, well-distributed objective space, congested objective space, and increased number of process parameters. Results indicate that the proposed methodology outperforms full factorial designs for such complex cases. The performance metrics—General Distance (GD) and Proportional Hyper-Volume (PHV)—obtained from the proposed approach significantly superseded full factorial design; there was a 55%-93% and 24%-42% improvement in GD and PHV, respectively, in the simulated test cases.

The results presented in this work are practically important. Given the time-and cost-intensive nature of AM experimental trials, a prudent approach to balance the tradeoff between multiple geometric accuracy requirements is needed in practice. In contrast, this work answers the following research question in the context of AM process optimization: What approach is required to balance between multiple geometric accuracy requirements with the minimal number of experimental trials?

The gap in the current work is that it is demonstrated in the case of non-functional polymer AM parts. The authors are currently researching functional metal AM parts with m-APO as a means for in situ control.

CHAPTER IV

MULTI-OBJECTIVE ACCELERATED PROCESS OPTIMIZATION OF
MECHANICAL PROPERTIES IN LASER-BASED ADDITIVE MANUFACTURING:
CASE STUDY ON SELECTIVE LASER MELTING (SLM) Ti-6Al-4V

2.14 Introduction

2.14.1 Objective and hypothesis

The objective of the present work is to apply a novel framework for efficiently optimizing multiple mechanical properties of metal parts fabricated by Laser-Based Additive Manufacturing (LBAM) systems. Inferior mechanical properties of parts fabricated by LBAM hamper the widespread adoption of this technology and accordingly achieving its full potential for fabricating functional parts in different industries. It is traditionally believed that improving the relative density of LBAM-fabricated parts will result in superior mechanical properties. However, our initial experimental study reveals that obtaining a high relative density for the LBAM-fabricated parts (compared to the traditional counterpart) does not necessarily result in acceptable tensile mechanical properties, such as elongation-to-failure. This phenomenon can be attributed to the existence of different size and distribution of fabrication-induced voids in the final part. The goal of the present work is to employ an efficient multi-objective process optimization framework to optimize quality of LBAM parts with respect to multiple properties such as relative density and elongation-to-failure.

The central hypothesis is that breaking down the master multi-objective problem into an intelligently-defined sequence of scalar combination of objective functions, as a set of sub-problems, can optimize conflicting mechanical properties with the fewest experimental runs. The hypothesis is tested against experimental data on Ti-6Al-4V parts fabricated by Selective Laser Melting (SLM) system. This work leads to a generic multi-objective process optimization framework that can be applied to any LBAM system, with any material, for optimizing any scalar mechanical property.

2.14.2 Motivation

Titanium alloys, among them Ti-6Al-4V, show superior mechanical properties such as high strength, high strength-to-weight ratio, high toughness, ductility, biocompatibility, and high resistance to severe environments. Due to these superior properties these alloys have been employed for several applications in various industries. For instance, titanium alloys, such as Ti-6Al-4V, have been used in biomedical applications since they fulfill the requirements, namely high specific strength, good corrosion and fatigue resistance [101–104]. Moreover, open-cell structures of highly porous metals are recognized very advantageous in orthopedic implants, due to the low modulus of elasticity (adjustable to that of bone) and high volumetric porosity (i.e. low relative density) [105,106]. In the dental prostheses applications, Ti-Ag and Ti-Cu alloys are used—owing to their relatively high strength—in fabricating partial dentures, clasps and bridges [107,108]. Furthermore, titanium alloys are vastly employed in the aerospace industry because of the desired weight-saving property resulted from their high strength-to-weight ratio [109–111]. In addition, in the automotive industry, where light-weight materials with

an acceptable relative density and strength are required, titanium alloys are favorable candidate materials [112,113].

Fabrication of Ti-6Al-4V coupons and parts using Laser-Based Additive Manufacturing (LBAM) techniques has rapidly grown in the past decade, due to their popularity for different applications. One of the main challenges of manufacturing AM metallic alloys is to obtain similar, or even higher, mechanical properties than the conventional alloy. To achieve this, a set of appropriate process parameters, such as laser power, scanning speed, hatch spacing, etc., should be employed during LBAM [1,114]. Therefore, the problem of optimizing process parameters to obtain acceptable mechanical properties, compared to the traditional counterparts, has been addressed by several researchers [1,114–116].

Due to nature of fabrication in LBAM, the manufactured parts are highly prone to formation of microstructural defects, such as voids and pores, which results in lower relative density of the material, as well as significantly reduced mechanical strength [115,117]. For LBAM applications, it is generally believed that maximizing the part density results in the optimal level of mechanical properties (such as elongation-to-failure), which is typically true. Hence, a data-driven methodology using Bayesian theorem was developed to optimize a single mechanical property—such as part’s relative density—called Accelerated Process Optimization (APO) [1]. The APO technique resulted in an average relative density of 99.2% for stainless steel parts fabricated by Selective Laser Melting (SLM) after only five experiments [1]. Nevertheless, further experimental studies revealed that maximizing the relative density of the part, although necessary, might not be sufficient to achieve acceptable mechanical properties. We demonstrate the insufficiency

of considering high relative density of the LBAM product as the only optimization objective by a few examples. For instance, fatigue resistance of specimens fabricated using LBAM techniques, even with very high relative densities, have been reported to be much lower than that for specimens from conventional methods [118,119]. This lower fatigue behavior was attributed to the planar, low-volume voids in the parts that do not affect the density but significantly influence the fatigue resistance [118].

Several factors can potentially cause lower mechanical properties, while having improved relative density, and high cooling rate associated with LBAM is one of them [115,117]. For instance in SLM, high cooling rate can cause low ductility in the final part for metallic powders [36]. Although the high cooling rate during most LBAM processes results in high yield strength, it causes low elongation-to-failure [5].

The shape and distribution of the pores is another significant factor causing the aforementioned conflicting behavior amongst different mechanical properties [118]. For instance, different parts with almost the same relative density can have different pore distribution. This phenomenon is schematically illustrated by Figure 2.34. In Figure 2.34, each gray dot represents a void with the same shape and volume. Although all the five parts have hypothetically same relative density (because of similar number of voids), distribution of the voids changes from one to another. For instance, the part (a) has a very congested distribution of voids at the middle of the gauge section of the part; while the voids are distributed close to the grip ends in part (b). Moreover, in parts (c) and (b) voids are formed very close to the surface of the specimen at the gauge section with different patterns, while those are almost evenly distributed inside the specimens shown in part (e). Other than the pore distribution, pores' shape can significantly contribute to the final parts' mechanical

characteristics, such as tensile properties. In practice, the pores can have very different shapes and volumes. Figure 2.34 (e) represents some microscopic longitudinal pictures of pores within one part. The intent of the presented work is to apply an efficient data-driven experimental plan to achieve the best tradeoff amongst different properties of the final parts, which could indirectly consider the effects of void size and distribution.

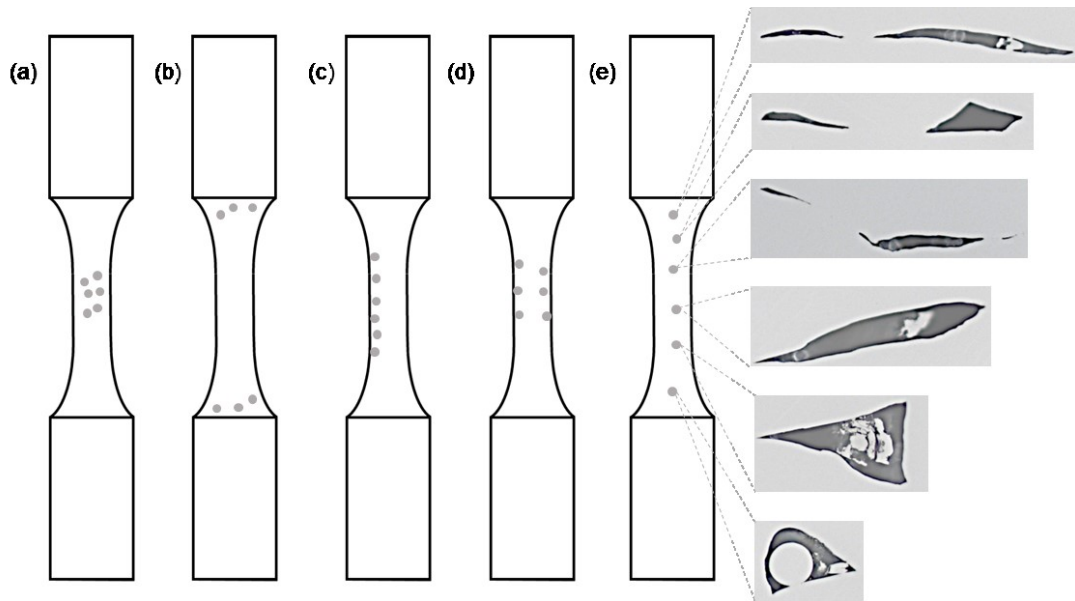


Figure 2.34 Schematic indicating the various possible distribution of voids for samples with similar densities, which may result in different tensile properties.

Figure 2.35 illustrates the contour plots of relative density and elongation-to-failure versus hatch spacing and layer thickness for Ti-6Al-4V parts fabricated by SLM in our initial experimental studies (see Sec. 2.17 for details). From Figure 2.35, it is evident that both relative density and elongation-to-failure for parts made by varying hatch spacing and layer thickness cannot be maximized simultaneously. The combinations of process parameters around the area in the middle right of Figure 2.35 (a) result in maximum relative

density. However, the same process parameter setup results in low elongation-to-failure (area in the middle right of Figure 2.35 (b)). Considering such a coupled variation amongst various mechanical properties, it is extremely challenging to identify the optimal process parameter setup that results in parts with acceptable mechanical properties. Therefore, this work addresses the following challenging research question in LBAM: What experimental plan is required to optimize process parameter setup with respect to multiple mechanical properties of part?

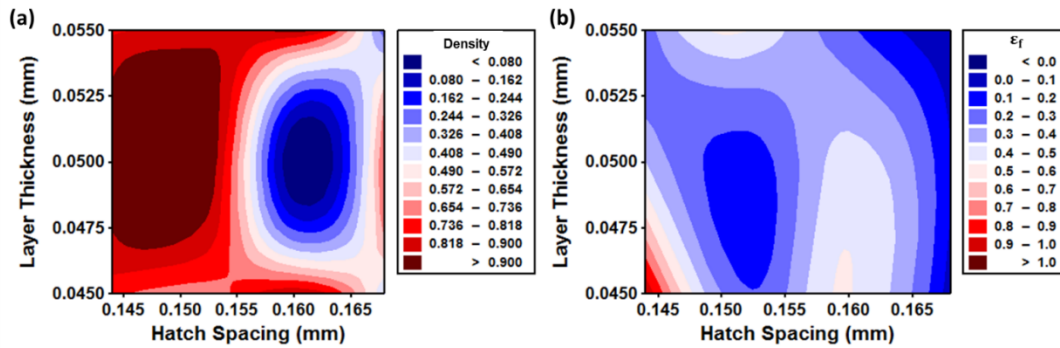


Figure 2.35 Contour plot of (a) part density and (b) part elongation-to-failure (ϵ_f) versus hatch spacing and layer thickness.

Laser power is set to 400w and response values are normalized within [0,1] range.

2.14.3 Research challenges and overview of the proposed approach

As discussed before and shown on Figure 2.36, tensile mechanical response of the AM Ti-6Al-4V is highly sensitive to the selected process parameters, including laser power, scanning speed, hatch spacing and layer thickness. This sensitivity is mainly due to differences in size, shape, location and distribution of fabrication-induced voids, pores, and un-melted regions due to lack of fusion. Consequently, an undesirable amount and distribution of voids can result in very low elongation-to-failure as well as a low failure

stress. On the other hand, a low void volume fraction and un-melted regions that are distributed uniformly can enable a large elongation-to-failure and a high failure stress.

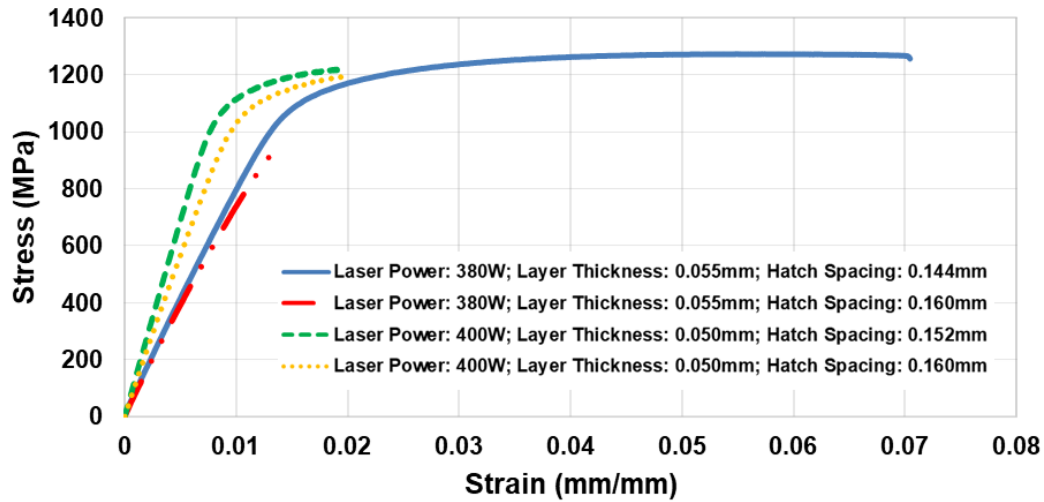


Figure 2.36 Selected stress-strain curves of the different specimens fabricated with different process parameters, indicating the sensitivity of the tensile properties to the process parameters.

Traditionally, maximizing the relative density of the LBAM material was considered as the objective to find the optimized process parameters in a LBAM system [1]. However, for the same relative density, size, shape and distribution of the voids can also dominate the mechanical properties of the LBAM material. Therefore, an extra criterion needs to be considered in optimizing the process parameters to obtain superior mechanical properties. The selected additional criterion in optimizing the process parameters, should be an appropriate representative of the material response. While several mechanical properties—such as modulus of elasticity, ultimate stress, etc.—can be selected, when dealing with one material (as the case of Ti-6Al-4V in this study), elongation-to-failure can be an appropriate candidate for the additional optimization

objective. Employing elongation-to-failure (ϵ_f) is also governed by the stress-strain response of the material, where beyond yield point, a wide range of ϵ_f can be associated with an almost constant stress (see the flat region on the longest stress-strain curve on Figure 2.36). Thus, use of ultimate stress may not be reasonable as knowing this parameter may not provide enough information about the elongation-to-failure. On the other hand, not only ϵ_f implicitly accounts for the value of the material's ultimate stress, it can also demonstrate the toughness of the material. As a result, elongation-to-failure of the material was selected as the additional constraint for the optimization of process parameters in this study.

Although the conventional belief regarding the existence of positive correlation between relative density and part's mechanical properties is correct in general, it may not necessarily hold in the optimal window corresponding to part relative density. This contradictory phenomenon is depicted by Figure 2.37. The plot on the right illustrates the data scatter plot of the scaled relative density and the scaled elongation-to-failure for Ti-6Al-4V parts fabricated by SLM (see Sec. 5.4 for details). The slope of line represents the Pearson correlation coefficient (ρ) between relative density and elongation-to-failure. Although not very significantly, they are positively correlated ($\rho = 0.218$). However, if we look at the optimal window with respect to relative density (i.e., parts with scaled relative density greater than 0.82) we observe a converse phenomenon (The optimal relative density window can be any acceptable relative density depending on the application). The plot on the left illustrates the data scatter plot of the scaled relative density and the scaled elongation-to-failure for parts fabricated within optimal window. It is evident that relative density and elongation-to-failure are negatively correlated ($\rho =$

−0.646). In other words, under the relative density optimal regime, there is no guarantee that improving the part density give rise to higher elongation-to-failure. With this in mind, our problem falls into the scope of multi-objective optimization. However, the existing multi-objective optimization methodologies are not well-suited for optimizing LBAM processes with respect to multiple mechanical properties.

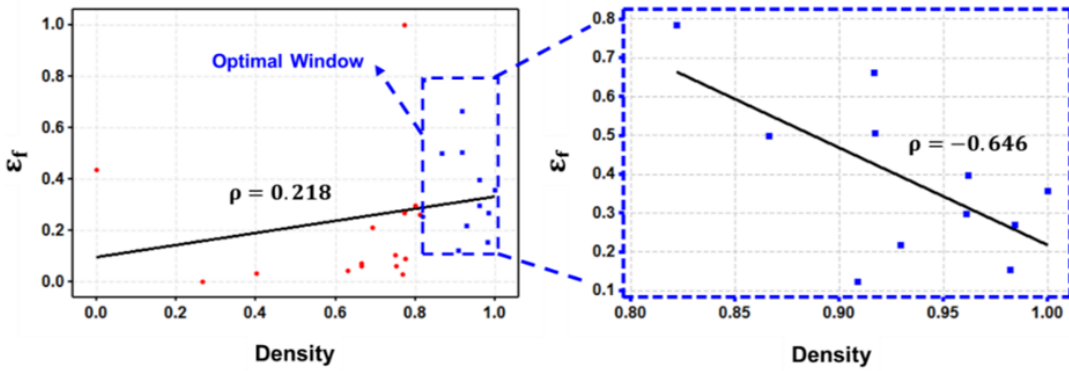


Figure 2.37 The representation of the data scatter plot to illustrate correlation between scaled part relative density and scaled elongation-to-failure.

Data are normalized within $[0,1]$ range. Relative density and elongation-to-failure are positively correlated in general (see the left plot). However, they are negatively correlated in the optimal window corresponding to the relative density (see the right plot).

The existing multi-objective optimization methodologies fall into two major categories: (i) scalarization methods and (ii) evolutionary algorithms [84,120]. Scalarization methods, which are considered as the classical approach in the literature, aggregate multiple objective functions to reduce the multi-objective problem into a scalar or single-objective optimization problem, enabling the employment of single-objective optimization techniques [85,120]. This category of methodologies is not applicable for the current multi-objective mechanical properties optimization problem in LBAM because functional form of objective functions—representing the relationship between process

parameters (e.g., hatch spacing and layer thickness) and objectives of interest (e.g., part density and elongation-to-failure) are unknown. Moreover, constructing the surrogate models representing the mathematical form of objective functions requires a large number of very time-and-cost intensive experimental data, which is not economically feasible for LBAM processes. In contrast to the classical scalarization methods, evolutionary algorithms directly generate a set of Pareto optimal solutions—representing permissible tradeoff between contradictory objective responses—in an iterative manner and gradually improve the quality of the Pareto optimal solutions [86,120–123]. This family of algorithms requires extremely numerous objective function evaluations (i.e., many LBAM experimental runs in the current mechanical properties optimization problem). Hence, we do not apply them to address the current multi-objective process optimization problem since they result in extremely high experimental cost. Hereupon, there is a serious research gap for optimizing multiple mechanical properties of LBAM fabricated parts in an efficient manner. In the present study, we apply a novel multi-objective process optimization framework to intelligently accelerate the process optimization and achieve a set of process parameters resulting in the best compromises between mechanical properties in the optimum regime.

The remainder of this work is organized as follows: In Sec. 2.15, we review the existing literature concerning mechanical properties of parts fabricated by LBAM. In Sec. 2.162.16, we elaborate on the applied multi-objective process optimization approach. In Sec. 2.172.17, the proposed methodology is applied to a real-world case study to optimize mechanical properties of Ti-6Al-4V parts fabricated by SLM. Finally, in Sec. 2.182.18, concluding remarks are provided.

2.15 Background: mechanical properties of laser-based additive manufacturing

Shamsaei et al. [5] conducted a literature review concerning recent advancements in Direct Laser Melting (DLM) systems and asserted that, due to the high cooling rate in DLM, (ultimate) tensile and yield strength of DLM parts are generally as good as those of wrought materials. Nevertheless, for most cases, elongation-to-failure of the DLM parts is lower than that for wrought materials. Non-optimized DLM process along with the associated micro-porosity and oxide inclusions in the parts are found to be the major cause of this phenomenon. Building orientation is another key factor affecting the part's tensile properties. In most cases, building the parts parallel to the loading direction, in tensile specimens, results in lower tensile strength compared to perpendicularly built specimens [5,124]. Different cooling rates resulted from different building orientation may be the reason for the aforementioned anisotropic behavior [5,124].

Selcuk et. al. [125] reviewed and compared mechanical properties of parts fabricated by different LBAM systems. They divided LBAM systems into two major categories: (i) blown powder deposition and (ii) powder-bed deposition. Selcuk et. al. [125] mentioned that mechanical properties of blown powder deposition systems (e.g., Laser Engineered Net Shaping—LENS) are fairly comparable to conventional manufacturing techniques. For instance, yield strength for stainless steel fabricated by LENS system is reported to be almost two times higher than that of conventionally processed material, while the ductility was halved. This different mechanical property between the LENS and wrought stainless steel was attributed to the resulted grain refinement in LENS-fabricated specimens. Almost the same case is reported for titanium- and nickel-based superalloys [125]. As it is mentioned by other papers, build direction is a key parameter affecting

tensile properties of part [124–127]. For instance, yield strength of the stainless steel parts in the perpendicular direction to the build orientation is reported to be considerably lower than the parallel direction, while the opposite is reported for elongation-to-failure [125,126]. Even though anisotropic tensile behavior is a common characteristic of parts fabricated by both powder-bed deposition and blown powder deposition systems, its magnitude varies from material to material. For instance, this phenomenon is considerably greater for stainless steel compared to nickel-based superalloys [125]. Regarding anisotropy tensile behavior in powder-bed deposition systems, Selcuk et al. [125] reported the lowest strength and ductility for the specimens fabricated in vertical direction (applied load was perpendicular to the laser traverse direction). On the other hand, highest strength was observed for the horizontal direction, where the applied load was along the laser traverse direction. Similar to blown powder deposition system, elongation-to-failure for stainless steel parts fabricated by powder-bed deposition system in all directions is reported to be lower than those achieved by conventionally fabricated parts [125].

Carroll et al. [128] studied the effect of build orientation on tensile properties of Ti-6Al-4V parts fabricated by a directed energy deposition (DED) system. Results from their work show that without any post-fabrication treatment and just by modifying the process parameters a larger elongation-to-failure can be achieved for DED Ti-6Al-4V alloys. The modified process parameters in Carroll et al. [128], were adjusted to reduce the amount of lack-of-fusion defects in the fabricated parts. Doing so, the achieved elongations-to-failure were reported to be 11% and 14% for the longitudinal and traverse directions, respectively, which showed significant improvement, compared to previous LBAM Ti-6Al-4V parts. Based on the literature, there has been a lot of research on build orientation effects on

tensile properties of the LBAM material [128,129]. However, to the best of our knowledge, there is no research work on optimizing process parameters to achieve acceptable tensile properties and a high relative density of the AM material.

Wang et al. [130] studied the nucleation and propagation of fatigue cracks in TC18 titanium alloy fabricated by laser melting deposition (LMD) system. They reported that size and location of the fabrication-induced micropores and voids to be the main defects dominating the high-cycle fatigue (HCF) lives of this alloy. As expected, they reported less effect on HCF lives for smaller pores compared with larger ones. Moreover, the effect pores located closer to the surface of the specimen were reported to be more detrimental on the HCF behavior of this alloy. Yadollahi et al. [131] also employed the crack-growth concept and investigated the effects defect properties on the fatigue behavior of Inconel 718 alloy, fabricated by L-PBF method. Their study also indicated the defect (i.e. void) size to be the most influential defect feature on the fatigue life of AM Inconel 718. Therefore, employing a set of process parameters that result in no or very small voids in the fabricated parts is desired for durable LBAM materials.

There are some works related to advance welding systems tried to predict and optimize the ultimate tensile strength of joints using conventional design of experiments (DOE) methods. Although welding processes may not fall into the category of LBAM processes; due to the layered nature of welding processes, results from such a study can potentially help to understand the appropriate criteria for optimizing the process parameter of AM process for favorable tensile behavior. Silva et al. [132] applied Taguchi orthogonal arrays to optimize ultimate tensile strength of aluminum alloy joints. Two different orthogonal arrays (i.e., $L_8(2^7)$ and $L_{27}(3^{13})$) were applied considering three different joint

configurations (i.e., butt, T and double-pass overlap joints). Bozkurt [133] used $L_{27}(3^{13})$ Taguchi orthogonal arrays to maximize tensile strength of polyethylene sheets processed by friction stir welding process. Ampaiboon et al. [134] applied fractional factorial (2^{6-2}) design with two replication to optimize ultimate tensile strength of mild steel (ST37-2) joints welded by Metal Active Gas system. Same DOE procedures can be applied to optimize tensile strength of AM parts; however, they result in many expensive LBAM experimental trials. Furthermore, they cannot directly handle optimizing multiple uncorrelated properties. Therefore, a novel multi-objective DOE is employed in this study, which requires significantly less number of experiments and specimen fabrication using LBAM.

2.16 Methodology

2.16.1 Multi-objective process optimization

This section is dedicated to presenting an overview of the Multi-Objective Accelerated Process Optimization (m-APO) methodology applied in the present work. The m-APO is a generalization of an existing Accelerated Process Optimization (APO) method, which is able to facilitate the optimization of AM systems with respect to one objective (e.g., one mechanical property of parts such as relative density) by characterizing and leveraging the similarities amongst the current and non-identical prior studies [1]. The APO is able to significantly reduce the number of experimental runs while achieving a targeted optimum value. In the authors' previous research work, the APO is applied to maximize the relative density of stainless steel test coupons fabricated by SLM system [1].

The m-APO applied in the present work is primarily developed to minimize the geometric inaccuracy of the AM parts [93,94,135]. In principal, the m-APO is developed

and illustrated in the form of bi-objective process optimization; however, it can readily be extended to multi-objective cases. In the present study, we apply m-APO to maximize relative density and elongation-to-failure of Ti-6Al-4V tensile samples fabricated by SLM system.

2.16.1.1 Multi-objective process optimization and Pareto front

Assume that the goal is to maximize two response variables Y_1 and Y_2 which are not significantly positively correlated (e.g. part relative density and elongation-to-failure). The bi-objective maximization problem is demonstrated as follows:

$$\begin{aligned} \text{Max } \mathbf{Y}(\mathbf{s}) &= (Y_1(\mathbf{s}), Y_2(\mathbf{s}))' \\ \text{s. t. } &\mathbf{s} \in \mathbf{S} \end{aligned} \quad (5.1)$$

$\mathbf{Y}(\mathbf{s})$ denotes the vector of objective functions $(Y_1(\mathbf{s}), Y_2(\mathbf{s}))'$, and \mathbf{s} is the vector of process parameters (e.g., layer thickness, laser power and hatch spacing). \mathbf{S} denotes the design space consisted of all possible combinations of process parameters' values, i.e., \mathbf{s} . Moreover, $\mathbf{C} = \{(Y_1(\mathbf{s}), Y_2(\mathbf{s}))' \in \mathbb{R}^2: \mathbf{s} \in \mathbf{S}\}$ denotes the objective space, i.e., the set of all possible combinations of response vectors \mathbf{Y} corresponding to the design space.

Due to the very complex underlying thermo-mechanical process associated with melt-pool formation and solidification in LBAM, for most cases, the mathematical expression of $Y_1(\mathbf{s})$ and $Y_2(\mathbf{s})$ representing the functional relationship between the process parameters (i.e., \mathbf{s}) and the mechanical properties of parts (i.e., Y_1 and Y_2) is not well-identified and formulated as yet. In other words, the analytical formula corresponding to the objective functions are unknown. Furthermore, statistical speaking, the correlation

between $Y_1(\mathbf{s})$ and $Y_2(\mathbf{s})$ is also unknown *a priori*. Improving the value of $Y_1(\mathbf{s})$ may consequently lead to worsening the value of $Y_2(\mathbf{s})$ or vice versa. In practice, due to the potential low or even negative correlation between Y_1 and Y_2 , it may not be possible to optimize them using the same process parameter setup. For instance, in the presented optimal window—shown in Figure 2.37—there is a negative Pearson correlation between part relative density and elongation-to-failure, i.e., $\rho = -0.646$. Therefore, improving the part relative density will not guarantee improving the elongation-to-failure of parts. With this in mind, there is no unique set of process parameters as the optimal solution to the presented bi-objective process optimization problem. The ultimate goal of the presented research is to develop and apply a methodical and optimization-oriented DOE procedure capable of efficiently achieve a set of optimal process parameter setups resulting in the best tradeoff between such contradictory mechanical properties in the parts.

Inspired by the scalarization idea, m-APO convert the master bi-objective process optimization problem into a series of single objective optimization sub-problems via multiplying each objective function by a weight coefficient. Therefore, the decomposed bi-objective maximization problem can be formulated as follows:

$$\text{Max } Z^h(\mathbf{s}) = \gamma_1^h \cdot Y_1(\mathbf{s}) + \gamma_2^h \cdot Y_2(\mathbf{s}) \quad (5.2)$$

$$\text{s. t. } \mathbf{s} \in \mathbf{S}$$

$$\text{where } \gamma_1^h + \gamma_2^h = 1$$

$$\gamma_k^h \geq 0, \quad \forall k = 1, 2$$

γ_k^h denotes weight coefficient corresponding to the k^{th} objective function within the h^{th} sub-problem. Different combinations of weight coefficients, satisfying the constant

$\gamma_1^h + \gamma_2^h = 1$, corresponds to different sub-problems and accordingly different search directions on the objective space.

For instance, weight coefficients $\gamma_1^3 = 0.7$ and $\gamma_2^3 = 0.3$ correspond to a sub-problem with the objective function in the form of $\text{Max } Z^3(\mathbf{s}) = (0.7Y_1(\mathbf{s}) + 0.3Y_2(\mathbf{s}))$.

The weight coefficients (γ_k^h) represented by the tangent of the maximization objective function line in Figure 2.38 denotes the desired search direction for the 3th sub-problem.

Another combination of weight coefficients, such as $\gamma_1^4 = 0.3$ and $\gamma_2^4 = 0.7$, corresponds to a distinct sub-problem with different objective function and search direction, i.e.,

$\text{Max } Z^4(\mathbf{s}) = (0.3Y_1(\mathbf{s}) + 0.7Y_2(\mathbf{s}))$ in Figure 2.38.

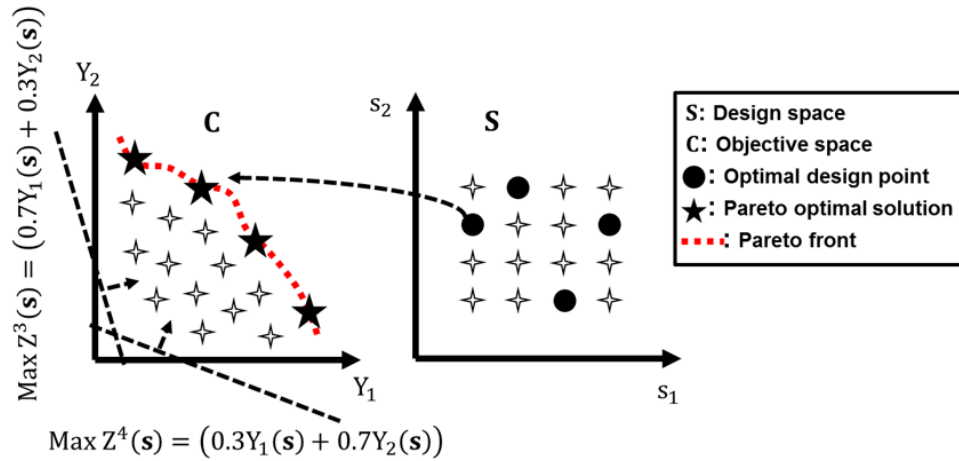


Figure 2.38 Schematic illustration of design space, objective space, optimal design point, Pareto optimal solution and Pareto front [135,136].

Likewise, different combinations of weight coefficients lead to entirely distinct shapes of contour plot for the weighted summation of part relative density and elongation-to-failure generated by our initial experimental data. For instance, Figure 2.39 illustrates two contour plots corresponding to different combinations of weight coefficients for our

initial experimental data; i.e., $(\gamma_1^1 = 1, \gamma_2^1 = 0)$ and $(\gamma_1^4 = 0.3, \gamma_2^4 = 0.7)$. It is visually noticeable that there is not a unique combination of hatch spacing and layer thickness maximizing both contour plots' response values. This statement is more supported by the research challenges regarding the negative or weak positive correlation amongst various mechanical properties of LBAM parts discussed in Sec.2.14.3. With this in mind, we also conclude that it is not possible to optimize infinite number of sub-problems by a unique set of process parameters. Therefore, in such problems, the optimum solution is a subset of objective space \mathbf{C} representing the best compromises amongst the values of conflicting objective responses, i.e., Y_1 and Y_2 .

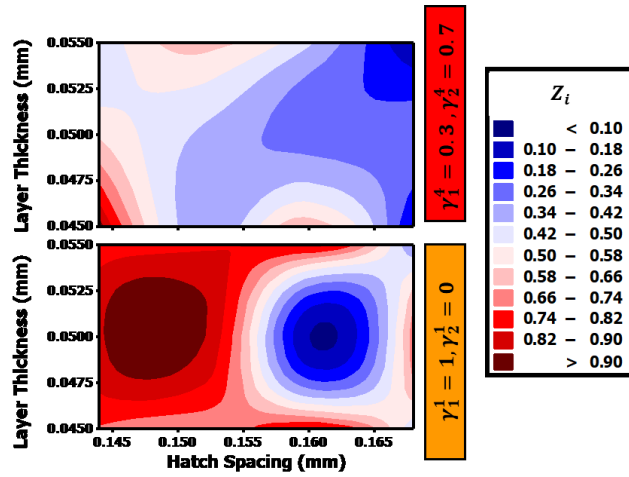


Figure 2.39 Different combinations of weight coefficients lead to distinct shapes of contour plot for the weighted summation of part relative density and elongation-to-failure.

The m-APO methodology is developed to systematically and efficiently identify the Pareto optimal solutions associated with the multi-objective optimization problem. A Pareto optimal solution $(Y_1(\mathbf{s}^*), Y_2(\mathbf{s}^*))$ is a non-dominated solution on the objective space

representing one of the best feasible compromises amongst the objective functions' values. A design point $\mathbf{s}^* \in \mathbf{S}$ corresponding to a Pareto optimal solution is called an optimal design point if and only if there is no other $\mathbf{s} \in \mathbf{S}$ such that $Y_k(\mathbf{s}) \geq Y_k(\mathbf{s}^*)$ for $k = 1, 2$. With respect to our mechanical properties optimization problem, a Pareto optimal solution corresponds to a design point where there is no other one resulting in higher value of both part relative density and elongation-to-failure. The set of Pareto optimal solutions is called Pareto front. The concept of design space, objective space, Pareto optimal solution and Pareto front are illustrated by Figure 2.38 given two process parameters for the bi-objective optimization problem presented by Eq. (5.2).

2.16.1.2 An overview of Multi-objective Accelerated Process Optimization (m-APO)

The Multi-Objective Accelerated Process Optimization (m-APO) methodology is targeted at achieving a well-distributed set of Pareto optimal solutions in order to efficiently approximate the Pareto front with very limited number of experiments. As opposed to conventional scalarization-based optimization approaches which individually solve the single-objective sub-problems, m-APO identifies and leverages the similarities amongst different sub-problems to eventually accelerate the multi-objective optimization procedure.

The Accelerated Process Optimization (APO), which is able to deal with single objective process optimization cases, is embedded in the proposed m-APO framework to jointly solve the constructed sub-problems. APO leverages the experimental data from prior similar—but non-identical—processes to accelerate the optimization procedure in the current process [1]. The same idea is incorporated within m-APO by treating the

experimental data from previous sub-problems as prior data for optimizing the current sub-problem at each stage.

After identifying the existing Pareto optimal solutions on the objective space at each step, m-APO intelligently constructs the best next sub-problem which has the most potential to efficiently improve the approximation of the Pareto front. Consequently, a large number of experimental runs will be saved by smartly selecting only a few sub-problems to solve amongst an infinite number of them.

Moreover, in lieu of independently and separately designing experiments for optimizing each sub-problem, experimental data obtained from previous sub-problems are utilized as prior data in the APO framework to accelerate optimization process for the next sub-problems. Figure 2.40 demonstrates an illustrative example of applying the m-APO approach to maximize parts' relative density and elongation-to-failure based on our initial experimental data. For example, in Figure 2.40 experimental data from sub-problem 1 (represented by segments a-b-c) facilitates the optimization procedure for sub-problem 2. Hence, the algorithm can achieve the Pareto optimal solution corresponding to the sub-problem 2 (i.e., segment e) with fewer experimental trials. Similarly, the information captured by experimental data obtained from sub-problems 1, 2 and 3 (represented by segments a-b-c, d-e and f-g respectively) contribute to achieving the Pareto optimal solution corresponding to sub-problem 4 (i.e., segment h) by conducting only one experiment. m-APO leverages the prior experimental data in order to avoid individually designing the experiments for each sub-problem from scratch.

The m-APO continues this procedure till the improvement in the resulting Pareto front approximation is not significant. The magnitude of dominated area on the objective space is used to evaluate the efficiency of the resulting Pareto optimal solutions. The m-APO algorithm is described in detail in the Appendix G.

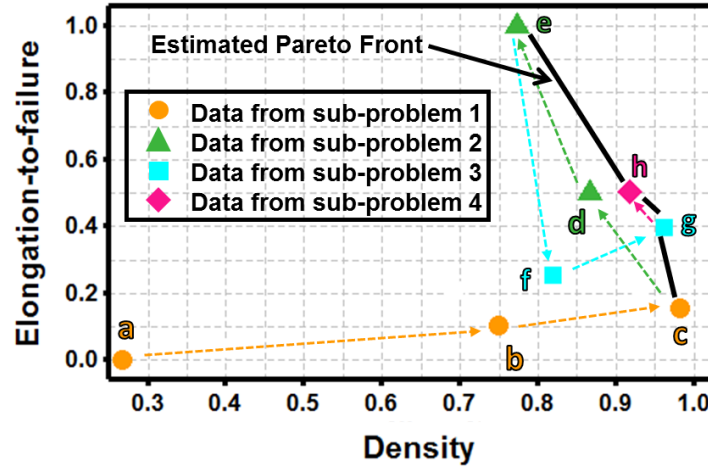


Figure 2.40 The m-APO leverages experimental data obtained from prior sub-problems to accelerate solving the subsequent sub-problems.

Response values are scaled within $[0,1]$ range.

2.17 Experimental case study and discussion: mechanical properties optimization of Ti-6Al-4V parts fabricated by Selective Laser Melting (SLM)

Now we apply the m-APO to a real-world case study to maximize the relative density and elongation-to-failure of Ti-6Al-4V parts fabricated by SLM. Note that m-APO can be applied to optimize any conflicting couple of scalar mechanical properties for any LBAM-fabricated part with any material. The efficiency of m-APO is tested via a series of extensive simulation studies in the authors' previous studies [93,94,135,136]. Its robustness is also validated against test problems with different number of input process

parameters and characteristics of objective space and Pareto fronts (including convex and non-convex Pareto fronts) [93,94,135,136]. Hence, in the present study we only present a real-world case study and benchmark the results against full factorial DOE. The results show that m-APO outperforms an extended full factorial DOE by 51.8% in terms of achieving the true Pareto front with fewer experimental runs.

2.17.1 Experimental data generation: fabrication and test procedures

Spherical gas atomized Grade 23 Ti-6Al-4V (ASTM B348 - 13 [137]) powder was used in an argon-purged AM machine (Renishaw AM250) to fabricate the specimens. Chemical composition of the powder is reported in Table 2.22. Various combinations of process parameters were used in this study — mainly by varying the laser power, hatch spacing, and layer thickness—to fabricate the rods (see Sec 2.17.2). Four rods were fabricated by using each set of process parameters at a time. All the rods were fabricated in the vertical direction and the scanning path was the same for all the fabricated rods.

Table 2.22 Chemical composition of powder used to fabricate the Ti-6Al-4V specimens.

Element	Al	C	Fe	H	N	O	Ti	V	Others
Weight percent (%)	6.4	0.01	0.021	0.0029	0.02	0.11	Balance	4.1	<0.4

Ti-6Al-4V rods of 7 mm diameter were fabricated using SLM machine on a Ti-6Al-4V build plate. After separation from the build plate, the fabricated bars were machined to a solid circular shape with straight gauge section of 3.6 mm diameter for tensile testing [138]. Before tensile testing, relative density of bars was measured and reported, considering Ti-6Al-4V wrought material density as the reference.

Geometry of the tensile specimens were designed according to the specifications of ASTM E-8 standard [138] and is indicated in Figure 2.41. Gauge section of the specimen was mechanically polished using SiC sand-paper to minimize the effects of surface condition on the mechanical response. Monotonic tensile tests were conducted in strain-controlled condition using an MTS 810 servo-hydraulic testing machine at a strain rate of 10^{-3} s^{-1} . Elongation-to-failure and stress values such as ultimate and yield stress (if observable) were collected from tensile tests to be used for optimizing the process parameters.

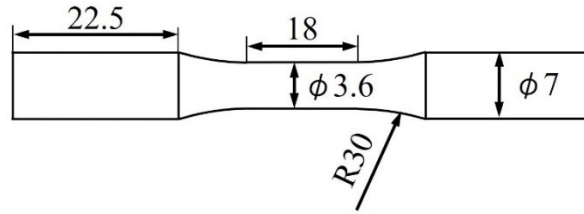


Figure 2.41 Schematic showing the dimensions of the specimen used in monotonic tensile tests (all dimensions are in mm).

2.17.2 Initial design of experiments setups and data generation

We applied full factorial DOE plans to generate experimental data forming our targeted design and objective spaces. Initially we designed a $2 \times 3^2 (= 18)$ full factorial DOE (see Table 2.23). The design space is originally centered on the process parameters setup recommended by SLM manufacturer for Ti-6Al-4V. The increment for process parameters' levels are selected based on the LBAM system sensitivity to the process parameters and the availability of resources. After conducting and testing some experiments we observed that parts with the largest hatch spacing (i.e., 0.168 mm) are

extremely prone to low elongation-to-failure as well as low failure stress. Hence, after making conducting and testing 3 sets of experiments with 0.168 mm hatch spacing, we replaced the hatch spacing of 0.168 mm with 0.144 mm for the rest of the experiments (see Table 2.24).

Table 2.23 Levels of the process parameters applied in the initial full factorial DOE plan.

Laser power (W)	380		400
Layer thickness (mm)	0.045	0.050	0.055
Hatch spacing (mm)	0.152	0.160	0.168 (replaced with 0.144)

After conducting and testing some experiments hatch spacing of 0.168 mm is replaced with 0.144 mm.

Moreover, to focus on the effect of laser power, we designed a $1 \times 3 \times 2 (= 6)$ full factorial DOE plan—as an auxiliary design—including the laser power at the level of 390W (see Table 2.24). Eventually, we conducted 27 sets of experiments each with 3 replications to generate a design and objective space.

Table 2.24 Levels of the process parameters applied in the auxiliary full factorial DOE plan to narrow down to the effect of laser power.

Laser power (W)	390		
Layer thickness (mm)	0.045	0.050	0.055
Hatch spacing (mm)	0.152	0.160	

2.17.3 Apply Multi-objective Accelerated Process Optimization (m-APO)

This section applies the m-APO to efficiently maximize the relative density and elongation-to-failure of parts. The extended full factorial DOE plan presented in Sec. 2.17.2 results in a design and objective space with size of 27 including 6 Pareto optimal solutions (cross circles in Figure 2.42). Starting from a random design point, we iteratively

apply m-APO. We stop the optimization process at the 13th experiment because we achieved the same 6 Pareto optimal solutions at this stage. Therefore, employing m-APO we attain the true Pareto front while saving 14 experimental runs, which means 51.8% experimental runs compared with our initial extended full factorial design.

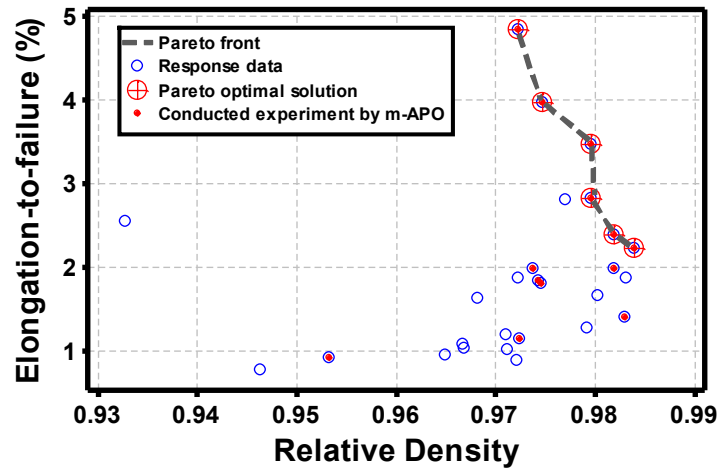


Figure 2.42 Demonstrating the objective space, Pareto optimal solutions and conducted experiments by m-APO.

Process parameter setups associated with the Pareto optimal solutions—along with the corresponding relative density, elongation-to-failure and ultimate strength—are presented in Table 2.25. In fact, we efficiently identified a set of process parameters resulting in the best compromises in terms of the relative density and tensile properties of parts while significantly reducing the number of required experimental runs. As can be seen in Figure 2.42, there are many specimens—fabricated with different process parameters—that yield in a high relative density. However, the corresponding elongation-to-failure for those specimens is very low (see the data with relative density > 0.97 and elongation-to-failure

< 2). The small elongation-to-failure for these specimens may be explained by the distribution of the void, as previously depicted in Figure 2.34. In other words, for those specimens with high relative density, although there exists lower amount of fabrication-induced voids, these voids may have been huddled in some locations of the gauge section, resulting to a weak point on the gauge section and, subsequently, very small elongation-to-failure. Another reason, for these observations, could be the presence of the small-volume flat voids (i.e. un-melted regions) due to the lack-of-fusion for some cases. Presence of un-melted regions in the LBAM specimens does not influence the relative density of the part, while resulting in a weak section along the specimen's length and, thus, premature failure of the corresponding specimens. That being said, the multi-objective accelerated process optimization (m-APO) employed in this study, can implicitly account for the effects of void type and distribution. As a result, it can efficiently achieve sets of process parameter setups— corresponding to the Pareto front of Figure 2.42— that not only fabricate parts with high relative density, but also with an acceptable elongation-to-failure.

Table 2.25 Optimal process parameters and the corresponding, relative density, elongation-to-failure and ultimate stress.

Laser power (W)	Layer thickness (mm)	Hatch spacing (mm)	Relative density	ϵ_f (%)	σ_u(MPa)
380	0.05	0.144	0.9839	2.22	1198.43
400	0.05	0.144	0.9819	2.38	1226.97
400	0.045	0.144	0.9722	4.84	1243.97
380	0.045	0.144	0.9796	3.47	1224.40
400	0.045	0.16	0.9797	2.82	1199.15
380	0.055	0.144	0.9748	3.97	1250.57

2.18 Conclusions

The present work proposed a novel approach to efficiently optimize different mechanical properties of LBAM-fabricated parts. The experimental data show that parts within an acceptable range of relative density possess very different magnitude of tensile mechanical properties (such as elongation-to-failure). In other words, different mechanical properties demonstrate nearly conflicting behavior in the optimal density window. The variation in the tensile mechanical properties of the specimens with almost similar relative density, although fabricated with different process parameters, could be attributed to the size and distribution of the fabrication-induced voids along the volume of the specimen (see Figure 2.34). The proposed multi-objective accelerated process optimization (m-APO) methodology is able to achieve a set of process parameter setups resulting in the best trade-off between conflicting mechanical properties of parts in the optimal regime (such as relative density and elongation-to-failure in Figure 2.37).

The m-APO methodology separates the master multi-objective problem into a sequence of single-objective sub-problems and intelligently solves the sub-problems with the highest chance to achieve the Pareto optimal solution, representing the best compromise between conflicting mechanical properties. At each stage, m-APO method leverages the experimental data generated from previous sub-problems to accelerate the optimization procedure of the remaining sub-problems.

The m-APO is applied to a real-world case study aimed at maximizing relative density and elongation-to-failure of Ti-6Al-4V parts fabricated by SLM system. m-APO method was able to achieve the optimal process parameter setups while reducing the experimental runs by 51.8% compared to an initial extended full factorial DOE. m-APO

method, which results in not only a high density, but also a satisfactory level of elongation-to-failure—as employed in this study—indirectly accounts for the effect of size and distribution of the voids on different mechanical properties of the fabricated parts.

CHAPTER V

CONCLUSIONS

The optimization of Additive Manufacturing (AM) processes with respect to desired part quality is essential to enhance the trustworthiness of this emerging technology and facilitate its commercial viability. In the present dissertation we developed knowledge-guided experimental frameworks that can efficiently optimize AM-fabricated parts with respect to various characteristics, namely geometric accuracy and mechanical properties. The proposed approaches are able to leverage the information from existing prior experiments and systematically characterize the relation between process parameters and part features so that the AM process can be optimized in a very efficient manner.

First a novel sequential methodology, called Accelerated Process Optimization (APO), is presented for systematically optimizing controllable process parameters in AM processes. The APO is developed on the premise that—despite differences in experimental conditions, material properties, system capacity, etc.—studies pertaining to various AM processes share similarities and thus the mechanical properties of AM-fabricated parts may be correlated. The APO method characterizes and quantifies these similarities by a random variable; that is, DRPCS. Using the Bayesian theory, to efficiently utilize data from similar—but non-identical—prior studies for accelerating the process optimization in the current study, we developed a closed-form expression that updates the statistical distribution of DRPCS terms. Hence, prior data are directly used as initial experiments and

eventually facilitate achieving a targeted optimum while reducing the experimental runs required. The performance of APO is evaluated using a series of simulation studies that used an empirical relative density model including four Laser-Based Additive Manufacturing (LBAM) process parameters; i.e., laser power, laser velocity, hatch spacing, and layer thickness. The performance of APO is assessed by the number of experimental runs needed to achieve a targeted level of relative density. The robustness of APO is tested against different characteristics of DRPCS. The APO significantly outperformed two benchmark methodologies; full factorial design, which does not account for the optimization objective, and Sequential Minimum Energy Design (SMED), which does not utilize prior data.

To further verify the superiority of the APO, we applied that to a real-world case study that aimed at optimizing the relative part density of PH 17-4 SS parts fabricated by a Selective Laser Melting (SLM) system. The optimized process parameters obtained from prior studies could not be directly applied due to difference scales of LBAM systems and various experimental conditions. The APO utilized these prior data and could achieve the optimal process parameters in the current study after only five experimental runs. Note that the APO methodology provides a generic framework for better understanding the similarities among AM systems and the correlation of parts' properties. It is not limited to any specific type of AM system, material or part property.

Also, there is a need to optimize multiple mechanical properties, which may be conflicting. Multi-objective optimization remains an open area, and more research efforts are needed to develop an efficient and effective optimization scheme.

This challenge of AM process optimization is further compounded when some of the parts' characteristics show conflicting behaviors. In other words, some characteristics of parts are negatively correlated; that is, improving one of the parts' properties results in worsening some of the others.

With this in mind, in a subsequent work, we presented an approach invoking the concept of Multi-objective Accelerated Process Optimization (m-APO). The proposed m-APO was initially targeted at minimizing the deviation in conflicting geometric characteristics of AM-fabricated parts. The m-APO methodology decomposes a master multi-objective optimization problem into a sequence of single-objective optimization sub-problems. The m-APO leverages the information captured from the experimental runs in the previous sub-problems to accelerate the experimentation procedure in the remaining sub-problems. Hence, the m-APO can efficiently achieve a set of process parameters setups resulting in the best trade-off between conflicting geometric characteristics of AM-fabricated parts. The m-APO method is tested against both experimental datasets obtained from Fused Filament Fabrication (FFF) AM process, and numerically generated data. The m-APO achieved the optimal process parameter settings with 20% fewer trials compared to full factorial experimental plans. The robustness of the m-APO is further assessed by conducting various simulation cases including non-convex Pareto front, well-distributed objective space, congested objective space, and increased number of process parameters. The performance metrics—General Distance (GD) and Proportional Hyper-Volume (PHV)—obtained from the m-APO methodology significantly superseded full factorial design as the benchmark method; there was a 55%-93% and 24%-42% improvement in GD and PHV, respectively, in the simulated test cases.

According to our initial experimental studies, parts within an acceptable range of relative density possess very different magnitude of tensile mechanical properties (such as elongation-to-failure). In other words, they are negatively correlated in the optimal relative density window. The variation in the tensile mechanical properties of the specimens with almost similar relative density, although fabricated with different process parameters, could be attributed to the size and distribution of the fabrication-induced voids along the volume of the specimen. Simultaneously optimizing such mechanical properties is impossible due to the negative correlation between them. In a subsequent research work, the m-APO methodology is applied to efficiently optimize different conflicting mechanical properties of LBAM-fabricated parts. The m-APO method is able to obtain a set of process parameter setups resulting in the best compromises between conflicting mechanical properties of parts in the optimal regime (such as relative density and elongation-to-failure). We applied m-APO to a real-world case study aimed at maximizing relative density and elongation-to-failure of Ti-6Al-4V parts fabricated by SLM system. The m-APO method was able to achieve the optimal process parameter setups while reducing the experimental runs by 51.8% compared to an initial extended full factorial DOE. The m-APO method, indirectly accounts for the effect of size and distribution of the voids on different mechanical properties of the fabricated parts.

To further understand and characterize the effect of process parameters on the mechanical properties of LBAM-fabricated parts, more research work is needed to model the formation of voids during the build and predict the void size and distribution within the final parts.

REFERENCES

- [1] Aboutaleb, A. M., Bian, L., Elwany, A., Shamsaei, N., Thompson, S. M., and Tapia, G., 2016, “Accelerated Process Optimization for Laser-Based Additive Manufacturing by Leveraging Similar Prior Studies,” *IIE Transactions*, **49**(1), pp. 1–14.
- [2] Badiru, A. B., Valencia, V. V., and Liu, D., *Additive Manufacturing Handbook : Product Development for the Defense Industry*.
- [3] Emelogu, A., Marufuzzaman, M., Thompson, S. M., Shamsaei, N., and Bian, L., 2016, “Additive Manufacturing of Biomedical Implants: A Feasibility Assessment via Supply-Chain Cost Analysis,” *Additive Manufacturing*, **11**, pp. 97–113.
- [4] Tapia, G., and Elwany, A., 2014, “A Review on Process Monitoring and Control in Metal-Based Additive Manufacturing,” *Journal of Manufacturing Science and Engineering*, **136**(6), p. 60801.
- [5] Shamsaei, N., Yadollahi, A., Bian, L., and Thompson, S. M., 2015, “An Overview of Direct Laser Deposition for Additive Manufacturing; Part II: Mechanical Behavior, Process Parameter Optimization and Control,” *Additive Manufacturing*, **8**, pp. 12–35.
- [6] M.S. Tootooni, 2016, “Sensor Based Monitoring of Multidimensional Complex Systems Using Spectral Graph Theory,” Binghamton University.
- [7] Rao, P. K., Kong, Z., Duty, C. E., Smith, R. J., Kunc, V., and Love, L. J., 2015, “Assessment of Dimensional Integrity and Spatial Defect Localization in Additive Manufacturing Using Spectral Graph Theory,” *Journal of Manufacturing Science and Engineering*, **138**(5), p. 51007.
- [8] Huang, Q., Zhang, J., Sabbaghi, A., and Dasgupta, T., 2015, “Optimal Offline Compensation of Shape Shrinkage for Three-Dimensional Printing Processes,” *IIE Transactions*, **47**(5), pp. 431–441.
- [9] Huang, Q., 2016, “An Analytical Foundation for Optimal Compensation of Three-Dimensional Shape Deformation in Additive Manufacturing,” *Journal of Manufacturing Science and Engineering*, **138**(6), p. 61010.

- [10] Huang, Q., Nouri, H., Xu, K., Chen, Y., Sosina, S., and Dasgupta, T., 2014, "Statistical Predictive Modeling and Compensation of Geometric Deviations of Three-Dimensional Printed Products," *Journal of Manufacturing Science and Engineering*, **136**(6), p. 61008.
- [11] Thompson, S. M., Bian, L., Shamsaei, N., and Yadollahi, A., 2015, "An Overview of Direct Laser Deposition for Additive Manufacturing; Part I: Transport Phenomena, Modeling and Diagnostics," *Additive Manufacturing*, **8**, pp. 36–62.
- [12] Yu, J., Lin, X., Ma, L., Wang, J., Fu, X., Chen, J., and Huang, W., 2011, "Influence of Laser Deposition Patterns on Part Distortion, Interior Quality and Mechanical Properties by Laser Solid Forming (LSF)," *Materials Science and Engineering: A*, **528**(3), pp. 1094–1104.
- [13] Kahlen, F.-J., and Kar, A., 2001, "Tensile Strengths for Laser-Fabricated Parts and Similarity Parameters for Rapid Manufacturing," *Journal of Manufacturing Science and Engineering*, **123**(1), p. 38.
- [14] Birnbaum, A., Aggarangsi, P., and Beuth, J., 2003, "Process Scaling and Transient Melt Pool Size Control in Laser-Based Additive Manufacturing Processes," *Proceedings of the Annual International Solid Freeform Fabrication Symposium*.
- [15] Bontha, S., Klingbeil, N. W., Kobryn, P. A., and Fraser, H. L., 2009, "Effects of Process Variables and Size-Scale on Solidification Microstructure in Beam-Based Fabrication of Bulky 3D Structures," *Materials Science and Engineering: A*, **513**, pp. 311–318.
- [16] Vasinonta, A., Beuth, J., and Griffith, M., 2000, "Process Maps for Controlling Residual Stress and Melt Pool Size in Laser-Based SFF Processes," *Proceedings of the Annual International Solid Freeform Fabrication Symposium*, pp. 200–208.
- [17] Kummailil, J., Sammarco, C., Skinner, D., Brown, C. A., and Rong, K., 2005, "Effect of Select LENS Processing Parameters on the Deposition of Ti-6Al-4V," *Journal of Manufacturing Processes*, **7**(1), pp. 42–50.
- [18] Montgomery, D. C., 2009, *Design and Analysis of Experiments*, Wiley.
- [19] Raghunath, N., and Pandey, P. M., 2007, "Improving Accuracy through Shrinkage Modelling by Using Taguchi Method in Selective Laser Sintering," *International Journal of Machine Tools and Manufacture*, **47**(6), pp. 985–995.
- [20] Koehler, J. R., and Owen, A. B., 1996, "9 Computer Experiments," *Handbook of Statistics*, pp. 261–308.

- [21] Kleijnen, J. P. C., 2009, "Kriging Metamodeling in Simulation: A Review," *European Journal of Operational Research*, **192**(3), pp. 707–716.
- [22] Myers, R. H., Montgomery, D. C., and Anderson-Cook, C. M., 2009, "Response Surface Methodology: Process and Product Optimization Using Designed Experiments," John Wiley & Sons, p. 825.
- [23] Simpson, and W., T., 1998, "Comparison of Response Surface and Kriging Models in the Multidisciplinary Design of an Aerospike Nozzle," Institute for Computer Applications in Science and Engineering, NASA Langley Research Center.
- [24] Russell, S. J., and Norvig, P., 2010, *Artificial Intelligence : A Modern Approach*, Prentice Hall.
- [25] Lu, Z. L., Li, D. C., Lu, B. H., Zhang, A. F., Zhu, G. X., and Pi, G., 2010, "The Prediction of the Building Precision in the Laser Engineered Net Shaping Process Using Advanced Networks," *Optics and Lasers in Engineering*, **48**(5), pp. 519–525.
- [26] Casalino, G., and Ludovico, A. D., 2002, "Parameter Selection by an Artificial Neural Network for a Laser Bending Process," *Proceedings of the Institution of Mechanical Engineers, Part B: Journal of Engineering Manufacture*, **216**(11), pp. 1517–1520.
- [27] Wang, L., Felicelli, S. D., and Craig, J. E., 2009, "Experimental and Numerical Study of the LENS Rapid Fabrication Process," *Journal of Manufacturing Science and Engineering*, **131**(4), p. 41019.
- [28] Fathi, A., and Mozaffari, A., 2014, "Vector Optimization of Laser Solid Freeform Fabrication System Using a Hierarchical Mutable Smart Bee-Fuzzy Inference System and Hybrid NSGA-II/Self-Organizing Map," *Journal of Intelligent Manufacturing*, **25**(4), pp. 775–795.
- [29] Campbell, T., Williams, C., Ivanova, O., and Garrett, B., 2011, "Could 3D Printing Change the World? Technologies, Potential, and Implications of Additive Manufacturing," Atlantic Council, Washington, DC, pp. 1–15.
- [30] Berman, B., 2012, "3-D Printing: The New Industrial Revolution," *Business Horizons*, **55**(2), pp. 155–162.
- [31] Petrick, I. J., and Simpson, T. W., 2013, "3D Printing Disrupts Manufacturing: How Economies of One Create New Rules of Competition," *Research-Technology Management*, **56**(6), pp. 12–16.

- [32] Spierings, A. B., and Levy, G., 2009, "Comparison of Density of Stainless Steel 316L Parts Produced with Selective Laser Melting Using Different Powder Grades," *Proceedings of the Annual International Solid Freeform Fabrication Symposium*, p. 342–353.
- [33] Averyanova, M., Bertrand, P., and Verquin, B., 2011, "Studying the Influence of Initial Powder Characteristics on the Properties of Final Parts Manufactured by the Selective Laser Melting Technology," *Virtual and Physical Prototyping*, **6**(4), pp. 215–223.
- [34] Kempen, K., Yasa, E., Thijs, L., Kruth, J.-P., and Van Humbeeck, J., 2011, "Microstructure and Mechanical Properties of Selective Laser Melted 18Ni-300 Steel," *Physics Procedia*, **12**, pp. 255–263.
- [35] Van Hooreweder, B., Moens, D., Boonen, R., Kruth, J.-P., and Sas, P., 2012, "Analysis of Fracture Toughness and Crack Propagation of Ti6Al4V Produced by Selective Laser Melting," *Advanced Engineering Materials*, **14**(1–2), pp. 92–97.
- [36] Leuders, S., Thöne, M., Riemer, A., Niendorf, T., Tröster, T., Richard, H. A., and Maier, H. J., 2013, "On the Mechanical Behaviour of Titanium Alloy TiAl6V4 Manufactured by Selective Laser Melting: Fatigue Resistance and Crack Growth Performance," *International Journal of Fatigue*, **48**, pp. 300–307.
- [37] Frazier, W. E., 2014, "Metal Additive Manufacturing: A Review," *Journal of Materials Engineering and Performance*, **23**(6), pp. 1917–1928.
- [38] Foust, M., Thomsen, D., Stickles, R., Cooper, C., and Dodds, W., 2012, "Development of the GE Aviation Low Emissions TAPS Combustor for Next Generation Aircraft Engines," *50th AIAA Aerospace Sciences Meeting Including the New Horizons Forum and Aerospace Exposition*, American Institute of Aeronautics and Astronautics, Reston, Virginia.
- [39] Wohlers, T., and Caffrey, T., 2013, "Additive Manufacturing and 3D Printing State of the Industry," *Annual Worldwide Progress Report 2014*, Wohlers Associates.
- [40] Camisa, J. A., Marler, D., and Madlinger, A., 2014, "Additive Manufacturing and 3D Printing for Oil and Gas-Transformative Potential and Technology Constraints," *Proceedings of the 24th International Ocean and Polar Engineering Conference*, International Society of Offshore and Polar Engineers, Busan, Korea, pp. 299–306.
- [41] Bian, L., Thompson, S. M., and Shamsaei, N., 2015, "Mechanical Properties and Microstructural Features of Direct Laser-Deposited Ti-6Al-4V," *Journal of Manufacturing*, **67**(3), pp. 629–638.

- [42] Van Elsen, M., 2007, “Complexity of Selective Laser Melting : A New Optimization Approach,” University of Leuven.
- [43] Bontha, S., Klingbeil, N. W., Kobryn, P. A., and Fraser, H. L., 2009, “Effects of Process Variables and Size-Scale on Solidification Microstructure in Beam-Based Fabrication of Bulky 3D Structures,” *Materials Science and Engineering: A*, **513–514**, pp. 311–318.
- [44] Kummailil, J., 2004, “Process Models for Laser Engineered Net Shaping,” Worcester Polytechnic Institute.
- [45] Averyanova, M., Cicala, E., Bertrand, P., and Grevey, D., 2012, “Experimental Design Approach to Optimize Selective Laser Melting of Martensitic 17-4 PH Powder: Part I – Single Laser Tracks and First Layer,” *Rapid Prototyping Journal*, **18**(1), pp. 28–37.
- [46] Lynn-Charney, C., and Rosen, D. W., 2000, “Usage of Accuracy Models in Stereolithography Process Planning,” *Rapid Prototyping Journal*, **6**(2), pp. 77–87.
- [47] Zhou, J. G., Herscovici, D., and Chen, C. C., 2000, “Parametric Process Optimization to Improve the Accuracy of Rapid Prototyped Stereolithography Parts,” *International Journal of Machine Tools and Manufacture*, **40**(3), pp. 363–379.
- [48] Averyanova, M., and Bertrand, P., 2009, “Direct Manufacturing of Dense Parts From Martensitic Precipitation Hardening Steel Gas Atomized Powder by Selective Laser Melting (SLM) Technology,” *Proceedings of the International Conference on Advanced Research in Virtual and Rapid Prototyping*, Leiria, Portugal, pp. 343–348.
- [49] Gu, H., Gong, H., Pal, D., Rafi, K., Starr, T., and Stucker, B., 2013, “Influences of Energy Density on Porosity and Microstructure of Selective Laser Melted 17- 4PH Stainless Steel,” *Proceedings of the Annual International Solid Freeform Fabrication Symposium*, pp. 474–489.
- [50] Vastola, J. T., 2012, “Sequential Experimental Design Under Competing Prior Knowledge,” Georgia Institute of Technology.
- [51] Dasgupta, T., 2007, “Robust Parameter Design for Automatically Controlled Systems and Nanostructure Synthesis,” Georgia Institute of Technology.
- [52] Joseph, V. R., Dasgupta, T., Tuo, R., and Wu, C. F. J., 2015, “Sequential Exploration of Complex Surfaces Using Minimum Energy Designs,” *Technometrics*, **57**(1), pp. 64–74.

- [53] Dasgupta, T., 2007, "Robust Parameter Design for Automatically Controlled Systems and Nanostructure Synthesis," Georgia Institute of Technology.
- [54] Morris, M. D., and Mitchell, T. J., 1995, "Exploratory Designs for Computational Experiments," *Journal of Statistical Planning and Inference*, **43**(3), pp. 381–402.
- [55] Jin, R., Chen, W., and Sudjianto, A., 2005, "An Efficient Algorithm for Constructing Optimal Design of Computer Experiments," *Journal of Statistical Planning and Inference*, **134**(1), pp. 268–287.
- [56] Casciato, M. J., 2013, "The Design, Synthesis, and Optimization of Nanomaterials Fabricated in Supercritical Carbon Dioxide," Ph.D. Thesis, Georgia Institute of Technology.
- [57] Casciato, M. J., Vastola, J. T., Lu, J. C., Hess, D. W., and Grover, M. A., 2013, "Initial Experimental Design Methodology Incorporating Expert Conjecture, Prior Data, and Engineering Models for Deposition of Iridium Nanoparticles in Supercritical Carbon Dioxide," *Industrial & Engineering Chemistry Research*, **52**(28), pp. 9645–9653.
- [58] Fedorov, V. V., and Hackl, P., 2012, *Model-Oriented Design of Experiments*, Springer US, New York.
- [59] Spierings, A. B., Wegener, K., and Levy, G., 2012, "Designing Material Properties Locally with Additive Manufacturing Technology SLM," *Proceedings of the Annual International Solid Freeform Fabrication Symposium*, pp. 447–455.
- [60] Yasa, E., and Kruth, J.-P., 2011, "Microstructural Investigation of Selective Laser Melting 316L Stainless Steel Parts Exposed to Laser Re-Melting," *Procedia Engineering*, **19**, pp. 389–395.
- [61] Abe, F., Osakada, K., Shiomi, M., Uematsu, K., and Matsumoto, M., 2001, "The Manufacturing of Hard Tools from Metallic Powders by Selective Laser Melting," *Journal of Materials Processing Technology*, **111**(1–3), pp. 210–213.
- [62] Tolosa, I., Garcand?a, F., Zubiri, F., Zapirain, F., and Esnaola, A., 2010, "Study of Mechanical Properties of AISI 316 Stainless Steel Processed by Selective Laser Melting, Following Different Manufacturing Strategies," *The International Journal of Advanced Manufacturing Technology*, **51**(5–8), pp. 639–647.
- [63] Pinkerton, A. J., and Li, L., 2005, "Direct Additive Laser Manufacturing Using Gas- and Water-Atomised H13 Tool Steel Powders," *The International Journal of Advanced Manufacturing Technology*, **25**(5–6), pp. 471–479.

- [64] Cottam, R., Wang, J., and Luzin, V., 2014, “Characterization of Microstructure and Residual Stress in a 3D H13 Tool Steel Component Produced by Additive Manufacturing,” *Journal of Materials Research*, **29**(17), pp. 1978–1986.
- [65] Cormier, D., Harrysson, O., and West, H., 2004, “Characterization of H13 Steel Produced via Electron Beam Melting,” *Rapid Prototyping Journal*, **10**(1), pp. 35–41.
- [66] Casavola, C., Campanelli, S. L., and Pappalettere, C., 2008, “Experimental Analysis of Residual Stresses in the Selective Laser Melting Process,” *Proceedings of the 6th International Congress and Exposition, Society for Experimental Mechancis, Orlando, Florida* *Proceedings of the XIth International Congress and Exposition, Society for Experimental Mechancis, Orlando, Florida*.
- [67] Antony, K. C., 1963, “Aging Reactions in Precipitation Hardenable Stainless Steel,” *Journal of Metals*, **15**, pp. 922–927.
- [68] Hsiao, C. N., Chiou, C. S., and Yang, J. R., 2002, “Aging Reactions in a 17–4 PH Stainless Steel,” *Materials Chemistry and Physics*, **74**, pp. 134–142.
- [69] Facchini, L., Vicente, N., Lonardelli, I., Magalini, E., Robotti, P., and Molinari, A., 2010, “Metastable Austenite in 17-4 Precipitation-Hardening Stainless Steel Produced by Selective Laser Melting,” *Advanced Engineering Materials*, **12**(3), pp. 184–188.
- [70] Murr, L. E., Martinez, E., Hernandez, J., Collins, S., Amato, K. N., Gaytan, S. M., and Shindo, P. W., 2012, “Microstructures and Properties of 17-4 PH Stainless Steel Fabricated by Selective Laser Melting,” *Journal of Materials Research and Technology*, **1**(3), pp. 167–177.
- [71] Jerrard, P. G. E., Hao, L., and Evans, K. E., 2009, “Experimental Investigation into Selective Laser Melting of Austenitic and Martensitic Stainless Steel Powder Mixtures,” *Proceedings of the Institution of Mechanical Engineers, Part B: Journal of Engineering Manufacture*, **223**(11), pp. 1409–1416.
- [72] Kumar, S., and Kruth, J. P., 2008, “Wear Performance of SLS/SLM Materials,” *Advanced Engineering Materials*, **10**(8), pp. 750–753.
- [73] Gu, H., Gong, H., Pal, D., Rafi, K., Starr, T., and Stucker, B., 2013, “Influences of Energy Density on Porosity and Microstructure of Selective Laser Melted 17-4PH Stainless Steel,” *2013 Solid Freeform Fabrication Symposium*, p. 474.
- [74] Kumar, S., and Kruth, J., 2008, “Wear Performance of SLS/SLM Materials,” *Advanced Engineering Materials*, **10**(8), pp. 750–753.

- [75] Huang, Y., Leu, M. C., Mazumder, J., and Donmez, A., 2015, “Additive Manufacturing: Current State, Future Potential, Gaps and Needs, and Recommendations,” *Journal of Manufacturing Science and Engineering*, **137**(1), p. 14001.
- [76] M.S. Tootooni, A. Dsouza, R. Donovan, P. Rao, Z. Kong, P. B., 2017, “Assessing the Geometric Integrity of Additive Manufactured (AM) Parts from Point Cloud Data Using Spectral Graph Theoretic Sparse Representation-Based Classification,” *Proceedings of Manufacturing Science and Engineering Conference (MSEC) of the ASME (Accepted)*.
- [77] M.S. Tootooni, A. Dsouza, R. Donovan, P. Rao, Z. Kong, P. B., 2017, “Classifying the Dimensional Variation in Additive Manufactured Parts from Laser-Scanned 3D Point Cloud Data Using Machine Learning Approaches,” *ASME Transactions, Journal of Manufacturing Science and Engineering (Accepted)*.
- [78] Dsouza, A., 2016, “Experimental Evolutionary Optimization of Geometric Integrity in Fused Filament Fabrication (FFF) Additive Manufacturing Process,” Binghamton University.
- [79] Vasinonta, A., and Beuth, J., 2000, “Process Maps for Controlling Residual Stress and Melt Pool Size in Laser-Based SFF Processes,” *Proceedings of Solid Freeform Fabrication Symposium Solid Freeform Fabrication Symposium*, pp. 200–208.
- [80] Bochmann, L., Bayley, C., Helu, M., Transchel, R., Wegener, K., and Dornfeld, D., 2015, “Understanding Error Generation in Fused Deposition Modeling,” *Surface Topography: Metrology and Properties*, **3**(1), p. 14002.
- [81] Mahesh, M., Wong, Y. S., Fuh, J. Y. H., and Loh, H. T., 2004, “Benchmarking for Comparative Evaluation of RP Systems and Processes,” *Rapid Prototyping Journal*, **10**(2), pp. 123–135.
- [82] El-Katatny, I., Masood, S. H., and Morsi, Y. S., 2010, “Error Analysis of FDM Fabricated Medical Replicas,” *Rapid Prototyping Journal*, **16**(1), pp. 36–43.
- [83] Weheba, G., and Sanchez-Marsa, A., 2006, “Using Response Surface Methodology to Optimize the Stereolithography Process,” *Rapid Prototyping Journal*, **12**(2), pp. 72–77.
- [84] Deshpande, S., Watson, L. T., and Canfield, R. A., 2013, “Pareto Front Approximation Using a Hybrid Approach,” *Procedia Computer Science*, **18**, pp. 521–530.
- [85] Eichfelder, G., 2008, *Adaptive Scalarization Methods in Multiobjective Optimization*, Springer Berlin Heidelberg, Berlin, Heidelberg.

- [86] Abraham, A., and Jain, L., 2005, “Evolutionary Multiobjective Optimization,” *Evolutionary Multiobjective Optimization*, Springer-Verlag, London, pp. 1–6.
- [87] Kunath, S., Marchyk, N., Haupt, K., and Feller, K.-H., 2013, “Multi-Objective Optimization and Design of Experiments as Tools to Tailor Molecularly Imprinted Polymers Specific for Glucuronic Acid,” *Talanta*, **105**, pp. 211–218.
- [88] Moylan, S., Cooke, A., Jurens, K., Slotwinski, J., Alkan Donmez, M., Bryson, J. E., and Gallagher, P. D., 2012, “A Review of Test Artifacts for Additive Manufacturing.”
- [89] ASME B5.54, 2005, “Methods for Performance Evaluation of Computer Numerically Controlled Machining Centers,” **1998**, p. 177.
- [90] NAS, 1969, *NAS 979 Uniform Cutting Tests--NAS Series Metal Cutting Equipment Specifications*.
- [91] Moylan, S., Slotwinski, J., Cooke, A., Jurens, K., and Alkan Donmez, M., 2014, “An Additive Manufacturing Test Artifact,” *Journal of Research of the National Institute of Standards and Technology*, **119**.
- [92] ASME, 2009, *Y14.5 - Dimensioning and Tolerancing - Engineering Drawing and Related Documentation Practices*, American Society of Mechanical Engineers.
- [93] Aboutaleb, A. M., Bian, L., Shamsaei, N., Thompson, S. M., and Rao, P. K., 2016, “Multi-Objective Process Optimization of Additive Manufacturing: A Case Study on Geometry Accuracy Optimization,” *Proceedings of the Annual International Solid Freeform Fabrication Symposium*, pp. 656–669.
- [94] Aboutaleb, A. M., Bian, L., Shamsaei, N., and Thompson, S. M., 2016, “Systematic Optimization of Laser-Based Additive Manufacturing for Multiple Mechanical Properties,” *2016 IEEE International Conference on Automation Science and Engineering (CASE)*, IEEE, pp. 780–785.
- [95] Knowles, J., 2006, “ParEGO: A Hybrid Algorithm with On-Line Landscape Approximation for Expensive Multiobjective Optimization Problems,” *IEEE Transactions on Evolutionary Computation*, **10**(1), pp. 50–66.
- [96] Okabe, T., Jin, Y., Olhofer, M., and Sendhoff, B., 2004, “On Test Functions for Evolutionary Multi-Objective Optimization,” Springer, Berlin, Heidelberg, pp. 792–802.
- [97] Kim, I. Y., and de Weck, O. L., 2005, “Adaptive Weighted-Sum Method for Bi-Objective Optimization: Pareto Front Generation,” *Structural and Multidisciplinary Optimization*, **29**(2), pp. 149–158.

- [98] Huband, S., Hingston, P., Barone, L., and While, L., 2006, "A Review of Multiobjective Test Problems and a Scalable Test Problem Toolkit," *IEEE Transactions on Evolutionary Computation*, **10**(5), pp. 477–506.
- [99] Van Veldhuizen, D. A., and Lamont, G. B., 1998, "Multiobjective Evolutionary Algorithm Research: A History and Analysis," Technical Report TR-98-03, Department of Electrical and Computer Engineering, Graduate School of Engineering, Air Force Institute of Technology, Wright-Patterson AFB, Ohio.
- [100] Ryu, J.-H., Kim, S., and Wan, H., "Pareto Front Approximation with Adaptive Weighted Sum Method in Multiobjective Simulation Optimization."
- [101] Murr, L. E., Gaytan, S. M., Medina, F., Lopez, H., Martinez, E., Machado, B. I., Hernandez, D. H., Martinez, L., Lopez, M. I., Wicker, R. B., and Bracke, J., 2010, "Next-Generation Biomedical Implants Using Additive Manufacturing of Complex, Cellular and Functional Mesh Arrays," *Philosophical Transactions of the Royal Society of London A: Mathematical, Physical and Engineering Sciences*, **368**(1917), pp. 1999–2039.
- [102] Niinomi, M., 2008, "Mechanical Biocompatibilities of Titanium Alloys for Biomedical Applications," *Journal of the Mechanical Behavior of Biomedical Materials*, **1**(1), pp. 30–42.
- [103] Elias, C. N., Lima, J. H. C., Valiev, R., and Meyers, M. A., 2008, "Biomedical Applications of Titanium and Its Alloys," *JOM*, **60**(3), pp. 46–49.
- [104] Rack, H. J., and Qazi, J. I., 2006, "Titanium Alloys for Biomedical Applications," *Materials Science and Engineering: C*, **26**(8), pp. 1269–1277.
- [105] Matassi, F., Botti, A., Sirleo, L., Carulli, C., and Innocenti, M., 2013, "Porous Metal for Orthopedics Implants," *Clinical cases in mineral and bone metabolism: the official journal of the Italian Society of Osteoporosis, Mineral Metabolism, and Skeletal Diseases*, **10**(2), pp. 111–5.
- [106] Vasconcellos, L., Leite, D., Nascimento, F., Vasconcellos, L. G., Graca, M., Carvalho, Y., and Cairo, C., 2010, "Porous Titanium for Biomedical Applications: An Experimental Study on Rabbits," *Medicina Oral Patología Oral y Cirugía Bucal*, pp. e407–e412.
- [107] TAKAHASHI, M., KIKUCHI, M., and TAKADA, Y., 2002, "Mechanical Properties and Microstructures of Dental Cast Ti-Ag and Ti-Cu Alloys," *Dental materials*.

- [108] Al-Mayouf, A. ., Al-Swayih, A. ., Al-Mobarak, N. ., and Al-Jabab, A. ., 2004, “Corrosion Behavior of a New Titanium Alloy for Dental Implant Applications in Fluoride Media,” *Materials Chemistry and Physics*, **86**(2–3), pp. 320–329.
- [109] Boyer, R., 1996, “An Overview on the Use of Titanium in the Aerospace Industry,” *Materials Science and Engineering: A*, **213**(1), pp. 103–114.
- [110] Peters, M., Kumpfert, J., Ward, C. H., and Leyens, C., 2003, “Titanium Alloys for Aerospace Applications,” *Advanced Engineering Materials*, **5**(6), pp. 419–427.
- [111] Leyens, C. (Christoph), Peters, M. (Manfred), John Wiley & Sons., and Wiley InterScience (Online service), 2003, *Titanium and Titanium Alloys : Fundamentals and Applications*, Wiley-VCH.
- [112] Tung, S. C., and McMillan, M. L., 2004, “Automotive Tribology Overview of Current Advances and Challenges for the Future,” *Tribology International*, **37**(7), pp. 517–536.
- [113] Sachdev, A. K., Kulkarni, K., Fang, Z. Z., Yang, R., and Girshov, V., 2012, “Titanium for Automotive Applications: Challenges and Opportunities in Materials and Processing,” *JOM*, **64**(5), pp. 553–565.
- [114] Aboutaleb, A. M., and Bian, L., 2017, “Optimization of Laser-Based Additive Manufacturing,” *Laser-Based Additive Manufacturing of Metal Parts: Modeling, Optimization, and Control of Mechanical Properties*, CRC Press, Taylor & Francis Group, pp. 137–160.
- [115] Gong, H., Rafi, K., Gu, H., Starr, T., and Stucker, B., 2014, “Analysis of Defect Generation in Ti–6Al–4V Parts Made Using Powder Bed Fusion Additive Manufacturing Processes,” *Additive Manufacturing*, **1–4**, pp. 87–98.
- [116] Rafi, H. K., Karthik, N. V., Gong, H., Starr, T. L., and Stucker, B. E., 2013, “Microstructures and Mechanical Properties of Ti6Al4V Parts Fabricated by Selective Laser Melting and Electron Beam Melting,” *Journal of Materials Engineering and Performance*, **22**(12), pp. 3872–3883.
- [117] 2014, “Effects of Defects in Laser Additive Manufactured Ti-6Al-4V on Fatigue Properties,” *Physics Procedia*, **56**, pp. 371–378.
- [118] Yadollahi, A., and Shamsaei, N., 2017, “Additive Manufacturing of Fatigue Resistant Materials: Challenges and Opportunities,” *International Journal of Fatigue*, **98**, pp. 14–31.

- [119] Bagheri, A., Mahtabi, M. J., and Shamsaei, N., 2017, “Fatigue Behavior and Cyclic Deformation of Additive Manufactured NiTi,” *Journal of Materials Processing Technology*.
- [120] Utyuzhnikov, s. v., Fantini, P., and Guenov, M. D., 2009, “A Method for Generating a Well-Distributed Pareto Set in Nonlinear Multiobjective Optimization,” *Journal of Computational and Applied Mathematics*, **223**(2), pp. 820–841.
- [121] Collette, Y., and Siarry, P., 2003, *Multiobjective Optimization: Principles and Case Studies*, Springer, Berlin, Heidelberg, New York.
- [122] Deb, D., 2001, *Multi-Objective Optimization Using Evolutionary Algorithms*, J. Wiley & Sons, Chichester.
- [123] Deb, K., Pratap, A., Agarwal, S., and Meyarivan, T., 2002, “A Fast and Elitist Multiobjective Genetic Algorithm: NSGA-II,” *IEEE Transactions on Evolutionary Computation*, **6**(2), pp. 182–197.
- [124] Hrabe, N., and Quinn, T., 2013, “Effects of Processing on Microstructure and Mechanical Properties of a Titanium Alloy (Ti–6Al–4V) Fabricated Using Electron Beam Melting (EBM), Part 2: Energy Input, Orientation, and Location,” *Materials Science and Engineering: A*, **573**, pp. 271–277.
- [125] Selcuk, C., 2011, “Laser Metal Deposition for Powder Metallurgy Parts,” *Powder Metallurgy*, **54**(2), pp. 94–99.
- [126] Simonelli, M., Tse, Y. Y., and Tuck, C., 2014, “Effect of the Build Orientation on the Mechanical Properties and Fracture Modes of SLM Ti-6Al-4V,” *Materials Science and Engineering A*, **616**, pp. 1–11.
- [127] Wauthle, R., Vrancken, B., Beynaerts, B., Jorissen, K., Schrooten, J., Kruth, J. P., and Van Humbeeck, J., 2015, “Effects of Build Orientation and Heat Treatment on the Microstructure and Mechanical Properties of Selective Laser Melted Ti6Al4V Lattice Structures,” *Additive Manufacturing*, **5**, pp. 77–84.
- [128] Carroll, B. E., Palmer, T. A., and Beese, A. M., 2015, “Anisotropic Tensile Behavior of Ti-6Al-4V Components Fabricated with Directed Energy Deposition Additive Manufacturing,” *Acta Materialia*, **87**, pp. 309–320.
- [129] Baufeld, B., Biest, O. Van der, and Gault, R., 2010, “Additive Manufacturing of Ti-6Al-4V Components by Shaped Metal Deposition: Microstructure and Mechanical Properties,” *Materials and Design*, **31**(SUPPL. 1), pp. S106–S111.

- [130] Wang, Y., Zhang, S., Tian, X., and Wang, H., 2013, "High-Cycle Fatigue Crack Initiation and Propagation in Laser Melting Deposited TC18 Titanium Alloy," *International Journal of Minerals, Metallurgy, and Materials*, **20**(7), pp. 665–670.
- [131] Yadollahi, A., Mahtabi, M. J., Khalili, A., Newman, J. C., and Doude, H., 2017, "Fatigue-Life Prediction of Additively-Manufactured Material: Effects of Surface Roughness, Defect Size and Shape," *International Journal of Fatigue* (Under Review).
- [132] Silva, A. C. F., Braga, D. F. O., de Figueiredo, M. A. V, and Moreira, P. M. G. P., 2015, "Ultimate Tensile Strength Optimization of Different FSW Aluminium Alloy Joints," *International Journal of Advanced Manufacturing Technology*, **79**(5–8), pp. 805–814.
- [133] Bozkurt, Y., 2012, "The Optimization of Friction Stir Welding Process Parameters to Achieve Maximum Tensile Strength in Polyethylene Sheets," *Materials and Design*, **35**, pp. 440–445.
- [134] Ampaipoon, A., Lasunon, O. U., and Bubphachot, B., 2015, "Optimization and Prediction of Ultimate Tensile Strength in Metal Active Gas Welding," *Scientific World Journal*, **2015**.
- [135] Aboutaleb, A. M., Tschopp, M. A., Rao, P. K., and Bian, L., 2017, "Multi-Objective Accelerated Process Optimization of Part Geometric Accuracy in Additive Manufacturing," *Journal of Manufacturing Science and Engineering*.
- [136] Aboutaleb, A. M., Bian, L., Rao, P. K., and Tschopp, M. A., 2017, "Accelerated Geometry Accuracy Optimization of Additive Manufacturing Parts," *ASME 12th International Manufacturing Science and Engineering Conference*.
- [137] "ASTM B348-13, Standard Specification for Titanium and Titanium Alloy Bars and Billets, ASTM International, West Conshohocken, PA, 2013, [Www.astm.org](http://www.astm.org)."
- [138] "ASTM E8 / E8M-13, Standard Test Methods for Tension Testing of Metallic Materials, ASTM International, West Conshohocken, PA, 2013, [Www.astm.org](http://www.astm.org)."
- [139] Zitzler, E., Thiele, L., Laumanns, M., Fonseca, C. M., and da Fonseca, V. G., 2003, "Performance Assessment of Multiobjective Optimizers: An Analysis and Review," *IEEE Transactions on Evolutionary Computation*, **7**(2), pp. 117–132.

APPENDIX A
PRIOR DISTRIBUTION OF λ'_i s

Since λ'_i 's are assumed independent, their joint distribution would be resulted by multiplying their distribution by each other as follows:

$$\begin{aligned}
\pi(\lambda) &= \prod_{i=1}^{n_p} (2\pi\omega_i^2)^{\frac{-1}{2}} \exp\left\{\frac{-1}{2\omega_i^2}(\lambda_i - \beta_i)^2\right\} \\
&= \left(\prod_{i=1}^{n_p} (2\pi\omega_i^2)^{\frac{-1}{2}}\right) \times \exp\left\{\sum_{i=1}^{n_p} \frac{-1}{2\omega_i^2}(\lambda_i - \beta_i)^2\right\} \\
&= \left(\prod_{i=1}^{n_p} (2\pi\omega_i^2)^{\frac{-1}{2}}\right) \\
&\quad \times \exp\left\{\frac{-1}{2}\sum_{i=1}^{n_p} \frac{\lambda_i^2}{\omega_i^2} + \sum_{i=1}^{n_p} \frac{\lambda_i\beta_i}{\omega_i^2} - \frac{1}{2}\sum_{i=1}^{n_p} \frac{\beta_i^2}{\omega_i^2}\right\}
\end{aligned}$$

Expanded prior distribution of λ'_i 's can be re-arranged according to the terms involving λ'_i 's as follows:

$$\pi(\lambda) \propto \exp\left\{\frac{-1}{2}\sum_{i=1}^{n_p} \frac{\lambda_i^2}{\omega_i^2} + \sum_{i=1}^{n_p} \frac{\lambda_i\beta_i}{\omega_i^2}\right\}$$

APPENDIX B

PROPORTIONAL FORMULA OF $f(\boldsymbol{Y} \mid \boldsymbol{\lambda}, \boldsymbol{u})$

Since the design points are generated sequentially, distribution of Y_j depends on prior data \mathbf{u} , updated DRPCS's $\boldsymbol{\lambda}$ and the responses from prior batches of experiments in the current study $Y_1, Y_2, \dots, Y_{\lfloor \frac{j-1}{b} \rfloor b}$. Hence, assuming that distribution of Y_j follows a normal distribution, it can be represented as follows:

$$f_j \left(Y_j \middle| Y_1, Y_2, \dots, Y_{\lfloor \frac{j-1}{b} \rfloor b}, \mathbf{u}, \boldsymbol{\lambda} \right) = (2\pi\sigma_j^2)^{-\frac{1}{2}} \exp \left\{ \frac{-1}{2\sigma_j^2} (Y_j - \mu_j)^2 \right\}$$

$$\mu_j = E[Y_j] = \sum_{i=1}^{n_p} w_{j,i} (u_i + \lambda_i) + \sum_{j'=1}^{\lfloor \frac{j-1}{b} \rfloor b} v_{j,j'} y_{j'}$$

Based on the definition of conditional distribution, joint distribution of Y_j 's can be resulted by multiplying their conditional distributions as follows:

$$\begin{aligned} f(\mathbf{Y}|\boldsymbol{\lambda}, \mathbf{u}) &= \prod_{j=1}^{n_c} f_j \left(Y_j \middle| Y_1, Y_2, \dots, Y_{\lfloor \frac{j-1}{b} \rfloor b}, \mathbf{u}, \boldsymbol{\lambda} \right) \\ &= \prod_{j=1}^{n_c} (2\pi\sigma_j^2)^{-\frac{1}{2}} \exp \left\{ \frac{-1}{2\sigma_j^2} (Y_j - \mu_j)^2 \right\} \\ &= \prod_{j=1}^{n_c} (2\pi\sigma_j^2)^{-\frac{1}{2}} \exp \left\{ \frac{-1}{2\sigma_j^2} \left(Y_j - \sum_{i=1}^{n_p} w_{j,i} u_i - \sum_{i=1}^{n_p} w_{j,i} \lambda_i \right. \right. \\ &\quad \left. \left. - \sum_{j'=1}^{\lfloor \frac{j-1}{b} \rfloor b} v_{j,j'} y_{j'} \right)^2 \right\} \end{aligned}$$

If we denote $\delta_j = Y_j - \sum_{i=1}^{n_p} w_{j,i} u_i - \sum_{j'=1}^{\lfloor \frac{j-1}{b} \rfloor b} v_{j,j'} y_{j'}$, $f(\mathbf{Y}|\boldsymbol{\lambda}, \mathbf{u})$ can be re-arranged as follows:

$$f(\mathbf{Y}|\boldsymbol{\lambda}, \mathbf{u}) = \prod_{j=1}^{n_c} (2\pi\sigma_j^2)^{-\frac{1}{2}} \exp \left\{ \frac{-1}{2\sigma_j^2} \left[\left(\sum_{i=1}^{n_p} w_{j,i} \lambda_i \right)^2 + \delta_j^2 - 2\delta_j \sum_{i=1}^{n_p} w_{j,i} \lambda_i \right] \right\}$$

Expanded proportional form of this formula is as follows:

$$f(\mathbf{Y}|\boldsymbol{\lambda}, \mathbf{u}) \propto \exp \left\{ \frac{-1}{2} \sum_{j=1}^{n_c} \frac{1}{\sigma_j^2} \left(\sum_{i=1}^{n_p} w_{j,i} \lambda_i \right)^2 + \sum_{j=1}^{n_c} \frac{\delta_j}{\sigma_j^2} \sum_{i=1}^{n_p} w_{j,i} \lambda_i - \frac{1}{2} \sum_{j=1}^{n_c} \left(\frac{\delta_j}{\sigma_j} \right)^2 \right\}$$

By factoring λ_i 's out we can reorganize proportional formula of $f(\mathbf{Y}|\boldsymbol{\lambda}, \mathbf{u})$ as follows:

$$f(\mathbf{Y}|\boldsymbol{\lambda}, \mathbf{u}) \propto \exp \left\{ \frac{-1}{2} \left(\sum_{i=1}^{n_p} \lambda_i^2 \sum_{j=1}^{n_c} \frac{w_{j,i}^2}{\sigma_j^2} + 2 \sum_{i \neq k} \lambda_i \lambda_k \sum_{j=1}^{n_c} \frac{w_{j,i} w_{j,k}}{\sigma_j^2} \right) + \sum_{i=1}^{n_p} \lambda_i \sum_{j=1}^{n_c} \frac{w_{j,i} \delta_j}{\sigma_j^2} - \frac{1}{2} \sum_{j=1}^{n_c} \left(\frac{\delta_j}{\sigma_j} \right)^2 \right\}$$

Proportional formula of $f(\mathbf{Y}|\boldsymbol{\lambda}, \mathbf{u})$ can be rearranged according to the terms involving λ_i 's

as follows:

$$f(\mathbf{Y}|\boldsymbol{\lambda}) \propto \exp \left\{ \frac{-1}{2} \left(\sum_{i=1}^{n_p} \lambda_i^2 \sum_{j=1}^{n_c} \frac{w_{j,i}^2}{\sigma_j^2} + 2 \sum_{i \neq k} \lambda_i \lambda_k \sum_{j=1}^{n_c} \frac{w_{j,i} w_{j,k}}{\sigma_j^2} \right) + \sum_{i=1}^{n_p} \lambda_i \sum_{j=1}^{n_c} \frac{w_{j,i} \delta_j}{\sigma_j^2} \right\}$$

APPENDIX C
POSTERIOR DISTRIBUTION OF λ_i 's

By multiplying the expanded form of $f(\mathbf{Y}|\boldsymbol{\lambda})$ and $\pi(\boldsymbol{\lambda})$, the posterior distribution of λ_i using the Bayesian formula would be resulted as follows:

$$g(\boldsymbol{\lambda}|\mathbf{y}) \propto \exp \left\{ \frac{-1}{2} \sum_{i=1}^{n_p} \frac{\lambda_i^2}{\omega_i^2} + \sum_{i=1}^{n_p} \frac{\lambda_i \beta_i}{\omega_i^2} - \frac{1}{2} \left(\sum_{i=1}^{n_p} \lambda_i^2 \sum_{j=1}^{n_c} \frac{w_{j,i}^2}{\sigma_j^2} + 2 \sum_{i \neq k} \lambda_i \lambda_k \sum_{j=1}^{n_c} \frac{w_{j,i} w_{j,k}}{\sigma_j^2} \right) \right. \\ \left. + \sum_{i=1}^{n_p} \lambda_i \sum_{j=1}^{n_c} \frac{w_{j,i} \delta_j}{\sigma_j^2} \right\}$$

Trying to factoring out the λ 's terms, the formula above can be re-arranged as follows:

$$g(\boldsymbol{\lambda}|\mathbf{y}) \propto \exp \left\{ \frac{-1}{2} \left(\sum_{i=1}^{n_p} \lambda_i^2 \left(\sum_{j=1}^{n_c} \frac{w_{j,i}^2}{\sigma_j^2} + \frac{1}{\omega_i^2} \right) + 2 \sum_{i \neq k} \lambda_i \lambda_k \sum_{j=1}^{n_c} \frac{w_{j,i} w_{j,k}}{\sigma_j^2} \right) \right. \\ \left. + \sum_{i=1}^{n_p} \lambda_i \left(\sum_{j=1}^{n_c} \frac{w_{j,i} \delta_j}{\sigma_j^2} + \frac{\beta_i}{\omega_i^2} \right) \right\}$$

APPENDIX D
CALCULATION OF Λ AND η

Here we show the steps of matrix multiplications as follows:

$$\begin{aligned}
\boldsymbol{\lambda}^T \boldsymbol{\Lambda} \boldsymbol{\lambda} &= (\lambda_1 \quad \lambda_2 \quad \cdots \quad \lambda_{n_p})_{1 \times n_p} \times \begin{pmatrix} \Lambda_{1,1} & \Lambda_{1,2} & \cdots & \Lambda_{1,n_p} \\ \Lambda_{2,1} & & \ddots & \Lambda_{2,n_p} \\ \vdots & & & \vdots \\ \Lambda_{n_p,1} & \Lambda_{n_p,2} & \cdots & \Lambda_{n_p,n_p} \end{pmatrix}_{n_p \times n_p} \times \begin{pmatrix} \lambda_1 \\ \lambda_2 \\ \vdots \\ \lambda_{n_p} \end{pmatrix}_{n_p \times 1} \\
&= (\lambda_1 \Lambda_{1,1} + \lambda_2 \Lambda_{2,1} + \cdots + \lambda_{n_p} \Lambda_{n_p,1} \quad \lambda_1 \Lambda_{1,2} + \lambda_2 \Lambda_{2,2} + \cdots + \lambda_{n_p} \Lambda_{n_p,2} \\
&\quad \cdots \quad \lambda_1 \Lambda_{1,n_p} + \lambda_2 \Lambda_{2,n_p} + \cdots + \lambda_{n_p} \Lambda_{n_p,n_p})_{1 \times n_p} \times \begin{pmatrix} \lambda_1 \\ \lambda_2 \\ \vdots \\ \lambda_{n_p} \end{pmatrix}_{n_p \times 1} \\
&= (\lambda_1^2 \Lambda_{1,1} + \lambda_2 \lambda_1 \Lambda_{2,1} + \cdots + \lambda_{n_p} \lambda_1 \Lambda_{n_p,1}) + (\lambda_1 \lambda_2 \Lambda_{1,2} + \lambda_2^2 \Lambda_{2,2} + \cdots + \lambda_{n_p} \lambda_2 \Lambda_{n_p,2}) \\
&\quad + \cdots + (\lambda_1 \lambda_{n_p} \Lambda_{1,n_p} + \lambda_2 \lambda_{n_p} \Lambda_{2,n_p} + \cdots + \lambda_{n_p}^2 \Lambda_{n_p,n_p})
\end{aligned}$$

Now $\boldsymbol{\lambda}^T \boldsymbol{\Lambda} \boldsymbol{\lambda}$ can be summarized and represented by its elements as follows:

$$\boldsymbol{\lambda}^T \boldsymbol{\Lambda} \boldsymbol{\lambda} = \sum_{i=1}^{n_p} \lambda_i^2 \Lambda_{i,i} + \sum_{i \neq k} \lambda_i \lambda_k \Lambda_{i,k}$$

By comparing the formula above with the final form of $g(\boldsymbol{\lambda}|\mathbf{y})$ in Appendix B, we can see the similarity between resulted terms in $\boldsymbol{\lambda}^T \boldsymbol{\Lambda} \boldsymbol{\lambda}$ and the coefficients of λ 's terms in $g(\boldsymbol{\lambda}|\mathbf{y})$. Hence, elements of $\boldsymbol{\Lambda}$ can be presented as follows:

$$\Lambda_{i,k} = \begin{cases} \sum_{j=1}^{n_c} \frac{w_{j,i}^2}{\sigma_j^2} + \frac{1}{\omega_i^2} & i = k \\ \sum_{j=1}^{n_c} \frac{w_{j,i} w_{j,k}}{\sigma_j^2}, & i \neq k \end{cases}$$

Moreover, by comparing canonical form of multivariate normal

distribution, $h_2(\mathbf{z}|\boldsymbol{\eta}, \boldsymbol{\Lambda}) \propto \exp\left\{a + \boldsymbol{\eta}^T \mathbf{z} - \frac{1}{2} \mathbf{z}^T \boldsymbol{\Lambda} \mathbf{z}\right\}$, and $g(\boldsymbol{\lambda}|\mathbf{y})$ in Appendix B we can

see that elements of $\boldsymbol{\eta}$ can be represented as follows:

$$\eta_i = \sum_{j=1}^{n_c} \frac{w_{j,i} \delta_j}{\sigma_j^2} + \frac{\beta_i}{\omega_i^2}$$

APPENDIX E

EXPERIMENTAL RESULTS FOR APO SIMULATIONS

The improvement in number of experimental runs using our method, compared to SMED, is highlighted in red.

Table E.1 Prior data with negative DRPCS.

Experiment Number	Laser Power (W)	Laser Velocity (mm/s)	SMED Hatch Distance (mm)	Laser Thickness (mm)	Relative Density	Experiment Number	Laser Power (W)	Laser Velocity (mm/s)	Our Method Hatch Distance (mm)	Laser Thickness (mm)	Relative Density
1	44	2000	0.05	0.03	0.7295	1	44	2000	0.05	0.03	0.7295
2	45	400	0.15	0.05	0.7268	2	45	400	0.15	0.05	0.7268
3	40	400	0.1	0.05	0.7831	3	40	400	0.1	0.05	0.7831
4	40	400	0.15	0.04	0.7328	4	40	400	0.15	0.04	0.7328
5	40	400	0.05	0.05	0.9692	5	40	400	0.05	0.05	0.9692
6	44	600	0.1	0.05	0.7295	6	44	600	0.1	0.05	0.7295
7	41	400	0.05	0.05	0.9725	7	41	400	0.05	0.05	0.9725
8	42	400	0.05	0.05	0.9754	8	42	400	0.05	0.05	0.9754
9	43	400	0.05	0.05	0.9780	9	43	400	0.05	0.05	0.9780
10	44	400	0.05	0.05	0.9805	10	44	400	0.05	0.05	0.9805
11	43	600	0.05	0.05	0.9016	11	43	600	0.05	0.05	0.9016
12	45	400	0.05	0.05	0.9827	12	45	400	0.05	0.05	0.9827
13	40	800	0.05	0.05	0.7831	13	40	800	0.05	0.05	0.7831
14	44	800	0.05	0.05	0.8164	14	44	800	0.05	0.05	0.8164
15	40	400	0.05	0.04	0.9909	15	40	400	0.05	0.04	0.9909
16	40	600	0.05	0.05	0.8806	16	45	400	0.05	0.04	0.9967
17	41	400	0.05	0.04	0.9924						
18	42	400	0.05	0.04	0.9937						
19	43	400	0.05	0.04	0.9948						
20	44	400	0.05	0.04	0.9958						
21	42	600	0.05	0.04	0.9477						
22	45	400	0.05	0.04	0.9967						

Improvement = 27.27%

Table E.2 Prior data with smaller DRPCS (compared to Table E.1).

Experiment Number	SMED				Experiment Number	Our Method					
	Laser Power (W)	Laser Velocity (mm/s)	Hatch Distance (mm)	Laser Thickness (mm)		Relative Density	Laser Power (W)	Laser Velocity (mm/s)	Hatch Distance (mm)	Laser Thickness (mm)	Relative Density
1	45	400	0.15	0.05	0.7268	1	45	400	0.15	0.05	0.7268
2	41	800	0.15	0.03	0.9496	2	41	800	0.15	0.03	0.9496
3	44	800	0.15	0.03	0.8406	3	44	800	0.15	0.03	0.8406
4	40	400	0.15	0.03	0.8199	4	40	400	0.15	0.03	0.8199
5	42	800	0.15	0.03	0.9067	5	42	800	0.15	0.03	0.9067
6	40	800	0.1	0.03	0.7328	6	40	800	0.1	0.03	0.7328
7	40	600	0.15	0.03	0.7281	7	40	600	0.15	0.03	0.7281
8	41	600	0.15	0.04	0.9496	8	40	400	0.05	0.05	0.9692
9	43	600	0.15	0.04	0.8708	9	42	400	0.05	0.05	0.9754
10	40	400	0.15	0.04	0.7328	10	43	400	0.05	0.05	0.9780
11	42	600	0.15	0.04	0.9067	11	44	400	0.05	0.05	0.9805
12	40	400	0.05	0.05	0.9692	12	45	400	0.05	0.05	0.9827
13	42	400	0.05	0.05	0.9754	13	44	600	0.05	0.05	0.9078
14	43	400	0.05	0.05	0.9780	14	41	400	0.05	0.05	0.9725
15	44	400	0.05	0.05	0.9805	15	40	800	0.05	0.05	0.7831
16	45	400	0.05	0.05	0.9827	16	40	400	0.05	0.04	0.9909
17	44	600	0.05	0.05	0.9078	17	41	400	0.05	0.04	0.9924
18	41	400	0.05	0.05	0.9725	18	42	400	0.05	0.04	0.9937
19	40	800	0.05	0.05	0.7831	19	43	400	0.05	0.04	0.9948
20	40	400	0.05	0.04	0.9909	20	44	400	0.05	0.04	0.9958
21	41	400	0.05	0.04	0.9924	21	45	400	0.05	0.04	0.9967
22	42	400	0.05	0.04	0.9937						
23	43	400	0.05	0.04	0.9948						
24	44	400	0.05	0.04	0.9958						
25	45	400	0.05	0.04	0.9967						
						Improvement = 16%					

Table E.3 Prior data with positive and negative DRPCS.

Experiment Number	SMED				Experiment Number	Our Method				
	Laser Power (W)	Laser Velocity (mm/s)	Hatch Distance (mm)	Laser Thickness (mm)		Relative Density	Laser Power (W)	Laser Velocity (mm/s)	Hatch Distance (mm)	Laser Thickness (mm)
1	44	800	0.15	0.03	1	44	800	0.15	0.03	0.8406
2	44	600	0.15	0.04	2	44	600	0.15	0.04	0.8406
3	45	400	0.15	0.05	3	45	400	0.15	0.05	0.7268
4	40	400	0.15	0.03	4	44	1200	0.1	0.03	0.8406
5	44	1200	0.1	0.03	5	45	400	0.15	0.03	0.8602
6	44	800	0.1	0.03	6	44	600	0.1	0.03	0.8528
7	40	400	0.15	0.04	7	40	400	0.1	0.03	0.9381
8	44	600	0.15	0.03	8	43	400	0.1	0.03	0.9521
9	45	400	0.05	0.05	9	45	400	0.1	0.03	0.9597
10	44	400	0.05	0.05	10	44	400	0.1	0.03	0.9560
11	42	400	0.05	0.05	11	42	400	0.1	0.03	0.9477
12	43	400	0.05	0.05	12	41	400	0.1	0.03	0.9431
13	40	400	0.05	0.05	13	40	400	0.05	0.03	0.9999
14	44	600	0.05	0.05						
15	41	400	0.05	0.05						
16	40	800	0.05	0.05						
17	40	600	0.05	0.05						
18	41	400	0.05	0.04						
19	40	400	0.05	0.04						
20	42	400	0.05	0.04						
21	43	400	0.05	0.04						
22	44	400	0.05	0.04						
23	45	400	0.05	0.04						

Improvement = 43.4%

Table E.4 Prior data with positive DRPCS.

Experiment Number	SMED				Experiment Number	Our Method				
	Laser Power (W)	Laser Velocity (mm/s)	Hatch Distance (mm)	Laser Thickness (mm)		Relative Density	Laser Power (W)	Laser Velocity (mm/s)	Hatch Distance (mm)	Laser Thickness (mm)
1	44	800	0.15	0.03	1	44	800	0.15	0.03	0.8406
2	44	2000	0.05	0.03	2	44	2000	0.05	0.03	0.7295
3	44	1800	0.05	0.04	3	45	400	0.15	0.05	0.7268
4	45	400	0.15	0.05	4	45	400	0.15	0.03	0.8602
5	44	1400	0.05	0.05	5	44	1200	0.1	0.03	0.8406
6	44	1200	0.1	0.03	6	44	1400	0.05	0.05	0.8098
7	44	1400	0.05	0.04	7	45	400	0.1	0.03	0.9597
8	45	400	0.15	0.03	8	42	400	0.1	0.03	0.9477
9	45	400	0.1	0.03	9	44	400	0.1	0.03	0.9560
10	43	400	0.1	0.03	10	40	400	0.1	0.03	0.9381
11	40	400	0.1	0.03	11	44	600	0.1	0.03	0.8528
12	44	400	0.1	0.03	12	43	400	0.1	0.03	0.9521
13	42	400	0.1	0.03	13	41	400	0.1	0.03	0.9431
14	44	600	0.1	0.03	14	40	400	0.05	0.03	0.9999
15	41	400	0.1	0.03						
16	43	400	0.05	0.03						
Improvement = 12.5%										

Table E.5 More prior data points.

Experiment Number	SMED				Experiment Number	Our Method				
	Laser Power (W)	Laser Velocity (mm/s)	Hatch Distance (mm)	Laser Thickness (mm)		Relative Density	Laser Power (W)	Laser Velocity (mm/s)	Hatch Distance (mm)	Laser Thickness (mm)
1	45	400	0.15	0.05	1	45	400	0.15	0.05	0.7268
2	45	400	0.05	0.05	2	45	400	0.05	0.05	0.9827
3	44	400	0.05	0.05	3	44	400	0.05	0.05	0.980
4	42	400	0.05	0.05	4	42	400	0.05	0.05	0.9754
5	43	400	0.05	0.05	5	43	400	0.05	0.05	0.9780
6	40	400	0.05	0.05	6	40	400	0.05	0.05	0.9692
7	44	600	0.05	0.05	7	44	600	0.05	0.05	0.9078
8	41	400	0.05	0.05	8	41	400	0.05	0.05	0.9725
9	40	800	0.05	0.05	9	40	800	0.05	0.05	0.7831
10	40	600	0.05	0.05	10	40	400	0.05	0.04	0.9909
11	40	400	0.05	0.04	11	41	400	0.05	0.04	0.9924
12	41	400	0.05	0.04	12	42	400	0.05	0.04	0.9937
13	42	400	0.05	0.04	13	43	400	0.05	0.04	0.9948
14	43	400	0.05	0.04	14	44	400	0.05	0.04	0.9958
15	44	400	0.05	0.04	15	45	400	0.05	0.04	0.9967
16	45	400	0.05	0.04	Improvement = 6.25%					

APPENDIX F

EFFECT OF γ ON THE OPTIMIZATION PERFORMANCE

Although there is not any universal guideline for choosing an appropriate charge function, the performance of the proposed method and SMED is examined given charge functions $q(\mathbf{s}) = (1 - \gamma(\mathbf{s}))^\gamma$ for $\gamma = 1, 3, 5$. This charge function is suggested by Ref. [51]. The simulations of this part are applied to multiple scenarios: negative DRPCS, positive and negative DRPCS, and positive DRPCS. The results are summarized in Tables F.1—F.9. Note that we used the charge function with $\gamma = 3$ in Section 3.1.1 and 3.1.2 to investigate the effects of DRPCS. Tables F.4—F.6 are identical to Tables E.1, E.3, and E.4, respectively. We include them in this section for the convenience of the reader.

a. Simulations for $\gamma = 1$

Table F.1 Performance of SMED and our method with negative DRPCS and $\gamma=1$.

Experiment Number	SMED					Our Method					
	Laser Power (W)	Laser Velocity (mm/s)	Hatch Distance (mm)	Laser Thickness (mm)	Relative Density	Experiment Number	Laser Power (W)	Laser Velocity (mm/s)	Hatch Distance (mm)	Laser Thickness (mm)	Relative Density
1	44	2000	0.05	0.03	0.7295	1	44	2000	0.05	0.03	0.7295
2	45	400	0.15	0.05	0.7268	2	45	400	0.15	0.05	0.7268
3	40	400	0.05	0.05	0.9692	3	40	400	0.05	0.05	0.9692
4	40	400	0.15	0.03	0.8199	4	40	400	0.15	0.03	0.8199
5	40	600	0.05	0.05	0.8806	5	40	600	0.05	0.05	0.8806
6	45	400	0.05	0.05	0.9827	6	45	400	0.05	0.05	0.9827
7	44	400	0.05	0.05	0.9805	7	44	400	0.05	0.05	0.9805
8	44	1000	0.05	0.05	0.7443	8	44	1000	0.05	0.05	0.7443
9	40	400	0.05	0.04	0.9909	9	40	400	0.05	0.04	0.9909
10	43	400	0.05	0.05	0.9780	10	43	400	0.05	0.05	0.9780
11	42	400	0.05	0.04	0.9937	11	42	400	0.05	0.04	0.9937
12	45	400	0.05	0.04	0.9967	12	45	400	0.05	0.04	0.9967

Table F.2 Performance of SMED and our method with positive and negative DRPCS and $\gamma=1$.

Experiment Number	SMED					Our Method					
	Laser Power (W)	Laser Velocity (mm/s)	Hatch Distance (mm)	Laser Thickness (mm)	Relative Density	Experiment Number	Laser Power (W)	Laser Velocity (mm/s)	Hatch Distance (mm)	Laser Thickness (mm)	Relative Density
1	45	400	0.15	0.05	0.7268	1	44	2000	0.05	0.03	0.7295
2	44	800	0.15	0.03	0.8406	2	45	400	0.15	0.05	0.7268
3	44	2000	0.05	0.03	0.7295	3	40	400	0.05	0.05	0.9692
4	45	400	0.05	0.05	0.9827	4	40	400	0.15	0.03	0.8199
5	40	400	0.05	0.05	0.9692	5	40	600	0.05	0.05	0.8806
6	44	600	0.05	0.05	0.9078	6	45	400	0.05	0.05	0.9827
7	43	400	0.05	0.05	0.9780	7	44	400	0.05	0.05	0.9805
8	40	1000	0.05	0.05	0.7274	8	44	1000	0.05	0.05	0.7443
9	40	400	0.05	0.04	0.9909	9	40	400	0.05	0.04	0.9909
10	44	400	0.05	0.04	0.9958	10	43	400	0.05	0.05	0.9780
11	45	400	0.05	0.04	0.9967	11	42	400	0.05	0.04	0.9937

Table F.3 Performance of SMED and our method with positive DRPCS and $\gamma=1$.

Experiment Number	SMED					Our Method					
	Laser Power (W)	Laser Velocity (mm/s)	Hatch Distance (mm)	Laser Thickness (mm)	Relative Density	Experiment Number	Laser Power (W)	Laser Velocity (mm/s)	Hatch Distance (mm)	Laser Thickness (mm)	Relative Density
1	45	400	0.15	0.05	0.7268	1	45	400	0.15	0.05	0.7268
2	44	2000	0.05	0.03	0.7295	2	44	2000	0.05	0.03	0.7295
3	44	1800	0.05	0.04	0.8406	3	44	1400	0.05	0.05	0.8098
4	44	800	0.15	0.03	0.8406	4	44	800	0.15	0.03	0.8406
5	44	1400	0.05	0.05	0.8098	5	40	400	0.05	0.05	0.9692
6	45	400	0.05	0.05	0.9827	6	40	600	0.05	0.05	0.8806
7	40	400	0.05	0.05	0.9692	7	45	400	0.05	0.05	0.9827
8	44	600	0.05	0.05	0.9078	8	44	400	0.05	0.05	0.9805
9	43	400	0.05	0.05	0.9780	9	40	400	0.05	0.04	0.9909
10	40	400	0.05	0.04	0.9909	10	44	400	0.05	0.04	0.9958
11	44	400	0.05	0.04	0.9958	11	45	400	0.05	0.04	0.9967
12	45	400	0.05	0.04	0.9967						

b. Simulations for $\gamma = 3$.

Table F.4 Performance of SMED and our method with positive DRPCS and $\gamma=3$ (Same as Table E.1).

Experiment Number	SMED—Scenario 1					Our Method					
	Laser Power (W)	Laser Velocity (mm/s)	Hatch Distance (mm)	Laser Thickness (mm)	Relative Density	Experiment Number	Laser Power (W)	Laser Velocity (mm/s)	Hatch Distance (mm)	Laser Thickness (mm)	Relative Density
1	44	2000	0.05	0.03	0.7295	1	44	2000	0.05	0.03	0.7295
2	45	400	0.15	0.05	0.7268	2	45	400	0.15	0.05	0.7268
3	40	400	0.1	0.05	0.7831	3	40	400	0.1	0.05	0.7831
4	40	400	0.15	0.04	0.7328	4	40	400	0.15	0.04	0.7328
5	40	400	0.05	0.05	0.9692	5	40	400	0.05	0.05	0.9692
6	44	600	0.1	0.05	0.7295	6	44	600	0.1	0.05	0.7295
7	41	400	0.05	0.05	0.9725	7	41	400	0.05	0.05	0.9725
8	42	400	0.05	0.05	0.9754	8	42	400	0.05	0.05	0.9754
9	43	400	0.05	0.05	0.9780	9	43	400	0.05	0.05	0.9780
10	44	400	0.05	0.05	0.9805	10	44	400	0.05	0.05	0.9805
11	43	600	0.05	0.05	0.9016	11	43	600	0.05	0.05	0.9016
12	45	400	0.05	0.05	0.9827	12	45	400	0.05	0.05	0.9827
13	40	800	0.05	0.05	0.7831	13	40	800	0.05	0.05	0.7831
14	44	800	0.05	0.05	0.8164	14	44	800	0.05	0.05	0.8164
15	40	400	0.05	0.04	0.9909	15	40	400	0.05	0.04	0.9909
16	40	600	0.05	0.05	0.8806	16	45	400	0.05	0.04	0.9967
17	41	400	0.05	0.04	0.9924						
18	42	400	0.05	0.04	0.9937						
19	43	400	0.05	0.04	0.9948						
20	44	400	0.05	0.04	0.9958						
21	42	600	0.05	0.04	0.9477						
22	45	400	0.05	0.04	0.9967						

Table F.5 Performance of SMED and our method with positive and negative DRPCS and $\gamma=3$ (Same as Table E.3).

Experiment Number	SMED				Experiment Number	Our Method				
	Laser Power (W)	Laser Velocity (mm/s)	Hatch Distance (mm)	Laser Thickness (mm)		Relative Density	Laser Power (W)	Laser Velocity (mm/s)	Hatch Distance (mm)	Laser Thickness (mm)
1	44	800	0.15	0.03	1	44	800	0.15	0.03	0.8406
2	44	600	0.15	0.04	2	44	600	0.15	0.04	0.8406
3	45	400	0.15	0.05	3	45	400	0.15	0.05	0.7268
4	40	400	0.15	0.03	4	44	1200	0.1	0.03	0.8406
5	44	1200	0.1	0.03	5	45	400	0.15	0.03	0.8602
6	44	800	0.1	0.03	6	44	600	0.1	0.03	0.8528
7	40	400	0.15	0.04	7	40	400	0.1	0.03	0.9381
8	44	600	0.15	0.03	8	43	400	0.1	0.03	0.9521
9	45	400	0.05	0.05	9	45	400	0.1	0.03	0.9597
10	44	400	0.05	0.05	10	44	400	0.1	0.03	0.9560
11	42	400	0.05	0.05	11	42	400	0.1	0.03	0.9477
12	43	400	0.05	0.05	12	41	400	0.1	0.03	0.9431
13	40	400	0.05	0.05	13	40	400	0.05	0.03	0.9999
14	44	600	0.05	0.05						
15	41	400	0.05	0.05						
16	40	800	0.05	0.05						
17	40	600	0.05	0.05						
18	41	400	0.05	0.04						
19	40	400	0.05	0.04						
20	42	400	0.05	0.04						
21	43	400	0.05	0.04						
22	44	400	0.05	0.04						
23	45	400	0.05	0.04				0.05	0.03	0.9967

Table F.6 Performance of SMED and our method with positive DRPCS and $\gamma=3$ (Same as Table E.4).

Experiment Number	SMED					Experiment Number	Our Method				
	Laser Power (W)	Laser Velocity (mm/s)	Hatch Distance (mm)	Laser Thickness (mm)	Relative Density		Laser Power (W)	Laser Velocity (mm/s)	Hatch Distance (mm)	Laser Thickness (mm)	Relative Density
1	44	800	0.15	0.03	0.8406	1	44	800	0.15	0.03	0.8406
2	44	2000	0.05	0.03	0.7295	2	44	2000	0.05	0.03	0.7295
3	44	1800	0.05	0.04	0.8406	3	45	400	0.15	0.05	0.7268
4	45	400	0.15	0.05	0.7268	4	45	400	0.15	0.03	0.8602
5	44	1400	0.05	0.05	0.8098	5	44	1200	0.1	0.03	0.8406
6	44	1200	0.1	0.03	0.8406	6	44	1400	0.05	0.05	0.8098
7	44	1400	0.05	0.04	0.7261	7	45	400	0.1	0.03	0.9597
8	45	400	0.15	0.03	0.8602	8	42	400	0.1	0.03	0.9477
9	45	400	0.1	0.03	0.9597	9	44	400	0.1	0.03	0.9560
10	43	400	0.1	0.03	0.9521	10	40	400	0.1	0.03	0.9381
11	40	400	0.1	0.03	0.9381	11	44	600	0.1	0.03	0.8528
12	44	400	0.1	0.03	0.9560	12	43	400	0.1	0.03	0.9521
13	42	400	0.1	0.03	0.9477	13	41	400	0.1	0.03	0.9431
14	44	600	0.1	0.03	0.8528	14	40	400	0.05	0.03	0.9999
15	41	400	0.1	0.03	0.9431						
16	43	400	0.05	0.03	0.9998						

c. Simulations for $\gamma = 5$

Table F.7 Performance of SMED and our method with negative DRPCS and $\gamma=5$.

Experiment Number	SMED					Experiment Number		Our Method			
	Laser Power (W)	Laser Velocity (mm/s)	Hatch Distance (mm)	Laser Thickness (mm)	Relative Density	Number	Laser Power (W)	Laser Velocity (mm/s)	Hatch Distance (mm)	Laser Thickness (mm)	Relative Density
1	44	800	0.15	0.03	0.8406	1	44	800	0.15	0.03	0.8406
2	45	400	0.15	0.05	0.7268	2	45	400	0.15	0.05	0.7268
3	41	800	0.15	0.03	0.9496	3	41	800	0.15	0.03	0.9496
4	44	600	0.15	0.03	0.7294	4	44	600	0.15	0.03	0.7294
5	42	800	0.15	0.03	0.9067	5	42	800	0.15	0.03	0.9067
6	43	800	0.15	0.03	0.8708	6	43	800	0.15	0.03	0.8708
7	40	600	0.1	0.03	0.8199	7	40	400	0.1	0.03	0.9381
8	41	600	0.15	0.04	0.9496	8	40	800	0.1	0.03	0.7328
9	42	600	0.15	0.04	0.9067	9	41	400	0.1	0.03	0.9431
10	43	600	0.15	0.04	0.8708	10	42	400	0.1	0.03	0.9477
11	40	400	0.15	0.04	0.7328	11	43	400	0.1	0.03	0.9521
12	45	400	0.15	0.04	0.7621	12	44	400	0.1	0.03	0.9560
13	40	1000	0.1	0.03	0.7638	13	45	400	0.1	0.03	0.9597
14	44	600	0.15	0.04	0.8406	14	40	400	0.05	0.03	0.9999
15	40	400	0.1	0.04	0.8602						
16	40	800	0.1	0.04	0.8155						
17	42	400	0.1	0.04	0.8757						
18	45	400	0.1	0.04	0.8962						
19	43	400	0.1	0.04	0.8829						
20	44	400	0.1	0.04	0.8898						
21	40	600	0.1	0.04	0.7328						
22	44	600	0.1	0.04	0.7554						
23	40	400	0.05	0.05	0.9692						
24	41	400	0.1	0.04	0.8682						
25	41	400	0.05	0.05	0.9725						
26	42	400	0.05	0.05	0.9754						
27	43	400	0.05	0.05	0.9780						
28	44	400	0.05	0.05	0.9805						
29	42	600	0.05	0.05	0.8950						

Performance of SMED and our method with negative DRPCS and $\gamma=5$ (continued).

Experiment Number	SMED				
	Laser Power (W)	Laser Velocity (mm/s)	Hatch Distance (mm)	Laser Thickness (mm)	Relative Density
30	45	400	0.05	0.05	0.9827
31	40	800	0.05	0.05	0.7831
32	44	800	0.05	0.05	0.8164
33	40	600	0.05	0.05	0.8806
38	44	600	0.05	0.05	0.9078
35	41	600	0.05	0.05	0.8880
36	43	600	0.05	0.05	0.9016
37	40	400	0.05	0.04	0.9909
38	45	400	0.05	0.04	0.9967

Table F.8 Performance of SMED and our method with negative DRPCS and $\gamma=5$.

Experiment Number	SMED				Experiment Number	Our Method					
	Laser Power (W)	Laser Velocity (mm/s)	Hatch Distance (mm)	Laser Thickness (mm)		Relative Density	Laser Power (W)	Laser Velocity (mm/s)	Hatch Distance (mm)	Laser Thickness (mm)	Relative Density
1	44	800	0.15	0.03	1	0.8406	44	800	0.15	0.03	0.8406
2	45	400	0.15	0.03	2	0.8602	45	400	0.15	0.03	0.8602
3	45	400	0.15	0.04	3	0.7621	45	400	0.15	0.04	0.7621
4	40	400	0.15	0.03	4	0.8199	40	400	0.15	0.03	0.8199
5	44	1200	0.1	0.03	5	0.8406	44	1200	0.1	0.03	0.8406
6	44	1000	0.1	0.03	6	0.7295	44	1000	0.1	0.03	0.7295
7	44	600	0.15	0.03	7	0.7294	44	600	0.15	0.03	0.7294
8	44	400	0.15	0.03	8	0.8528	44	400	0.15	0.03	0.8528
9	45	400	0.15	0.05	9	0.7268	45	400	0.15	0.05	0.7268
10	41	1200	0.1	0.03	10	0.9496	41	1200	0.1	0.03	0.9496
11	42	1200	0.1	0.03	11	0.9067	42	1200	0.1	0.03	0.9067
12	43	1200	0.1	0.03	12	0.8708	43	1200	0.1	0.03	0.8708
13	40	1000	0.05	0.03	13	0.8806	40	1000	0.05	0.03	0.8806
14	44	1000	0.05	0.03	14	0.9078	44	1000	0.05	0.03	0.9078
15	43	1000	0.05	0.03	15	0.9016	43	1000	0.05	0.03	0.9016
16	44	800	0.05	0.03	16	0.9560	44	800	0.05	0.03	0.9560
17	43	800	0.05	0.03	17	0.9521	43	800	0.05	0.03	0.9521
18	42	800	0.05	0.03	18	0.9477	42	800	0.05	0.03	0.9477
19	40	800	0.05	0.03	19	0.9381	40	800	0.05	0.03	0.9381
20	41	800	0.05	0.03	20	0.9431	41	800	0.05	0.03	0.9431
21	43	600	0.05	0.03	21	0.9877	43	600	0.05	0.03	0.9877
22	44	600	0.05	0.03	22	0.9894	44	600	0.05	0.03	0.9894
23	42	600	0.05	0.03	23	0.9859	42	600	0.05	0.03	0.9859
24	41	600	0.05	0.03	24	0.9838	41	600	0.05	0.03	0.9838
25	40	600	0.05	0.03	25	0.9815	40	600	0.05	0.03	0.9815
26	42	400	0.05	0.03	26	0.9999	42	400	0.05	0.03	0.9999

Table F.9 Performance of SMED and our method with positive DRPCS and $\gamma=5$.

Experiment Number	Laser			SMED			Experiment Number	Laser			Our Method			Relative Density
	Power (W)	Velocity (mm/s)	Hatch Distance (mm)	Laser Thickness (mm)	Relative Density	Number		Power (W)	Velocity (mm/s)	Hatch Distance (mm)	Laser Thickness (mm)			
1	44	800	0.15	0.03	0.8406	1	44	800	0.15	0.03	0.8406			
2	44	2000	0.05	0.03	0.7295	2	44	2000	0.05	0.03	0.7295			
3	44	1800	0.05	0.04	0.8406	3	45	400	0.15	0.05	0.7268			
4	45	400	0.15	0.05	0.7268	4	45	400	0.15	0.03	0.8602			
5	44	1400	0.05	0.05	0.8098	5	40	400	0.15	0.03	0.8199			
6	44	1200	0.1	0.03	0.8406	6	44	1200	0.1	0.03	0.8406			
7	44	1600	0.05	0.04	0.7481	7	45	400	0.1	0.03	0.9597			
8	45	400	0.15	0.03	0.8602	8	44	400	0.1	0.03	0.9560			
9	40	400	0.15	0.03	0.8199	9	42	400	0.1	0.03	0.9477			
10	45	400	0.1	0.03	0.9597	10	43	400	0.1	0.03	0.9521			
11	44	400	0.1	0.03	0.9560	11	40	400	0.1	0.03	0.9381			
12	42	400	0.1	0.03	0.9477	12	41	400	0.1	0.03	0.9431			
13	43	400	0.1	0.03	0.9521	13	44	600	0.1	0.03	0.8528			
14	40	400	0.1	0.03	0.9381	14	42	400	0.05	0.03	0.9999			
15	41	400	0.1	0.03	0.9431									
16	44	600	0.1	0.03	0.8528									
17	44	400	0.05	0.03	0.9997									

Table F.10 Performance of SMED and our method with positive DRPCS and $\gamma=5$.

Experiment Number	Laser			SMED			Experiment			Our Method			Relative Density
	Power (W)	Velocity (mm/s)	Hatch Distance (mm)	Laser Thickness (mm)	Relative Density	Number	Laser Power (W)	Laser Velocity (mm/s)	Hatch Distance (mm)	Laser Thickness (mm)			
1	44	800	0.15	0.03	0.8406	1	44	800	0.15	0.03	0.8406	0.8406	
2	44	2000	0.05	0.03	0.7295	2	44	2000	0.05	0.03	0.7295	0.7295	
3	44	1800	0.05	0.04	0.8406	3	45	400	0.15	0.05	0.7268	0.7268	
4	45	400	0.15	0.05	0.7268	4	45	400	0.15	0.03	0.8602	0.8602	
5	44	1400	0.05	0.05	0.8098	5	40	400	0.15	0.03	0.8199	0.8199	
6	44	1200	0.1	0.03	0.8406	6	44	1200	0.1	0.03	0.8406	0.8406	
7	44	1600	0.05	0.04	0.7481	7	45	400	0.1	0.03	0.9597	0.9597	
8	45	400	0.15	0.03	0.8602	8	44	400	0.1	0.03	0.9560	0.9560	
9	40	400	0.15	0.03	0.8199	9	42	400	0.1	0.03	0.9477	0.9477	
10	45	400	0.1	0.03	0.9597	10	43	400	0.1	0.03	0.9521	0.9521	
11	44	400	0.1	0.03	0.9560	11	40	400	0.1	0.03	0.9381	0.9381	
12	42	400	0.1	0.03	0.9477	12	41	400	0.1	0.03	0.9431	0.9431	
13	43	400	0.1	0.03	0.9521	13	44	600	0.1	0.03	0.8528	0.8528	
14	40	400	0.1	0.03	0.9381	14	42	400	0.05	0.03	0.9999	0.9999	
15	41	400	0.1	0.03	0.9431								
16	44	600	0.1	0.03	0.8528								
17	44	400	0.05	0.03	0.9997								

APPENDIX G
ALGORITHM OF M-APO

The algorithm of m-APO is described in detail as follows:

- **Step 1: Decomposing master problem into sub-problems**

First, the master bi-objective optimization problem is broken down into a sequence of single objective sub-problems formulated (solvable by APO) as a convex combination of individual objective functions represented by Eq. (5.2). To identify the scope of objective space, the m-APO first requires achieving a targeted optimum value for individual objectives. (In our LBAM mechanical properties optimization case, the targeted value for part relative density and elongation-to-failure should be set considering the powder properties and the machine technical capabilities. Those should be reasonable desired values.) Hence, the algorithm is initialized by choosing two boundary sub-problems with $(\gamma_1^1 = 0, \gamma_2^1 = 1)$ and $(\gamma_1^2 = 1, \gamma_2^2 = 0)$. These two initial sub-problems represent the single objective optimization problems with respect to only one mechanical property. The solution to the first two sub-problems identifies the ends of Pareto front on the objective space (i.e., segments e and c in Figure 2.40)

- **Step 2: Applying Accelerated Process Optimization (APO) to sub-problems**

The APO [1] is incorporated into m-APO framework to consecutively design experiments and optimize the selected single objective sub-problems at each step. Suppose the weight coefficients associated with the current sub-problem is already identified, i.e., γ_1^h and γ_2^h . All the design points and the corresponding response vectors, i.e., $(\mathbf{s}_i, \mathbf{Y}_i)$, are mapped and scaled to the current sub-problem in the form of weighted summation of single responses, i.e., (\mathbf{s}_i, Z_i^h) via the transformation equation $Z_i^h(\mathbf{s}_i) = \gamma_1^h \cdot Y_1(\mathbf{s}_i) + \gamma_2^h \cdot Y_2(\mathbf{s}_i)$ represented by Eq. (5.2). The experimental data obtained from optimization procedure of previous sub-problems (i.e., sub-problems 1, 2, ..., $h - 1$) are treated as prior data and fed

into APO to guide and accelerate optimization of the current sub-problem (i.e., h^{th} sub-problem). The APO leverages the transformed information to improve prediction of the weighted single objective responses corresponding to the untested design points for the subsequent sub-problems. Consequently, improving the prediction accuracy of the single objective responses result in guiding the algorithm towards achieving the Pareto optimal solution corresponding to the current sub-problem in an accelerated manner.

The APO makes a direct analogy with a fundamental electrostatic law to balance optimization and space-filling properties. In any sub-problem the APO assigns a simulative positive charged particle $q^h(\mathbf{s}_j)$ to each design point. The charge function $q^h(\mathbf{s})$ should be appropriately selected in relation to the objective of optimization. Since our case is a maximization problem, $q^h(\mathbf{s})$ should be defined as an inversely proportional function of the weighted single objective response values $Z^h(\mathbf{s})$ corresponding to each sub-problem in Eq. (5.2) [1,51]. Considering this, particles with lower charge are assigned to design points with higher $Z^h(\mathbf{s})$ and converse. Figure G.1 demonstrates an illustrative example of applying APO and the associated dynamics in the design space corresponding to the objective space illustrated in Figure 2.40. For instance, design points (a) and (b) on the right side of Figure G.1 (a) are illustrated with larger positive particles compared with design point (c) on the middle left of the contour plot. This is because of the fact that design points (a) and (b) result in lower Z^1 in comparison with design point (c). Note that, since the combination of weight coefficients and the corresponding single objective response values $Z^h(\mathbf{s})$ changes from one sub-problem to another, the corresponding charge function should change as well. Hence, we observe that positive particle charges with different sizes are assigned to the same design points in different contour plots (i.e., different sub-

problems). The m-APO leverages the dynamics associated with the differences amongst the sub-problems' objective spaces by intelligently mapping the charged particles from one sub-problem to another. Similar to a fundamental electrostatic law, the design points (so-called positive charged particles) push each other apart so as to minimize the total electrostatic potential energy in the contour plot domain (i.e., design space). Since the design points associated with the lower charged particles (i.e., with higher $Z^h(\mathbf{s})$) weakly repel others, more new design points have the chance to be accommodated in their neighborhood. The resulting allocation of the design points corresponds to the minimum total potential energy. Considering this analogy, the sequential selection of the design points will lead to maximize the objective function of interest in the current sub-problem (i.e., $Z^h(\mathbf{s})$) with reduced number of experimental runs.

The so-called electrostatic potential energy between any two design points \mathbf{s}_i and \mathbf{s}_j is defined as $q(\mathbf{s}_i)q(\mathbf{s}_j)/d(\mathbf{s}_i, \mathbf{s}_j)$, where $d(\mathbf{s}_i, \mathbf{s}_j)$ represents the Euclidean distance between \mathbf{s}_i and \mathbf{s}_j . Therefore, the total electrostatic potential energy function corresponding to the h^{th} sub-problem including the n^{th} new design is formulated as follows:

$$E_n^h = \sum_{i=1}^{n-1} \sum_{j=i+1}^n \frac{q^h(\mathbf{s}_i)q^h(\mathbf{s}_j)}{d(\mathbf{s}_i, \mathbf{s}_j)} \quad (\text{G.3})$$

The new design point can be obtained by solving $\mathbf{s}_n = \text{argmin } E_n^h$. Details of the single objective response value prediction for new untested design points and the charge function computation is beyond the scope of the present paper and can be found in Ref. [1].

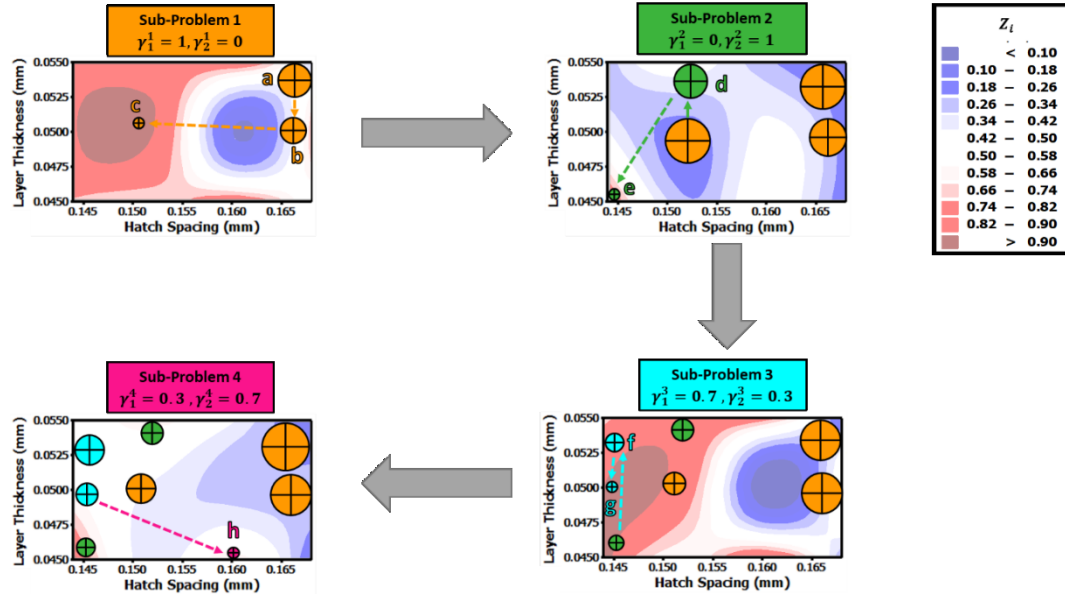


Figure G.1 Schematic illustration of applying APO to different sub-problems, and representing the design space dynamics associated with conducting m-APO.

- **Step 3: Defining Hyper-Volume (HV) and stopping criteria for sub-problems**

Hyper-Volume (HV) metric—a well-known performance indicator in the realm of multi-objective optimization—is employed to construct the stopping criteria for m-APO [95,139]. HV assesses the size of the region on the objective space dominated by the resulting Pareto optimal solutions. Therefore, higher HV indicates better coverage of the true Pareto front and thus bring about the better Pareto front approximation. Throughout the algorithm, ΔHV (i.e., HV increment) represents the contribution of a new Pareto optimal solution in terms of solution improvement. In other words, ΔHV quantifies the achievement of a new Pareto optimal solution. For instance, in Figure G.2 black rectangle represents ΔHV associated with a new Pareto optimal solution. Moreover, the size of the whole shaded area (including the black rectangle) indicates the HV associated with the current approximated Pareto front. The m-APO continues designing experiments for the current

sub-problem via APO until the current ΔHV is less than a pre-specified boundary (i.e., $\Delta HV < \varepsilon_1$). In that case, the m-APO stops proceeding with the current sub-problem and move on to the next sub-problem. Moreover, the m-APO stops keep constructing new sub-problems and consequently designing more experiments when a significant improvement in ΔHV is not observed (i.e., $\Delta HV < \varepsilon_2$).

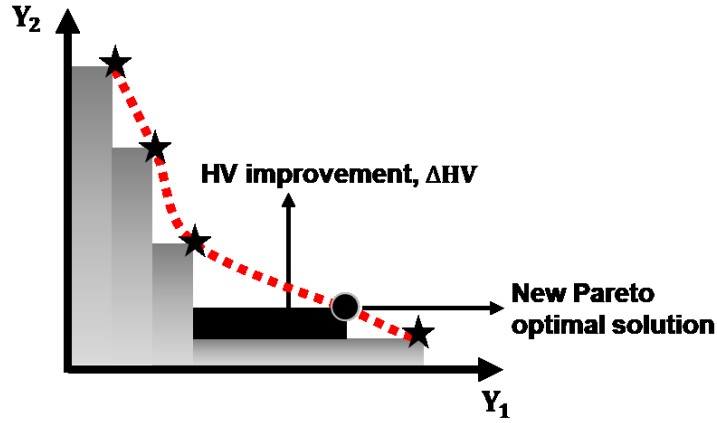


Figure G.2 Schematic illustration of HV as the yardstick of improving the Pareto front approximation.

The black rectangle represents ΔHV , i.e., the contribution of a new Pareto optimal solution with regard to HV improvement.

- **Step 4: Constructing sub-problems by determining appropriate weight coefficients**

At the end of each sub-problem, contingent upon the distribution of the current Pareto optimal solutions, m-APO calculates the appropriate weight coefficients (i.e., γ^h) to construct the next sub-problem. The weighting coefficients are identified in a way to cover the existing gaps on the Pareto front. Note that in the preset work unknown variables are represented by upper case letters, while known variables are illustrated by lower case letters. Suppose m-APO stopped designing experiments for the $(h - 1)^{th}$ sub-problem.

Hence, currently m optimal design points and corresponding Pareto optimal solutions are achieved represented by the set $\Phi^{h-1} = \{(\mathbf{s}_1^*, \mathbf{y}_1^*), (\mathbf{s}_2^*, \mathbf{y}_2^*), \dots, (\mathbf{s}_m^*, \mathbf{y}_m^*)\}$. Afterwards, the Euclidean distance between all of the neighboring Pareto points and accordingly the largest gap on the existing Pareto front is determined as follows:

$$\delta_j = |\mathbf{y}(\mathbf{s}_{(j+1)}^*) - \mathbf{y}(\mathbf{s}_{(j)}^*)| \quad \text{for } j = 1, \dots, (m-1)$$

$$\Delta = \max_{j=1, \dots, (m-1)} \delta_j$$

Suppose \mathbf{s}_a^* and \mathbf{s}_b^* are the neighboring Pareto points corresponding to Δ , where $y_1(\mathbf{s}_a^*) < y_1(\mathbf{s}_b^*)$. To cover the largest gap on the existing Pareto front, the weight coefficients for the next sub-problem is identified as $\boldsymbol{\gamma}^h = c^h(y_2(\mathbf{s}_a^*) - y_2(\mathbf{s}_b^*), y_1(\mathbf{s}_b^*) - y_1(\mathbf{s}_a^*))$, where c^h is a constant leading to $\gamma_1^h + \gamma_2^h = 1$. In that way, the consecutive sub-problems can efficiently achieve well-distributed Pareto optimal points to approximate the true Pareto front using minimum amount of resource.